EFFECTS OF STELLAR ROTATION ON YOUNG CLUSTER HR DIAGRAMS

by

Christopher M. Geroux

A Thesis Submitted to Saint Mary's University, Halifax, Nova Scotia in Partial Fulfillment
of the Requirements for the Degree of

MASTER OF SCIENCE

in

Astronomy

(Department of Physics and Astronomy)

November 20, 2007,Halifax, Nova Scotia

Approved: Dr. R.G. Deupree
Supervisor

Approved: Dr. D.G. Turner
Examiner

Approved: Dr. D.B. Guenther
Examiner

Date: November 20, 2007

Library and
Archives Canada

Published Heritage
Branch

395 Wellington Street
Ottawa ON K1A 0N4
Canada

Bibliothèque et
Archives Canada

Direction du
Patrimoine de l'édition

395, rue Wellington
Ottawa ON K1A 0N4
Canada

Your file Votre référence
ISBN: 978-0-494-35768-2
Our file Notre référence
ISBN: 978-0-494-35768-2

NOTICE:
The author has granted a non-exclusive license allowing Library and Archives Canada to reproduce, publish, archive, preserve, conserve, communicate to the public by telecommunication or on the Internet, loan, distribute and sell theses worldwide, for commercial or non-commercial purposes, in microform, paper, electronic and/or any other formats.

The author retains copyright ownership and moral rights in this thesis. Neither the thesis nor substantial extracts from it may be printed or otherwise reproduced without the author's permission.

AVIS:
L'auteur a accordé une licence non exclusive permettant à la Bibliothèque et Archives Canada de reproduire, publier, archiver, sauvegarder, conserver, transmettre au public par télécommunication ou par l'Internet, prêter, distribuer et vendre des thèses partout dans le monde, à des fins commerciales ou autres, sur support microforme, papier, électronique et/ou autres formats.

L'auteur conserve la propriété du droit d'auteur et des droits moraux qui protège cette thèse. Ni la thèse ni des extraits substantiels de celle-ci ne doivent être imprimés ou autrement reproduits sans son autorisation.

In compliance with the Canadian Privacy Act some supporting forms may have been removed from this thesis.

While these forms may be included in the document page count, their removal does not represent any loss of content from the thesis.

Conformément à la loi canadienne sur la protection de la vie privée, quelques formulaires secondaires ont été enlevés de cette thèse.

Bien que ces formulaires aient inclus dans la pagination, il n'y aura aucun contenu manquant.

Canada

Reproduced with permission of the copyright owner. Further reproduction prohibited without permission.

CONTENTS

LIST OF FIGURES

LIST OF TABLES

ACKNOWLEDGEMENTS

First and foremost I would like to thank Bob Deupree, my supervisor. He has not only supplied me with the foundation for the current work, but help to ensure that this project was a success. I wish to thank Bob for his considerable advice, guidance, encouragement and patience throughout this process. I would also like to thank David Turner and David Guenther, my examining committee. I appreciate the time you have both taken out of your busy schedules to read and examine my thesis. I would also like to thank Matthew Cooper, an undergrad student from Dalhousie University, who helped with some of the early exploratory work. I would like to thank Aaron Gillich, and Catherine Lovekin who provided much of the foundation work that made this thesis possible. It has been a great help to have had both of you readily available for questions. In addition I would like to thank Joel Tanner for supplying some of the ROTORC models used. I would also like to thank the other grad students at Saint Mary's University for your support through this project. Finally I would like to thank my girlfriend Jennifer Parker, who has dealt with my stress and lack of time during this project.

ABSTRACT

EFFECTS OF STELLAR ROTATION ON YOUNG CLUSTER HR DIAGRAMS

by Christopher Geroux

This thesis investigates the effects of stellar rotation on the HR diagram location of members within young clusters. The rotational effects on luminosity and temperature of a star depend on the viewing angle and the rotation rate of the star and must be included in determining the HR diagram locations. The position of members is used as an indicator of the rotational characteristics of the individual stars. The fraction of clusters with a selected member within restricted ranges of rotation rate and viewing angle has been calculated for each selected member. These selected members are: brightest cluster member, bluest cluster member, and reddest cluster member above a luminosity cutoff. The brightest and bluest members were found to be rapidly rotating and viewed pole-on in 74% and 88% of the clusters respectively. The reddest member above a luminosity cutoff was found to be rapidly rotating and viewed equator on in 94% of the clusters.

November 20, 2007

1 INTRODUCTION

Stellar rotation is difficult to study directly for stars other than the Sun. Observationally the surface rotation velocity can be measured by spectroscopy using Doppler broadening of spectral lines. This allows one to measure the line of sight velocity, $v \sin i$, causing the measured velocity to be dependent on the inclination, i, of the rotation axis to the observer's line of sight. The intertwining of inclination and rotation velocity causes difficulty in studying rotating stars. For stars rotating sufficiently rapidly, their position in the HR diagram can be greatly affected not only by their rotation rate but also by their inclination, as shown by Collins (1966), Hardorp & Strittmatter (1968a), Maeder & Peytremann (1970), and Gillich (2007). One aim of this thesis is to explore how the dependence of a star's location in the HR diagram, due to rotation and viewing angle, can be used to constrain a star's rotation rate and inclination under certain conditions. One of these conditions is that the star be a member of a cluster.

Star clusters are of great use to astronomers because the members of a cluster form out of the same material at essentially the same time. The age of clusters can be estimated from isochrone fitting. Due to these properties, clusters are very useful for testing theoretical stellar models. In the present work synthetic clusters are constructed to examine how a cluster member's position on the HR diagram can constrain its rotation and inclination under specific conditions. Through examination of the properties of cluster members in specific HR diagram locations, in particular the members near the extrema (e.g., brightest, bluest) of the cluster HR diagram, the fraction of clusters can be calculated with these selected members having certain rotation velocities and inclinations.

Recent studies by Strom, Wolff, & Dror (2005) and Wolff et al. (2007) suggest that the distribution of rotation velocities among stars may vary based on their environment. They find that field B stars on average are slower rotators than B stars in clusters. Turner (1996a,b) finds a correlation between reddening and $v \sin i$ saying that this is suggestive of circumstellar reddening and circumstellar disks and suggests that the origin of rapidly rotating stars could be explained by mergers. This led Turner to the conclusion that if rapidly rotating stars are generated via mergers then 40% to 50% of the stars prior to mergers must have been binaries to account for the number of stars exhibiting rapid rotation and circumstellar reddening. Turner also notes that a high number of binaries is far more likely in dense cores of clusters. These environmental effects lead to the issue of how the fraction of clusters having selected members with specific rotational characteristics is affected by the distribution of rotation among cluster members. We shall address this by examining several distribution functions for allocating rotation rates among stars in a cluster.

Understanding how rotation affects the luminosity and effective temperature of stars is necessary in studying early type stars to deduce the star's true physical characteristics. Sufficiently rapid rotation can greatly alter a star's deduced effective temperature and luminosity (Collins, 1963). For example, a 12 $M_\odot$ ZAMS model rotating uniformly with a surface equatorial velocity of 575 km s^{-1} can have its apparent position on the HR diagram moved so much that it may have the same luminosity and effective temperature as a non-rotating 8 $M_\odot$ model near the ZAMS. To derive information from clusters which contain stars that rotate appreciably, it is necessary to understand the effects that rotation has on a star's location in the HR diagram. We shall refer to this relationship between inclination and location in the HR diagram as an inclination curve.

The present work strives to determine the fraction of clusters with members at selected locations in the HR diagram having inclinations and rotation rates within a specified range. The robustness of these fractions is tested by considering different numbers of cluster members, different limitations on the inclination and rotation rates of the selected members, and a different number of rapidly rotating stars in the cluster. We will use different numbers of clusters and stars in a cluster to determine how sample size affects the calculated fractions.

Once the mass, rotation rate, and surface properties of a star are specified an inclination curve can be computed. Then once an inclination is specified, a point on the inclination curve can be determined, thus placing the star in the HR diagram. The inclination curves used in this work are computed with analytic approximations we designed to match actual inclination curves computed by Gillich (2007). The analytic approximation of inclination curves requires stellar structure information, which is derived from evolutionary tracks of rotating stars. The next section will describe how rotating stars have been modeled in the past, as well as how inclination curves are determined for these stellar models.

1.1 MODELING ROTATING STARS

Several steps are required to simulate the observed luminosity and effective temperature of rotating stars. First we construct a stellar model to determine the surface effective temperature and gravity as functions of colatitude. Then model atmospheres are used to produce angle dependent intensities. The model atmospheres depend on the local values of the effective temperature and gravity from the structure calculations. A grid of atmospheres is needed to cover the range of effective temperature and gravity over the surface of the stellar model. The intensities in the direction of the observer are then integrated over the surface of the stellar model to produce the observed flux as a function of wavelength, which is referred to as the spectral energy distribution (SED). Thus, the observed SED depends on the inclination. From the SED, effective temperatures and luminosities can be derived: temperature by the shape of the SED and luminosity by the integration of the SED over all wavelengths. Inclination curves are constructed for a given model by calculating the effective temperature and luminosity from the different SEDs of models at varying inclinations.

1.1.1 STELLAR INTERIORS

One of the earliest methods for describing the surface properties of rotating stars was provided by von Zeipel (1924). He showed that if a rotating star is in hydrostatic and radiative equilibrium, then the pressure and density are constant on equipotential surfaces. Assuming an ideal gas law it can be shown that temperature is also constant on an equipotential surface if the composition is uniform. For purely radiative stars, the flux can be expressed as the product of the temperature gradient and a radiative conductivity. The flux is constant on an equipotential surface because the temperature is constant on an equipotential surface. Thus the flux is parallel to the gradient of the total potential. The surface flux is proportional to T_{eff}^4 as well as to the gradient of the total potential, $\nabla\Phi \equiv g_{\text{eff}}$, producing the proportionality, $T_{\text{eff}} \propto g_{\text{eff}}^{1/4}$, known as von Zeipel's theorem. g_{eff} is the effective gravitational acceleration, which is the sum of the gravitational and centrifugal accelerations normal to the surface. This relation can be used to determine the effective temperature as a function of colatitude, $T_{\text{eff}}(\theta)$, from g_{eff}, which is dependent on the interior mass distribution, the radius as a function of colatitude, $R(\theta)$, and the angular velocity of the rotating star.

One of the earliest structural model of a rotating star was done by Sweet & Roy (1953), who used a first-order perturbation technique to calculate the structure of a rotating model based on a numerical Cowling model computed by Gardiner (1951). The Cowling model is a solution to the equations of stellar structure with a convective core and a radiative envelope (Cowling, 1935). Sweet & Roy found that when the ratio of equatorial centrifugal force to surface gravity was greater than 0.29, the first order model breaks down and higher order corrections need to be accounted for. They also discussed that, using their first-order model, the mean effective temperature and luminosity of a rotating star are reduced. Another result was that rotation produces a spread in luminosity, when viewed from different inclinations, on the order of half a magnitude for the most rapidly rotating B stars. When the rotating star is viewed pole-on, it will appear brighter and hotter than if viewed equator on.

Roxburgh, Griffith, & Sweet (1965) modeled more rapidly rotating stars using a two part model, with the inner part of the model containing the majority of the mass and the outer envelope containing a negligible amount of the mass. In the inner region, the ratio of centrifugal force to gravity was small and could be modeled with the first order perturbation method used by Sweet & Roy (1953). In the outer region the potential was determined by an approximate solution to Laplace's equation allowing the structure equations to be integrated in the same manner as for spherical stars. The opacity used in the model was electron scattering, which applies to very early-type stars, while neglecting radiation pressure, which applies to late-type stars. Faulkner, Roxburgh, & Strittmatter (1968) improved upon the models by including better opacities and nuclear energy generation rates along with more realistic boundary conditions. Sackmann & Anand (1969) then included radiation pressure in the model calculations. Sackmann & Anand (1970) present the first quantitative computations of the evolution of uniformly rotating stars, finding that rotation moves the evolution track down in luminosity and to lower effective temperatures.

The methods previously described are only useful for relatively slowly rotating stars where the distortions to internal structure are small, and cannot handle the large changes in internal structure that are possible in white dwarfs and rapidly rotating massive stars (Ostriker & Mark, 1968). Ostriker & Mark (1968) developed the self-consistent-field (SCF) method to determine the equilibrium structure of a rapidly rotating star. This method separates the problem of solving for the potential and the density profile by adopting an initial density distribution and using Poisson's equation to solve the potential from the density profile. One then solves the equations for hydrostatic equilibrium and the boundary conditions for the density profile that corresponds to the potential. The process is repeated, improving the density profile and potential. The SCF method was extended by Jackson (1970), who used the Henyey method (Henyey, Forbes, & Gould, 1964) to permit the inclusion of nuclear-energy generation and energy transport by allowing the solution of differential equations to relate the density to the potential rather than the simplified algebraic equations used previously. The SCF failed to converge if the mass is less than about 9 $M_\odot$ (Clement, 1978), even for non-rotating main-sequence models. However, that is disputed in a recent paper by Jackson, MacGregor, & Skumanich (2005). In this method the type of differential rotation is restricted to a conservative rotation law having constant angular velocity on cylindrical surfaces co-axial to the rotation axis (Mark, 1968).

There are two main types of differential rotation laws, conservative and non-conservative. A conservative rotation law is one in which the centrifugal force can be derived from a potential. Bodenheimer (1971) considered different conservative rotation laws to explore the effects of differential rotation on a stellar model's luminosity and effective temperature. He found using the SCF method that the luminosity is nearly independent of the rotation law, and dependent on the mass and total angular momentum.

Clement (1974, 1978, 1979) developed a two-dimensional finite-difference technique for solving Poisson's equation. This method can only accommodate conservative rotation laws and becomes numerically unstable otherwise. While the method provides faster convergence for some rotation laws than the SCF method, other rotation laws produce similar convergence rates. Another method for modeling rotating stars is used by Collins & Smith (1985), who use 1D stellar models and apply three correction factors to account for all of the rotational distortion. Collins & Smith used their models to study the effects of differential rotation, with a cylindrical rotation law applied to A stars. A revised form of the SCF method was presented by Jackson, MacGregor, & Skumanich (2005), which now converges for masses less than 9 $M_\odot$.

1.1.2 INCLINATION CURVES

Studies by Hardorp & Strittmatter (1968b) show that energy transported in the atmosphere by meridional circulation of material is very small compared to the energy transported by radiation, and can be omitted from atmosphere calculations. Hardorp & Strittmatter state that, in general, constant-flux, plane-parallel atmospheres fitted at each point on the surface of the star, which does not consider energy transport due to circulation of material, are legitimate to model the atmosphere of a rotating star.

Collins (1963) was among the first to examine the effects of rotation on the deduced effective temperature and luminosity. In his examination he used the assumptions that the mass distribution follows that of a Roche model (the outer envelope has a potential derived from a centrally located mass), that rotation is solid body, and that energy-production is unaffected by rotation, and hence neither is luminosity. That allowed him to define the effective gravity as a function of colatitude, and then to use von Zeipel's theorem to obtain the effective temperature as a function of colatitude. He then used a gray atmosphere model, and found that the observed monochromatic magnitude changed up to a magnitude from inclination $i = 0$ to 90°. Roxburgh & Strittmatter (1965) find similar results as Collins (1963), but use the more detailed interior model of Roxburgh, Griffith, & Sweet (1965) with gray model atmospheres. Collins (1965) improved on his previous work by using a series of non-gray model atmospheres, finding even larger variations in luminosity with inclination than previously.

Maeder & Peytremann (1970) improved the realism of atmospheres modeled with local thermodynamic equilibrium (LTE), which had thus far only included continuum opacities, by incorporating hydrogen line opacities for the Balmer and Lyman series. Further improvements came when Slettebak, Kuzma, & Collins (1980) and Frémat, Zorec, Hubert, & Floquet (2005) created spectra of rotating stars using a series of non-LTE atmospheres. In most of the cases "gravity darkening", in one form or another, is used to describe the surface properties of a star. "Gravity darkening" is essentially the use of von Zeipel's theorem relating the effective gravity to the effective temperature. The approach requires some structure information, specifically the effective gravity as a function of colatitude. The simplest models postulate a point source gravitational potential with an assumed centrifugal potential. While atmospheres of rotating stars are clearly important in the observed quantities, Collins, Truax, & Cranmer (1991) state that the effects of rotation on the structure of the interior would likely play as large a role in determining the emergent spectrum as the rotational affects on the atmosphere.

Earlier work by Carroll (1928, 1933) and Shajn & Struve (1929) used limb darkening only and did not consider "gravity darkening". The work by Carroll and by Shajn & Struve was primarily focused on determining line widths as a function of $v \sin i$. Elvey (1930) used their results to calculate $v \sin i$ from observed line widths for the first time. Hardorp & Strittmatter (1968a) suggested that not including the effects of gravity darkening could lead to underestimating $v \sin i$ by as much as 40%. Collins & Truax (1995) later examined the classical treatment of rotational broadening and found that inappropriate values for limb darkening coefficients can lead to significant errors, even in moderately rotating stars.

Many of the above works have created inclination curves or rotation displacement fans while modeling rotating interiors and atmospheres. Rotation displacement fans are curves on the HR or color magnitude diagrams in luminosity versus effective temperature or color. They are curves that connect points of constant inclination and varying rotational velocity, while inclination curves connect points of constant rotational velocity and varying inclination. See figure 1.1 for an example of inclination curves and rotation displacement fans. Collins (1966) computed rotation displacement fans on a color magnitude diagram of M_v versus B-V. From figure 1.1 one can see that a rotating 12 $M_\odot$ model can easily have the same HR diagram location as a lower or higher mass non rotating star that is slightly evolved. This is the case for appreciable mass differences of up to 4 $M_\odot$. Hardorp & Strittmatter (1968b) computed inclination curves for 6 masses in the range of 1.5 to 8 $M_\odot$ from calcu-

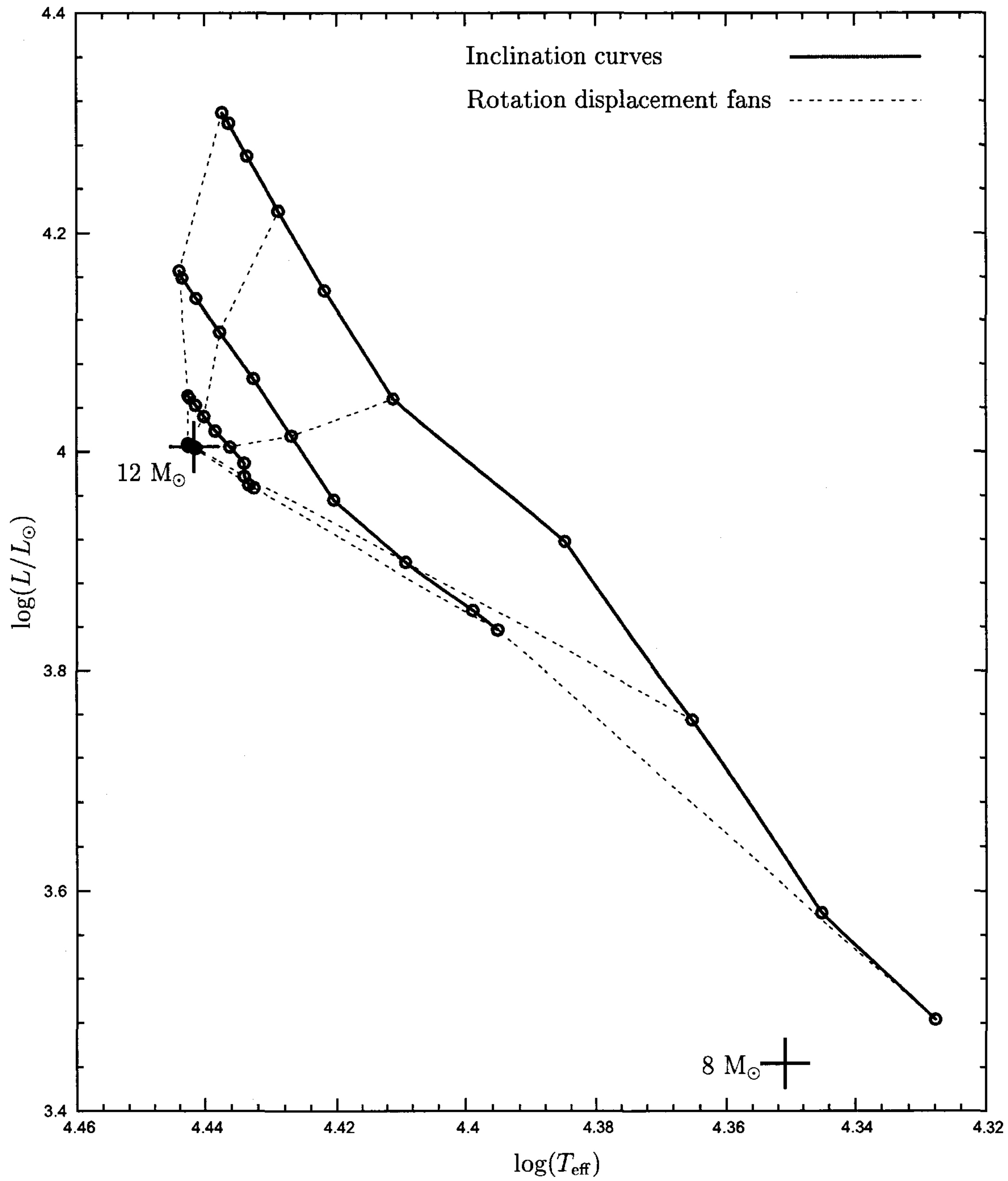

Figure 1.1: Shown are rotation displacement fans (dashed curves) and inclination curves (solid curves). Open circles indicate inclinations of 0° to 90° in steps of 10° from left to right along the inclination curves. The inclination curves are at 4 different surface equatorial velocities of 0, 210, 405, and 575 km s^{-1}. Crosses show non-rotating ZAMS models for 12 M$_\odot$ and 8 M$_\odot$. Data for these curves have been provided by Gillich (private communication).

lations based on von Zeipel's theorem. Maeder & Peytremann (1970) computed rotation displacement fans for 5, 2 and 1.4 $M_{\odot}$ models from atmospheres that included hydrogen lines of the Balmer and Lyman series. Collins, Truax, & Cranmer (1991) also computed rotational displacement fans, but obtained an effective gravity by assuming a Roche model and using von Zeipel's "gravity darkening" theorem. Townsend, Owocki, & Howarth (2004) computed rotation displacement fans using von Zeipel's theorem.

In general, when stellar interiors are handled in a more realistic way (Clement, 1974, 1978, 1979; Jackson, 1970) than simply using a Roche model or a 1D model with perturbations or corrections applied, the modeling of the stellar atmosphere is neglected and only a simple gray atmosphere is used. The reverse seems to be true for modeling atmospheres. The works cited here, which have used non-gray atmospheres and even non-LTE to compute inclination curves or rotation displacement fans, have all used von Zeipel's theorem to calculate the effective temperature as a function of colatitude. The present work uses inclination curves by Gillich (2007), which have the interior structure and the atmospheres both handled in detail. This was done using the fully 2D stellar structure and evolution code ROTORC (Deupree, 1990, 1995, 1998) and the stellar atmosphere code PHOENIX (Hauschildt & Baron, 1999), treating the atmospheres in non-LTE.

1.2 SYNTHETIC CLUSTERS

Synthetic clusters are synthetically generated HR diagrams representing the observed effective temperature and luminosity of cluster members. Such synthetic clusters are composed of individual points, each representing an observed star's HR diagram location. To generate a synthetic cluster, evolutionary tracks computed from stellar structure codes are interpolated to the desired mass and age. The age of the interpolated model is usually chosen to be the age of the cluster, and the masses of the models usually follow some initial mass function. A synthetic cluster is composed of many such interpolated models.

Synthetic clusters have not been as extensively studied as stellar interiors and atmospheres, though that is expected because synthetic clusters depend on the latter for their calculation. One of the first to compute a theoretical HR diagram was Sandage (1962), who computed theoretical HR diagrams for clusters of different ages. He then compared the theoretical HR diagrams for clusters to observed clusters to determine estimates of the ages of the observed clusters. The theoretical HR diagrams were constructed by connecting points of constant age among evolutionary tracks for stars of different masses. The lines then formed the theoretical HR diagram for a cluster at a given age. This method provided what was later referred to as an isochrone.

A more sophisticated approach was performed by Schlesinger (1969), who used a Salpeter initial mass function. To compute the location of the cluster members in the HR diagram, Schlesinger interpolated among tracks calculated by Iben (1965a,b, 1966a,b,c, 1967a,b). The interpolation was done among stages in the evolutionary tracks in which the time variation of luminosity and effective temperature was approximately linear. For example the section of the evolutionary track between the ZAMS and where half the initial central hydrogen is depleted was one stage of 10 stages that Schlesinger defined between the ZAMS and core-helium exhaustion. Meyer-Hofmeister (1969) constructed HR diagrams of synthetic clusters, and also considered the effects of a non-zero formation time on the synthetic clusters. Meyer-Hofmeister used a method similar to Schlesinger (1969) to linearly interpolate in mass between similar phases of evolution. Harris & Deupree (1976) used a method similar to Meyer-Hofmeister (1969) and Schlesinger (1969), in which the evolutionary tracks were divided into segments, the Salpeter (1955) mass function was imposed, and a non-zero formation time was used to compare with observed clusters.

Becker & Mathews (1983) took synthetic cluster generation one step further by not only interpolating in mass and age, but in metallicity and helium abundance as well. They constructed a three-dimensional grid of theoretical evolutionary tracks in Y, Z and mass. Becker & Mathews approached the construction of the synthetic clusters in a similar way to Schlesinger (1969), in that the evolutionary tracks were divided into sections. Tracks bracketing the desired composition and mass were interpolated in log Z to the desired log Z (at fixed Y and mass) resulting in $\log(age)$, $\log(T_e)$ and $\log(L/L_\odot)$ at the desired metallicity. This interpolation scheme was then repeated in log Y and in $\log M$.

In more recent years synthetic clusters have been almost entirely replaced with isochrones. Isochrones are curves of constant age on the HR diagram over a mass range. One of the first to use the term isochrone was Demarque (1967). To construct the isochrones in his paper, Demarque used 22 evolutionary tracks and 50 main-sequence models. Sandage & Eggen (1969) used isochrones to determine ages for clusters, and explored the effects of composition on the age estimates. Simpson et al. (1970) computed isochrones by interpolating evolutionary tracks in log mass. They then used the isochrones to estimate ages and distance to some galactic clusters. Mentioned here are some of the first workers to use isochrones. Isochrones have been extensively used up to present day to explore the features of star clusters.

Isochrones can be of great use for testing the theories of stellar evolution against observations of clusters and estimating properties of the clusters. However, in the present work, exploring the rotational effects on a cluster's HR diagram cannot use isochrones. The reason is that the HR diagram location of a cluster member now depends on the rotation and inclination of that particular member. Thus, an individual isochrone curve would be broadened into a sizeable (2100K) swath on the HR diagram. Rotation does not merely widen the main sequence; it also shifts the star parallel to the non-rotating main sequence depending on the star's inclination. As the rotation rate of a star is changed, the position of the star's inclination curve in the HR diagram is moved nearly perpendicular to the non-rotating main sequence. For different inclinations the observed effective temperature and luminosity move nearly parallel to the non-rotating main sequence along the inclination curve. Rotation rates of cluster members will not all be similar, but will cover a range of values. Also the inclination of a given cluster member may well be independent of those for other cluster members. For these reasons synthetic clusters are used and comparison with observed clusters must be done in a statistical manner.

There are two primary goals of this thesis. The first is to determine whether the width of the ZAMS well below the turnoff can be fit by the inclusion of rotation, and whether the width tells us something about the distribution of rotation among individual cluster members. The second is to determine if constraints may be placed on specific cluster members based on their relative positions in the cluster HR diagram. This work will use improved stellar interior models and more detailed atmosphere models than are often used in examining the stellar structure of rotating stars, and seldom ever used in conjunction with one another. As previously mentioned, this thesis will use inclination curves provided by Gillich (2007), who incorporated improved stellar interior models and detailed stellar atmospheres in his computations. These calculations handle "gravity darkening" without resorting to von Zeipel's theorem, and have limb darkening automatically built into the atmosphere calculation. Thus no *ad hoc* limb darkening or gravity darkening need to be employed.

To examine our second goal, we compute a number of synthetic clusters. Once a sample of synthetic clusters is created, the rotational characteristics of a selected member of the cluster, for example the hottest star in a cluster, can be examined to determine if the selected member has the expected rotation rate and inclination based on its HR diagram location. For example, if the hottest cluster member is at the age of the cluster we expect it to be a rapidly rotating star and seen pole-on because it has the longest inclination curve and a star seen pole-on occupies the hottest part of the inclination curve. Many synthetic clusters with rotation are created and the hottest member selected from each cluster and examined for its rotational characteristics. Thus, each synthetic cluster generated contributes one data point (e.g. the hottest star) to the sample. The sample size is the number of synthetic clusters generated. If the selected member is found to be rapidly rotating and seen pole-on, then it is included in the count of hottest stars that meet the specified criterion. The number of rapidly rotating hottest stars seen pole-on is then divided by the total number of synthetic clusters. This gives the fraction, which we shall define as C_f, of hottest stars that are rapidly rotating and seen pole-on within the clusters sampled. This method of calculating the fraction is also applied to the other types of selected members to quantify how many of the selected members meet the specified criterion

We use a modified version of the synthetic cluster code used by Harris & Deupree (1976), which interpolates among evolutionary tracks. It has been adapted to read in the ROTORC output data files, to interpolate in rotation rate, and to generate random inclinations. The code uses the same method for selecting masses and interpolating as a function of mass and age as Harris & Deupree (1976). Analytic expressions for the inclination curves were developed to specify the location of a cluster member in the HR diagram as it would be observed. Sections have been added to the code to allow one to create many synthetic clusters in quick succession and to specify the rotation and inclination distribution of the cluster members. A synthetic cluster allows one to specify the rotation rate, mass, age, and inclination of each individual cluster member and as such these quantities are known for each cluster member. In this study we assume that all members of the cluster have the same composition and the same age. Binaries have also been ignored and the rotating stellar models produced by ROTORC have solid body rotation on the ZAMS and only slight differential rotation in later stages of evolution due to local conservation of momentum during evolution. To compute C_f a C++ code was developed to sort the cluster members of a given synthetic cluster according to various characteristics (e.g. effective temperature descending) in order to identify selected cluster members (e.g. the hottest). This sorting is repeated for each cluster, and the selected member is tested against specific rotational criteria (e.g. rapidly rotating and viewed pole-on), and if they are met that cluster will increase C_f towards 1, and if they are not met will decrease C_f towards 0.

In chapter 2 the methods used for modeling a star's interior, computing the inclination curves and how they are then used to produce synthetic clusters are discussed. The results from the study are presented in chapter 3, including how the main sequence width is affected by varying rotation distributions, and C_fs are derived for the selected members under varying conditions. A comparison of the synthetic clusters to four observed clusters is made in chapter 4. Finally chapter 5 will discuss and summarize the results.

2 METHODS

This chapter describes the methods used to create a synthetic cluster of stars, with the rotational effects on the deduced effective temperature and luminosity included. The first section, "ROTORC", describes how this 2.5D stellar evolutionary code computes rotating stars. This section also discusses the settings used for calculating the evolution tracks used in this research. The next section, "Inclination Curves", describes how inclination curves, which are used to determine the position of a rotating star on the HR-diagram, are computed. Then, in the same section, there is a discussion of analytic inclination curves. Analytic inclination curves are expressions that have been determined by fits to mimic the relationship between the computed surface properties and the deduced inclination curves. Analytic inclination curves are used in place of the computed inclination curves in order to speed up the calculation time of the inclination curves and make this research feasible. The last section of this chapter, "Synthetic Cluster Generation", discusses how models within ROTORC evolution tracks are used to generate the observed properties of a synthetic cluster member. All of these facets coupled together allow the inclusion of rotational affects in the HR diagram of synthetic clusters.

2.1 ROTORC

Stellar structure models generated by ROTORC form the basis for all stellar structure information used in this research. This stellar structure information is used in computing inclination curves and generating the analytic inclination curves. The quantities required for the computed inclination curves are the effective temperature as a function of colatitude,

$T_{\text{eff}}(\theta)$, the fractional radius as a function of colatitude, $r(\theta)/R_{\text{eq}}$, the equatorial radius, R_{eq}, and the effective gravity, g_{eff}. Other quantities useful for comparison and interpretation are the ROTORC luminosity, the ROTORC average effective temperature, and the surface equatorial velocity. The ROTORC luminosity is the total energy output of the star. The ROTORC average effective temperature is defined as the black body temperature required to produce the ROTORC luminosity on a spherical surface that has the same surface area as the rotating spheroid. Stellar structure models over a range of ages form the evolutionary tracks among which the synthetic cluster code interpolates. In this section ROTORC is described along with how it was used in the current work.

2.1.1 INNER WORKINGS OF ROTORC

ROTORC is a 2.5D stellar evolution code written by Deupree (1990, 1995, 1998). ROTORC has been designed with the intention of studying instabilities that occur on varying time scales which redistribute angular momentum. To study the instabilities, ROTORC implicitly solves the time-dependent conservation laws for mass, momentum, energy, and composition, as well as Poisson's equation. Momentum is conserved in all 3 directions, r, θ, and ϕ. Azimuthal symmetry is assumed, meaning that the azimuthal velocity, v_ϕ, is symmetric about the rotation axis but does not have to be zero. Because symmetry is assumed in the azimuth co-ordinate, it is not a true 3D calculation; however it is not strictly a 2D calculation either as momentum conservation is required in all 3 dimensions. The usual designation for this type of calculation is 2.5 dimensions.

ROTORC uses the fractional radius, $x = r/R$, where r is the local radius and R is the largest radius (usually the equatorial radius), instead of the mass interior to r, M_r, as the radial independent variable. Though M_r is an excellent independent variable for spherical stars because it is Lagrangian, it is not for non-spherical stars. That is because it is difficult to relate M_r to r for a non-spherical density distribution. Simply using r as the independent variable creates difficulties because the star can change its radius by a factor of 100 throughout its evolution, making it difficult to get good zoning for all parts of the star's evolution. The choice of x as an independent variable means the co-ordinate system is neither Lagrangian nor Eulerian but what is referred to as Euler-Lagrange. The second independent variable is θ, the colatitude which is an Eulerian variable. Given these assumptions and restrictions, and following Deupree (1990) we write the conservation equations. Mass conservation is given by:

$$R\frac{\partial \rho}{\partial t} + (v_r - V_0)\frac{\partial \rho}{\partial x} + \frac{v_\theta}{x}\frac{\partial \rho}{\partial \theta} + \frac{\rho}{x^2}\frac{\partial}{\partial x}\left(x^2 v_r\right) + \frac{\rho}{x\sin\theta}\frac{\partial}{\partial \theta}\left(v_\theta \sin\theta\right) = 0, \tag{2.1}$$

where ρ is the density, t the time, v_r the radial component of the velocity , V_0 the radial velocity of the co-ordinate system, and v_θ the θ component of the velocity. Momentum conservation in r direction is given by:

$$R^2\frac{\partial v_r}{\partial t} + R\left(v_r - V_0\right)\frac{\partial v_r}{\partial x} + \frac{R v_\theta}{x}\frac{\partial v_r}{\partial \theta} + \frac{R}{\rho}\frac{\partial P}{\partial x} + R\frac{\partial \Phi}{\partial x} - R\frac{v_\phi^2}{x} - R\frac{v_\theta^2}{x} = 0, \tag{2.2}$$

where v_ϕ is the component of the velocity in the ϕ direction and Φ is the gravitational potential. Momentum conservation in θ direction is given by:

$$R^2\frac{\partial v_\theta}{\partial t} + R\left(v_r - V_0\right)\frac{\partial v_\theta}{\partial x} + \frac{R v_\theta}{x}\frac{\partial v_\theta}{\partial \theta} + \frac{R}{\rho x}\frac{\partial P}{\partial \theta} + \frac{R}{x}\frac{\partial \Phi}{\partial \theta} - R\frac{v_\phi^2}{x}\cot\theta + R\frac{v_r v_\theta}{x} = 0. \tag{2.3}$$

Momentum conservation in the ϕ direction is given by:

$$R^2 \frac{\partial v_\phi}{\partial t} + R\left(v_r - V_0\right) \frac{\partial v_\phi}{\partial x} + \frac{R v_\theta}{x} \frac{\partial v_\phi}{\partial \theta} + R \frac{v_r v_\theta}{x} + R \frac{v_\theta v_\phi}{x} \cot\theta = 0. \tag{2.4}$$

Conservation of energy is given by:

$$\begin{aligned} R^2 \frac{\partial E}{\partial t} + R\left(v_r - V_0\right) \frac{\partial E}{\partial x} + \frac{R v_\theta}{x} \frac{\partial E}{\partial \theta} - \frac{R^2 P}{\rho x^2} \frac{\partial}{\partial x}\left(x^2 v_r\right) - \frac{R^2 P}{\rho x \sin\theta} \frac{\partial}{\partial \theta}\left(v_\theta \sin\theta\right) - R^2 \epsilon \\ - \frac{4\sigma}{3\rho x^2} \frac{\partial}{\partial x}\left(\frac{x^2}{\rho\kappa} \frac{\partial T^4}{\partial x}\right) - \frac{4\sigma}{3\rho x^2 \sin\theta} \frac{\partial}{\partial \theta}\left(\frac{\sin\theta}{\kappa\rho} \frac{\partial T^4}{\partial \theta}\right) = 0, \end{aligned} \tag{2.5}$$

where E is the specific internal energy, T the temperature, P the pressure, σ the Boltzmann constant, and κ the opacity. The gravitational potential, Φ, is obtained from Poisson's equation:

$$\frac{1}{x^2} \frac{\partial}{\partial x}\left(x^2 \frac{\partial \Phi}{\partial x}\right) + \frac{1}{x^2 \sin\theta} \frac{\partial}{\partial \theta}\left(\sin\theta \frac{\partial \Phi}{\partial \theta}\right) - 4\pi G \rho R^2 = 0. \tag{2.6}$$

Conservation of the hydrogen mass fraction (X) is given by:

$$R \frac{\partial X}{\partial t} + \left(v_r - V_0\right) \frac{\partial X}{\partial x} + \frac{v_\theta}{x} \frac{\partial X}{\partial \theta} + q = 0, \tag{2.7}$$

with q being the nuclear destruction rate of hydrogen.

The boundary conditions at the stellar center are given by:

$$\frac{\partial P}{\partial r} = 0 \text{ at } r = 0, \tag{2.8}$$

$$\text{Radial flux} = 0 \text{ at } r = 0, \tag{2.9}$$

and

$$\frac{\partial \Phi}{\partial r} = 0 \text{ at } r = 0. \tag{2.10}$$

At the stellar surface the boundary conditions are

$$\rho = \rho_{ref}, \tag{2.11}$$

where ρ_{ref} is a chosen density cut off. The flux at the surface, F_s, can be related to the surface temperature, T_s, by using $F_s = \sigma T_{\text{eff}}^4$ in conjunction with the equation for the temperature structure of a plane parallel gray atmosphere in LTE:

$$T^4 = \frac{3}{4} T_{\text{eff}}^4 \left(\tau + \frac{2}{3}\right); \tag{2.12}$$

producing at the surface ($\tau = 0$) $F_s = 2\sigma T_s^4$.

The boundary condition for the potential is defined on a spherical surface just exterior to the star at the largest radius. This external gravitational potential, Φ_{ext}, is evaluated using the method outlined in Deupree (1974). The method depends on the assumption of azimuthal symmetry by assuming that the density distribution can be represented as a large number of uniform density rings perpendicular to the rotation axis. The finite difference form of the solution for the external potential, $\Phi_{ext,k}$, on a spherical surface with radius just exterior to R at angle θ_k from the pole is:

$$\Phi_{ext,k} = R^2 \sum_i \sum_j \rho_{ij} G_{ijk}, \tag{2.13}$$

where ρ_{ij} is the density in the zone at radius x_i and at angle θ_j. The G_{ijk}'s include all the geometrical factors. The G_{ijk}'s depend only on the zoning and need to be calculated once for a given (x, θ) zoning. The zoning is not changed in this work because we only consider core hydrogen burning and the very early phases of hydrogen shell burning for which the given zoning is adequate. The boundary condition for the potential on this spherical surface thus becomes:

$$\Phi = \Phi_{ext}. \tag{2.14}$$

The potential at the surface of the star is determined by solving Poison's equation (equation 2.6) from this spherical surface back to the star's surface.

At $\theta = 0$ and $\pi/2$, because of equatorial and azimuthal symmetry assumptions, $v_\theta = 0$. That is because, if v_θ were non-zero, material would flow across the symmetry boundaries, which would violate the symmetry assumption. Also the symmetry assumption at $\theta = 0$ and $\theta = \pi/2$ means that:

$$\frac{\partial \rho}{\partial \theta} = \frac{\partial T}{\partial \theta} = \frac{\partial \Phi}{\partial \theta} = \frac{\partial v_r}{\partial \theta} = \frac{\partial v_\phi}{\partial \theta} = 0, \tag{2.15}$$

in order to assure that the dependent variables are continuous functions of θ across the symmetry boundary. We solve for R from the conservation of total mass, M, in the following way:

$$M - 2\pi R^3 \int_{x=0}^{1} \int_{\theta=0}^{\pi} \rho x^2 \sin\theta d\theta dx = 0, \tag{2.16}$$

with the finite difference form having the double integral replaced by a sum over all the zones in the 2D mesh. To locate the surface at all angles, it is assumed that the model's surface is an equipotential surface of the total potential, ψ, the gravitational potential plus the centrifugal potential, given by:

$$\psi = \Phi - \frac{1}{2}v_\phi^2. \tag{2.17}$$

ψ is computed at $x = 1$. The surface is defined at other angles in the radial zones with ψ closest to the value computed at $x = 1$.

Hydrodynamic calculations are usually preformed in one of two ways, explicitly or implicitly. The difference between the two methods is how certain terms are handled. Consider the following differential equation:

$$\frac{\partial f}{\partial x} = g(x, f). \tag{2.18}$$

In finite difference form the equation can be represented as:

$$\frac{f^{n+1} - f^n}{\Delta x} = g(x, f^n), \tag{2.19}$$

the explicit form, or

$$\frac{f^{n+1} - f^n}{\Delta x} = g(x, f^{n+1}), \tag{2.20}$$

the implicit form. The value of f is known at state n and the value of f is sought at some new state $n + 1$. The explicit representation of the differential equation can easily and directly be solved for f^{n+1}. The implicit formulation on the other hand must solve for f^{n+1} by solving a much more complex equation. When converting from differential equations to finite difference representations the discretization introduces numerical instabilities. The implicit calculation places an additional constraint on the solution, f^{n+1}, by requiring it to satisfy the finite difference equation on both the right and left hand sides of the equation. This reduces the tendency of producing solutions that are not consistent with the true solution of the differential equations as Δx becomes larger.

In the case that x is the time variable and g represents the conservation equations, the stability constraint for the explicit representation is known as the Courant condition (Richtmyer & Morton, 1957). The Courant condition requires the time step to be chosen such that a sound wave does not completely cross any particular zone within one time step. The sound speed, c, in an ideal gas is given as:

$$c = \sqrt{\gamma \frac{P}{\rho}} \tag{2.21}$$

where γ is the ratio of the specific heat at constant-pressure over the specific heat at constant-volume, P is the pressure and ρ is the density of the gas. If the flow of interest is well subsonic ($v_{gas} \approx 2 \times 10^{-8}$ km s$^{-1} \ll c \approx 200$ km s^{-1}), as it is here, the Courant condition imposes too tight a constraint to make explicit solutions feasible over the time periods desired. Equation 2.20, the implicit form, has no constraint equivalent to the Courant condition.

ROTORC is fully implicit, and as such there is no stability constraint on the time step as for explicit calculations. However, there are accuracy constraints on the time step. If the conservation equations are used to follow the evolution of the convective core in an accurate manner, the time scales would be on the order of the convective flow patterns. This time scale is far too short compared with the stellar evolutionary time scale, and one could not hope to follow the evolution of a star this way. Instead the usual procedure for treating convective cores is used. This procedure forces the logarithmic gradient of the temperature with respect to pressure to be a minimum of the radiative and adiabatic gradients, i.e.:

$$\frac{d\ln T}{d\ln P} = \min(\nabla_{ad}, \nabla_{rad}). \tag{2.22}$$

To implement it either equation (2.5) would need to be replaced with an equation not suitable for following the hydrodynamic evolution of the convective core or equation (2.5) would need to be altered to be compatible with the procedure for handling the logarithmic gradient of temperature with respect to pressure (2.22). The former solution requires switching between two equations: one suitable for hydrodynamic calculations and one suitable for stellar evolution calculations. A switch from following stellar evolution to following hydrodynamic evolution may not necessarily satisfy both equations at the time of the switch, and could generate unrealistic results. So that the adiabatic temperature gradient in the convective region is enforced, the opacity in equation (2.5) is altered to:

$$\kappa_{\text{eff}} = \kappa \cdot (\nabla_{ad}/\nabla_{rad}) \text{ if } \nabla_{ad} \leq \nabla_{rad}, \tag{2.23}$$

where κ is the usual radiative opacity. This imposes the adiabatic condition of equation 2.22 when appropriate.

Once the differential equations and boundary conditions are fully specified, the remaining step is to develop a solution algorithm. To do so ROTORC uses a two-dimensionalization of the Henyey method (Henyey, Forbes, & Gould, 1964) to solve equations (2.1)-(2.7). The implementation of the Henyey method is described below. The concept behind the Henyey method is successive corrections to an initial guess for the dependent variables. The corrections are recalculated using the current solution for the dependent variables and applied to the current solution producing an updated solution; the process is repeated until the corrections are smaller than some predefined amount.

The corrections are calculated first by taking the partial derivatives of the finite difference forms of equations (2.1)-(2.7) with respect to the dependent variables (ρ, T, v_r, v_θ, v_ϕ, Φ, Φ_{ext} and R). The partial derivatives describe how the difference equations change as the dependent variables change. Let the partial derivatives of the finite difference form of equations (2.1)-(2.7), evaluated at the i^{th} radial and the j^{th} angular zone with respect to the dependent variable in the l^{th} radial and m^{th} angular zone, be written as a matrix, $\mathbf{J}^{i,j}_{l,m}$. The matrix is known as the Jacobian of the system and has the form:

$$\mathbf{J}^{i,j}_{l,m} = \begin{pmatrix} \frac{\partial(eq.\ 2.1)_{i,j}}{\partial\rho_{l,m}} & \frac{\partial(eq.\ 2.1)_{i,j}}{\partial T_{l,m}} & \cdots \\ \frac{\partial(eq.\ 2.2)_{i,j}}{\partial\rho_{l,m}} & \frac{\partial(eq.\ 2.2)_{i,j}}{\partial T_{l,m}} & \cdots \\ \vdots & \vdots & \ddots \end{pmatrix}. \qquad (2.24)$$

$\mathbf{J}^{i,j}_{l,m}$ is an $N_{\rm eq} \times N_{\rm eq}$ matrix where $N_{\rm eq}$ is the number of equations (in this case, seven). If the corrections to the dependent variables in the l, m^{th} zone are written as the vector:

$$\delta\mathbf{q}_{l,m} = \begin{pmatrix} \delta\rho_{l,m} \\ \delta T_{l,m} \\ \delta v_{r,l,m} \\ \delta v_{\theta,l,m} \\ \delta v_{\phi,l,m} \\ \delta\Phi_{l,m} \\ \delta X_{l,m} \end{pmatrix}, \qquad (2.25)$$

and the finite difference equations evaluated with the initial guess for the dependent variables at the i, j^{th} zone are written as the vector:

$$\mathbf{Q}^{i,j} = \begin{pmatrix} (eq.\ 2.1)_{i,j} \\ (eq.\ 2.2)_{i,j} \\ \vdots \\ (eq.\ 2.7)_{i,j} \end{pmatrix}, \tag{2.26}$$

then the equation:

$$\mathbf{Q}^{i,j} + \sum_{l,m} \mathbf{J}^{i,j}_{l,m} \delta \mathbf{q}_{l,m} = 0, \tag{2.27}$$

can be solved for the corrections.

In the case of the 2D model described by second order conservation equations, the i, j^{th} zone will depend on only some of the other zones. In particular it will depend on the neighboring zones in θ and x. Equation (2.27) for the i, j^{th} zone then becomes:

$$\mathbf{J}^{i,j}_{i-1,j}\delta\mathbf{q}_{i-1,j} + \mathbf{J}^{i,j}_{i,j-1}\delta\mathbf{q}_{i,j-1} + \mathbf{J}^{i,j}_{i,j}\delta\mathbf{q}_{i,j} + \mathbf{J}^{i,j}_{i+1,j}\delta\mathbf{q}_{i+1,j} + \mathbf{J}^{i,j}_{i,j+1}\delta\mathbf{q}_{i,j+1} + \mathbf{Q}^{i,j} = 0. \tag{2.28}$$

Note that the corrections solved for with this equation will not yield the exact solution for the dependent variables immediately, because equation 2.27 keeps only the terms to first order in $\delta\mathbf{q}$. If one considers the Taylor expansion of a function, $f(x)$, about a point, a, the expansion is given by:

$$f(x) = f(a) + f'(a)(x-a) + \frac{f''}{2!}(a)(x-a)^2 + \cdots, \tag{2.29}$$

where f' and f'' denote the first and second derivatives of f. This is similar to the Henyey method, with f as the differential equation, a as the initial guess for the dependent variable, $x - a$ as the correction, $f(a)$ as the differential equations evaluated at the initial guess, and f' representing the Jacobian. Equations (2.27) and (2.28) are the linearization of this expansion and become closer to an equality as δq becomes smaller. The process can be continued using the updated guess for the dependent variables until all $\delta \mathbf{q}$ approach zero within some tolerance.

Equations (2.1)-(2.7) also depend on the total radius of the star. This is unknown and must be treated as another perturbable dependent variable. Equations (2.1)-(2.7) must have their partial derivatives taken with respect to R as well forming the vector,

$$\mathbf{P}^{i,j} = \begin{pmatrix} \frac{\partial (eq.\ 2.1)_{i,j}}{\partial R} \\ \frac{\partial (eq.\ 2.2)_{i,j}}{\partial R} \\ \vdots \end{pmatrix}. \tag{2.30}$$

The revised form of equation (2.28) can be written as:

$$\mathbf{J}^{i,j}_{i-1,j}\delta\mathbf{q}_{i-1,j} + \mathbf{J}^{i,j}_{i,j-1}\delta\mathbf{q}_{i,j-1} + \mathbf{J}^{i,j}_{i,j}\delta\mathbf{q}_{i,j} + \mathbf{J}^{i,j}_{i,j+1}\delta\mathbf{q}_{i+1,j} + \mathbf{J}^{i,j}_{i+1,j}\delta\mathbf{q}_{i,j+1} + \mathbf{P}^{i,j}\delta R + \mathbf{Q}^{i,j} = 0. \tag{2.31}$$

The equation for the external potential, equation (2.13), also needs to be included. The partial derivatives of equation (2.13) at the k^{th} angular zone on the spherical surface exterior to the model are taken with respect to the dependent variables listed in $\delta q_{l,m}$, giving the row vector of length N_{eq} with only one non-zero entry:

$$\mathbf{A}^{k}_{l,m} = \begin{pmatrix} \frac{\partial (eq.2.13)_k}{\partial \rho_{l,m}} & 0 & \cdots & 0 \end{pmatrix}. \tag{2.32}$$

This is analogous to $\mathbf{J}_{l,m}^{i,j}$ except that there is only one equation, causing it to be a row vector. The zeroes come about because equation (2.13) depends only on all the $\rho_{l,m}$'s and not on the other dependent variables in $\delta\mathbf{q}_{l,m}$. The external potential at each angular zone, k, is also a dependent quantity, and equation (2.13) must be partially differentiated with respect to $\Phi_{ext,k}$ as well. Let the partial differential be denoted as:

$$B^k = \frac{\partial(eq.\ 2.13)_k}{\partial\Phi_{ext,k}}. \tag{2.33}$$

Equation (2.13) also depends on R, thus the partial derivative with respect to R is taken, giving the scalar:

$$C^k = \frac{\partial(eq.\ 2.13)_k}{\partial R}. \tag{2.34}$$

If equation (2.13), evaluated with the initial guess at zone k, is denoted as D^k, then the following can be written for the external potential:

$$\sum_{l=1}^{N_r}\sum_{m=1}^{N_\theta} \mathbf{A}_{l,m}^k \delta\mathbf{q}_{l,m} + B^k\delta\Phi_{ext,k} + C^k\delta R + D^k = 0. \tag{2.35}$$

Finally, the finite difference form of the equation for the total mass (equation 2.16) must be included. This also depends on $\rho_{l,m}$ and R. It gives the row vector and scalar of the forms:

$$\mathbf{E}_{l,m} = \begin{pmatrix} \frac{\partial(eq.\ 2.16)}{\partial\rho_{l,m}} & 0 & \cdots \end{pmatrix}, \tag{2.36}$$

and

$$F = \frac{\partial(eq.\ 2.16)}{\partial R}. \tag{2.37}$$

Letting equation (2.16), evaluated with the initial guess, be G produces:

$$\sum_{l=1}^{N_r}\sum_{m=1}^{N_\theta}\mathbf{E}_{l,m}\delta\mathbf{q}_{l,m}+F\delta R+G=0. \tag{2.38}$$

There are now 3 sets of equations. The first set (equation 2.28) is a set of $N_{\text{eq}} \times N_r \times N_\theta$ equations, the second set (equation 2.35) is a set of N_θ equations, and the third set (equation 2.38) is a single equation. The equations can be combined into a single giant matrix equation containing all the equations at all of the zones, perturbed (having their partial derivatives taken) with respect to all the unknowns. Let the giant matrix containing all the coefficients to the corrections be denoted by the square matrix $\mathbf{Y}$ of size $N_{\text{eq}} \times N_\theta \times N_r + N_\theta + 1$. Let all the corrections ($\delta\mathbf{q}_{l,m}$, $\delta\Phi_{ext,k}$ and δR) be placed in a column vector $\delta\mathbf{q}_{all}$ of length $N_{\text{eq}} \times N_\theta \times N_r + N_\theta + 1$. Let the residues ($\mathbf{Q}^{i,j}$, D^k and G) be placed in a column vector, $\mathbf{Z}$ of length $N_{\text{eq}} \times N_\theta \times N_r + N_\theta + 1$. Then the system of equations can be written as:

$$\mathbf{Y}\delta\mathbf{q}_{all}=\mathbf{Z}. \tag{2.39}$$

To clarify the situation, $\mathbf{Y}$, $\delta\mathbf{q}_{all}$ and $\mathbf{Z}$ have been written out for $N_r = N_\theta = 3$. The matrix

$\mathbf{Y}$ is given by:

$$\mathbf{Y} =$$

$$\left(\begin{array}{c|c|c|c|c|c|c|c|c|c|c|c|c}
\mathbf{J}^{1,1}_{1,1} & \mathbf{J}^{1,1}_{1,2} & & \mathbf{J}^{1,1}_{2,1} & & & & & & & & & \mathbf{P}^{1,1} \\ \hline
\mathbf{J}^{1,2}_{1,1} & \mathbf{J}^{1,2}_{1,2} & \mathbf{J}^{1,2}_{1,3} & & \mathbf{J}^{1,2}_{2,2} & & & & & & & & \mathbf{P}^{1,2} \\ \hline
& \mathbf{J}^{1,3}_{1,2} & \mathbf{J}^{1,3}_{1,3} & & & \mathbf{J}^{1,3}_{2,3} & & & & & & & \mathbf{P}^{1,3} \\ \hline
\mathbf{J}^{2,1}_{1,1} & & & \mathbf{J}^{2,1}_{2,1} & \mathbf{J}^{2,1}_{2,2} & & \mathbf{J}^{2,1}_{3,1} & & & & & & \mathbf{P}^{2,1} \\ \hline
& \mathbf{J}^{2,2}_{1,2} & & \mathbf{J}^{2,2}_{2,1} & \mathbf{J}^{2,2}_{2,2} & \mathbf{J}^{2,2}_{2,3} & & \mathbf{J}^{2,2}_{3,2} & & & & & \mathbf{P}^{2,2} \\ \hline
& & \mathbf{J}^{2,3}_{1,3} & & \mathbf{J}^{2,3}_{2,2} & \mathbf{J}^{2,3}_{2,3} & & & \mathbf{J}^{2,3}_{3,3} & & & & \mathbf{P}^{2,3} \\ \hline
& & & \mathbf{J}^{3,1}_{2,1} & & & \mathbf{J}^{3,1}_{3,1} & \mathbf{J}^{3,1}_{3,2} & & \mathbf{J}^{3,1}_{ext,1} & & & \mathbf{P}^{3,1} \\ \hline
& & & & \mathbf{J}^{3,2}_{2,2} & & \mathbf{J}^{3,2}_{3,1} & \mathbf{J}^{3,2}_{3,2} & \mathbf{J}^{3,2}_{3,3} & & \mathbf{J}^{3,2}_{ext,2} & & \mathbf{P}^{3,2} \\ \hline
& & & & & \mathbf{J}^{3,3}_{2,3} & & \mathbf{J}^{3,3}_{3,2} & \mathbf{J}^{3,3}_{3,3} & & & \mathbf{J}^{3,3}_{ext,3} & \mathbf{P}^{3,3} \\ \hline
\mathbf{A}^{1}_{1,1} & \mathbf{A}^{1}_{1,2} & \mathbf{A}^{1}_{1,3} & \mathbf{A}^{1}_{2,1} & \mathbf{A}^{1}_{2,2} & \mathbf{A}^{1}_{2,3} & \mathbf{A}^{1}_{3,1} & \mathbf{A}^{1}_{3,2} & \mathbf{A}^{1}_{3,3} & B^{1} & & & C^{1} \\ \hline
\mathbf{A}^{2}_{1,1} & \mathbf{A}^{2}_{1,2} & \mathbf{A}^{2}_{1,3} & \mathbf{A}^{2}_{2,1} & \mathbf{A}^{2}_{2,2} & \mathbf{A}^{2}_{2,3} & \mathbf{A}^{2}_{3,1} & \mathbf{A}^{2}_{3,2} & \mathbf{A}^{2}_{3,3} & & B^{2} & & C^{2} \\ \hline
\mathbf{A}^{3}_{1,1} & \mathbf{A}^{3}_{1,2} & \mathbf{A}^{3}_{1,3} & \mathbf{A}^{3}_{2,1} & \mathbf{A}^{3}_{2,2} & \mathbf{A}^{3}_{2,3} & \mathbf{A}^{3}_{3,1} & \mathbf{A}^{3}_{3,2} & \mathbf{A}^{3}_{3,3} & & & B^{3} & C^{3} \\ \hline
\mathbf{E}_{1,1} & \mathbf{E}_{1,2} & \mathbf{E}_{1,3} & \mathbf{E}_{2,1} & \mathbf{E}_{2,2} & \mathbf{E}_{2,3} & \mathbf{E}_{3,1} & \mathbf{E}_{3,2} & \mathbf{E}_{3,3} & & & & F
\end{array}\right), \tag{2.40}$$

where all the blank elements are zero and the $\mathbf{J}^{i,j}_{ext,k}$ are given by:

$$\mathbf{J}^{i,j}_{ext,k} = \begin{pmatrix} \frac{\partial(eq.\ 2.1)_{i,j}}{\partial \Phi_{ext,k}} \\ \frac{\partial(eq.\ 2.2)_{i,j}}{\partial \Phi_{ext,k}} \\ \vdots \end{pmatrix}. \tag{2.41}$$

The matrix $\mathbf{Y}$ was created by stepping through the i, j mesh by first stepping through angular zones $j = 1-3$ for $i = 1$ and then incrementing the radial zone by one and stepping through all the angular zones, continuing in that manner until all of the zones have been evaluated. It is helpful to keep in mind that each $\mathbf{J}^{i,j}_{l,m}$ is an $N_{\rm eq} \times N_{\rm eq}$ matrix, each $\mathbf{P}^{i,j}$ is a column vector of length $N_{\rm eq}$, each $\mathbf{A}^{k}_{l,m}$ and $\mathbf{E}_{l,m}$ are row vectors of length $N_{\rm eq}$, and each B^k, C^k and F are scalars. $\delta\mathbf{q}_{all}$ and $\mathbf{Z}$ are given by:

$$\delta\mathbf{q}_{all} = \begin{pmatrix} \delta\mathbf{q}_{1,1} \\ \delta\mathbf{q}_{1,2} \\ \delta\mathbf{q}_{1,3} \\ \delta\mathbf{q}_{2,1} \\ \delta\mathbf{q}_{2,2} \\ \delta\mathbf{q}_{2,3} \\ \delta\mathbf{q}_{3,1} \\ \delta\mathbf{q}_{3,2} \\ \delta\mathbf{q}_{3,3} \\ \delta\Phi_{ext,1} \\ \delta\Phi_{ext,2} \\ \delta\Phi_{ext,3} \\ \delta R \end{pmatrix}, \tag{2.42}$$

and

$$\mathbf{Z} = \begin{pmatrix} \mathbf{Q}^{1,1} \\ \mathbf{Q}^{1,2} \\ \mathbf{Q}^{1,3} \\ \mathbf{Q}^{2,1} \\ \mathbf{Q}^{2,2} \\ \mathbf{Q}^{2,3} \\ \mathbf{Q}^{3,1} \\ \mathbf{Q}^{3,2} \\ \mathbf{Q}^{3,3} \\ D^1 \\ D^2 \\ D^3 \\ G \end{pmatrix}. \tag{2.43}$$

The matrix $\mathbf{Y}$ has many zero elements in the upper $N_{\text{eq}} \times N_\theta \times N_r$ rows, which aid in the solution of $\delta\mathbf{q}_{all}$. The knowledge of the zero elements can be used to avoid a number of computational steps involved in solving the system of equations. To illustrate the method, the first few steps are followed. If interior boundary conditions are applied to equation (2.28) with $i = j = 1$ then:

$$\mathbf{J}^{1,1}_{1,1}\delta q_{1,1} + \mathbf{J}^{1,1}_{1,2}\delta\mathbf{q}_{1,2} + \mathbf{J}^{1,1}_{2,1}\delta q_{2,1} + \mathbf{P}^{1,1}\delta R + \mathbf{Q}^{1,1} = 0. \tag{2.44}$$

Solving equation (2.44) for $\delta \mathbf{q}_{1,1}$ gives:

$$\delta \mathbf{q}_{1,1} = \alpha_{1,1}^{1} \delta \mathbf{q}_{1,2} + \alpha_{1,1}^{N_\theta} \delta \mathbf{q}_{2,1} + \beta_{1,1} \delta R + \gamma_{1,1}, \tag{2.45}$$

where

$$\begin{aligned} \alpha_{1,1}^{1} &= -(\mathbf{J}_{1,1}^{1,1})^{-1} \mathbf{J}_{1,2}^{1,1}, \\ \alpha_{1,1}^{N_\theta} &= -(\mathbf{J}_{1,1}^{1,1})^{-1} \mathbf{J}_{2,1}^{1,1}, \\ \beta_{1,1} &= -(\mathbf{J}_{1,1}^{1,1})^{-1} \mathbf{P}^{1,1}, \\ \text{and} \quad \gamma_{1,1} &= -(\mathbf{J}_{1,1}^{1,1})^{-1} \mathbf{Q}^{1,1}. \end{aligned} \tag{2.46}$$

The α's are $N_{\text{eq}} \times N_{\text{eq}}$ matrices, and β and γ are column vectors of length N_{eq}. For $i = 1$, $j = 2$, equation (2.28) becomes:

$$\mathbf{J}_{1,1}^{1,2} \delta q_{1,1} + \mathbf{J}_{1,2}^{1,2} \delta \mathbf{q}_{1,2} + \mathbf{J}_{1,3}^{1,2} \delta \mathbf{q}_{1,3} + \mathbf{J}_{2,2}^{1,2} \delta \mathbf{q}_{2,2} + \mathbf{P}^{1,2} \delta R + \mathbf{Q}^{1,2} = 0. \tag{2.47}$$

By substitution in equation (2.45) for $\delta \mathbf{q}_{1,1}$ in equation (2.47), the following is obtained:

$$\delta \mathbf{q}_{1,2} = \alpha_{1,2}^{1} \delta \mathbf{q}_{1,3} + \alpha_{1,2}^{N_\theta - 1} \delta \mathbf{q}_{2,1} + \alpha_{1,2}^{N_\theta} \delta \mathbf{q}_{2,2} + \beta_{1,2} \delta R + \gamma_{1,2}, \tag{2.48}$$

Where:

$$\begin{aligned} \alpha_{1,2}^{1} &= -(\mathbf{J}_{1,2}^{1,2} + \mathbf{J}_{1,1}^{1,2} \alpha_{1,1}^{1})^{-1} (\mathbf{J}_{1,3}^{1,2}), \\ \alpha_{1,2}^{N_\theta - 1} &= -(\mathbf{J}_{1,2}^{1,2} + \mathbf{J}_{1,1}^{1,2} \alpha_{1,1}^{1})^{-1} (\mathbf{J}_{1,1}^{1,2} \alpha_{1,1}^{N_\theta}), \\ \alpha_{1,2}^{N_\theta} &= -(\mathbf{J}_{1,2}^{1,2} + \mathbf{J}_{1,1}^{1,2} \alpha_{1,1}^{1})^{-1} (\mathbf{J}_{2,2}^{1,2}), \\ \beta_{1,2} &= -(\mathbf{J}_{1,2}^{1,2} + \mathbf{J}_{1,1}^{1,2} \alpha_{1,1}^{1})^{-1} (\mathbf{P}^{1,2} + \mathbf{J}_{1,1}^{1,2} \beta_{1,1}), \\ \text{and} \quad \gamma_{1,2} &= -(\mathbf{J}_{1,2}^{1,2} + \mathbf{J}_{1,1}^{1,2} \alpha_{1,1}^{1})^{-1} (\mathbf{Q}^{1,2} + \mathbf{J}_{1,1}^{1,2} \gamma_{1,1}). \end{aligned} \tag{2.49}$$

Note the range of the upper index of the α's. The index starts at 1 and continues to

N_θ. In equation (2.45) there are no non-zero α's between 1 and N_θ, but as the process of elimination is repeated the α's will be filled in. In general:

$$\delta\mathbf{q}_{i,j} = \alpha^1_{i,j}\delta\mathbf{q}_{i,j+1} + \cdots + \alpha^{N_\theta}_{i,j}\delta\mathbf{q}_{i+1,j} + \beta_{i,j}\delta R + \gamma_{i,j}. \tag{2.50}$$

The terms excluded correspond to the $\delta\mathbf{q}$'s of the zones stepped through, starting at the i, j^{th} zone, and stepping through the angular direction, j, and then the radial direction, i, until $\delta\mathbf{q}_{i+1,j}$ is reached.

Once the first N_θ rows of the matrix have been processed via the above method, the first N_θ rows will have the terms left and below the diagonal reduced to zeros, with 1's along the diagonal. For the next $N_\theta \times (N_r - 1)$ rows with $i > 1$, the process will have to be repeated N_θ times instead of just once. That is because the term from the adjacent interior radial zone $(i-1, j)$ is no longer removed because of the boundary conditions. Because the new term is N_θ elements away from the diagonal, it requires the steps leading to equation (2.49) to be repeated N_θ times using the previous N_θ rows. For the last $N_\theta + 1$ rows, coming from equation (2.13) for the external potential and equation (2.16) for the total mass, the steps leading to equation (2.49) must be repeated $N_\theta \times N_r$ times because they will have no non-zero terms.

From the surface, global, and external boundary conditions, the last N_θ $\delta\mathbf{q}_{i,j}$'s can be eliminated and $\delta\mathbf{q}_{N_r,N_\theta}$ can be solved for. Equation (2.50) can now be used to back step to solve for all $\delta\mathbf{q}_{i,j}$'s. If the corrections $(\delta\mathbf{q}_{i,j})$ overshoot the real solution by too much, the new guess could be outside the radius of convergence. To avoid that, the magnitude of the ratio of the correction to the current value is found in all zones. If the magnitude of the largest ratio is greater than some predefined maximum, all the corrections are scaled down by the same amount in order that the magnitude of the largest ratio is equal to the predefined maximum. The scaled corrections are then added to the current guess. The entire process is repeated until the corrections drop below some tolerance factor.

2.1.2 ROTORC OPERATIONAL PARAMETERS

The models computed in this work were made with solid body rotation on the ZAMS and local conservation of angular momentum during evolution. No convective core overshooting was allowed, meaning that the convective region is determined only by the region in which the adiabatic temperature gradient is less than the radiative temperature gradient and the material is assumed to have convective motions only in this region and not overshoot the boundary. It is possible that solid body rotation and no overshooting are not realistic characteristics of stars. Schou et al. (1998) provide observational evidence for the Sun rotating differentially with rotation rate increasing outward, and Stoeckley (1968) and Smith (1971) supply observational evidence of other stars suggesting a rotation rate increasing towards the rotation axis. Numerical models of rotating stars suggesting that differential rotation can be sustained in the convective core are provided by Deupree (1998). Observational evidence of convective core overshooting from a comparison of observed clusters with models is provided by Maeder & Meynet (1989). Deupree (2000, 2001) provides numerical models suggesting convective core overshooting takes place in both rotating and non-rotating stellar models. Though there is a trend in opinion that differential rotation and convective core overshooting are present in real stars, the degree to which these effects operate and what circumstances affect them are not well understood. Since it is not well known how much overshooting actually takes place in models that has been left out of our model calculations. Preliminary work that used models including overshooting produced values for the cluster fraction, C_f, only differing by 0.05 to 0.1.

The effects of differential rotation on inclination curves were studied by Gillich (2007) for a 10 $M_\odot$ star with surface equatorial velocities of 120 and 240 km s^{-1}. The differential rotation distribution of the ROTORC models is chosen to be:

$$\Omega(\varpi) = \frac{\Omega_0}{1 + (\alpha\varpi)^\beta}, \tag{2.51}$$

where Ω is the local angular rotation rate, ϖ is the distance from the rotation axis, α is a constant, and β is a constant describing the severity and type of differential rotation. This rotation law is conservative. A value of $\beta = 0$ corresponds to solid body rotation, values of $\beta < 0$ correspond to a rotation profile with Ω increasing with increasing ϖ, and values of $\beta > 0$ correspond to a rotation profile with Ω decreasing with increasing ϖ. There is a physical limit set on the upper limit of β (decreasing Ω with increasing ϖ). Stability constraints require that the angular momentum per unit mass must increase outward, putting an upper limit on β of 2 (Tassoul, 1978). Gillich was interested in $\beta > 0$ because there is some evidence to suggest that early type stars have positive values of β. The effects of decreasing rotation profile on spectral lines have not been well studied.

In the study done by Gillich as β increases from 0, the inclination curve becomes longer and the slope tends to decrease from nearly parallel to the ZAMS to a shallower slope than the ZAMS for sufficiently large β. For example a 10 $M_\odot$ star rotating with an equatorial surface velocity of 120 km s^{-1} with $\beta = 1$ has an inclination curve that is almost twice as long, and is inclined approximately 30° to the ZAMS. For $\beta = 2$ the inclination curve dips substantially below the ZAMS. Though the effects of differential rotation could have major implications for the results presented in this thesis, the amount of differential rotation in real stars has not been well quantified, making it difficult to choose realistic values of β. Choosing to model stars with a solid body rotation profile and no overshooting provides a suitable starting point for this investigation and allows results to be compared to other common calculations with no differential rotation or overshooting.

All stellar evolution models considered in this work have 10 angular zones. The evolutionary tracks with masses 3 – 12 $M_\odot$ at all rotations and 15 $M_\odot$ at rotations 0, 100, 405, and 455 km s^{-1} are computed with 350 radial zones. The evolutionary tracks at 15 $M_\odot$ at rotations 260 and 570 km s^{-1} where computed with 585 radial zones. The reason for the difference in zoning is that partial 15 $M_\odot$ evolutionary tracks were available from work by Tanner (private communication) at those rotation rates. Models at other rotation rates were scaled up from a lower mass with fewer radial zones than those started by Joel Tanner. The difference in zoning has little effect in the properties of evolutionary tracks, including the effective temperature and luminosity.

The errors arising from the different zoning are estimated by interpolating an evolutionary track at a ZAMS surface equatorial velocity of 260 km s^{-1} using evolutionary tracks at ZAMS surface equatorial velocities of 210 km s^{-1} and 405 km s^{-1}. Section 2.3.2 describes the interpolation procedure used to create the evolutionary track. Both the 210 km s^{-1} and the 405 km s^{-1} tracks have 350 radial zones. The turning point at the end of core hydrogen burning, the point labeled ② in figure 2.6, of the interpolated evolutionary track is then compared to the turning point of the computed 260 km s^{-1} evolutionary track having 570 radial zones. The estimated difference in $\log(L/L_\odot)$ and $\log(T_{\rm eff})$ from this different zoning is 3% (corresponding to a difference of 1100 $L_\odot$ at a luminosity of 40,000 $L_\odot$) and 0.4%

(corresponding to a difference of 100 K at a temperature of 24,000 K) respectively.

Other physical parameters used by ROTORC in computing the models for this work are the OPAL 1996 opacities (Iglesias & Rogers, 1996), the equation of state from tables produced by Rogers, Swenson, & Iglesias (1996), and the composite hydrogen burning nuclear reaction rates given in Fowler, Caughlan, & Zimmerman (1967). The ROTORC models used in the present work have a fractional heavy element abundance of $Z = 0.02$.

2.2 INCLINATION CURVES

Inclination curves determine the position on the HR diagram of a rotating star as a function of the star's inclination. An inclination curve is specified by producing the effective temperature, T_{eff} and luminosity, L, as functions of inclination. In this work analytic functions replace the inclination curves computed using the results of the PHOENIX (Hauschildt & Baron, 1999) stellar atmosphere code and the stellar structure code ROTORC, discussed previously. The analytic functions are developed by fitting the inclination curves calculated by Gillich (2007). They are used because calculating the actual inclination curves is too computationally time consuming for the number of models needed for this work. The next section, 2.2.1, briefly discusses the procedure used by Gillich to compute inclination curves. The following section, 2.2.2 describes the development and implementation of the analytic inclination curves.

2.2.1 COMPUTED INCLINATION CURVES

Inclination curves are produced by integrating weighted intensities over the visible surface of the star to produce the observed spectral energy distribution (SED), from which the luminosity and effective temperature can be deduced. This is performed with a code written by Lovekin (2005) and Lovekin, Deupree, & Short (2006). The integration is done by dividing the stellar surface into a mesh of 200 θ zones and 400 ϕ zones, where θ and ϕ are colatitude and azimuth angle respectively. For each mesh zone, an effective temperature, T_{eff}, and an effective surface gravity, $\log g_{\text{eff}}$, are determined from ROTORC models through linear interpolation. An interpolation through a grid of plane parallel model atmospheres is then used to specify the intensities in the direction of the observer at each of these $T_{\text{eff}}(\theta)$s and $\log g_{\text{eff}}(\theta)$s in the mesh zones.

The model atmospheres are computed by the stellar atmosphere code PHOENIX (Hauschildt & Baron, 1999). PHOENIX solves the equation of radiative transfer,

$$\frac{dI_\nu}{d\tau_\nu} = I_\nu - \frac{j_\nu}{\kappa_\nu}, \tag{2.52}$$

for the source function, $S(\nu) = \frac{j_\nu}{\kappa_\nu}$. Here j_ν and κ_ν are the emission and absorption coefficients respectively, and τ_ν is the optical depth. To solve for the source function, the occupation of thousands of atomic energy levels by electrons must be determined for the atomic elements included. These populations can be calculated in two main ways: using local thermodynamic equilibrium (LTE), or using non-LTE (NLTE). In LTE, matter and radiation are always assumed to be in equilibrium with each other locally. Thus, the radiation is described by the Planck function, $B(\lambda, T)$, and energy levels of the atoms are populated according to Maxwell-Boltzmann statistics. In NLTE, the determination of the source function is greatly complicated because no assumptions about how matter and radiation interact are made. In NLTE, level populations are calculated by actually solving coupled rate equations. These equations track the transition probabilities of populating or depopulating a given energy level, n, from all energy levels where a transition to or from n is possible. If all important atomic species are treated in this manner, the level populations can be calculated from a given radiation field. NLTE is a more realistic method for calculating model atmospheres, and is the method used to calculate model atmospheres by Gillich (2007), from which come the inclination curves used in the present work.

From the grid of model atmospheres, the intensity, $I_\lambda(\xi)$, for a wavelength, λ, and at an angle between the surface normal and the observer's line of sight, ξ, can be logarithmically interpolated using $\log(T_{\text{eff}})$ and $\log g_{\text{eff}}$ at each mesh zone. ξ depends on θ, ϕ, and i, the colatitude, azimuth, and inclination of the rotation axis to the line of sight of the observer, respectively. The projection of the surface area of a given mesh zone in the direction of an observer is also needed to calculate the observed fluxes. It is given by:

$$dA_{proj} = R^2(\theta)\sin\theta\cos\xi\sqrt{1+\left(\frac{dR}{Rd\theta}\right)^2}\,d\theta d\phi. \qquad (2.53)$$

It is the area of a spherical surface element with a local radius R, multiplied by a correction factor to account for the distortion of the surface from a sphere. From dA_{proj} and $I_\lambda(\xi)$, the observed flux can be calculated by performing the following integral over the surface of the mesh:

$$F_\lambda(i) = \int_\theta\int_\phi I_\lambda(\xi(\theta,\phi,i))\frac{dA_{proj}\cos\xi(\theta,\phi,i)}{d^2}, \qquad (2.54)$$

where d is the distance to the star from the observer. It is done for each wavelength at various selected inclinations.

From such fluxes the effective temperature and luminosity as functions of inclination can be obtained. The luminosity can be determined from the simple relation:

$$L(i) = 4\pi d^2 F(i), \tag{2.55}$$

where d is the distance of the star from the observer, and $F(i)$ is the total flux integrated over all wavelengths for a given inclination. $L(i)$ is seen to be independent of distance to the star, as it should be, by noting the form of F in equation (2.54). In practice the flux is integrated from $300 - 10,000$Å and then a Rayleigh-Jeans tail is used to evaluate the flux analytically from $10,000 - \infty$ Å. The cutoff of $10,000$ Åwas chosen to include the most important lines and to produce a smooth continuation from the model atmosphere fluxes to the analytic Rayleigh-Jeans expression for the fluxes.

To compute the observed effective temperature as a function of inclination, $T_{\text{eff}}(i)$, Gillich (2007) adopts a procedure utilized by observational astronomers. Color indices are used to calculate effective temperatures from the shape of the spectral energy distributions. Color indices are differences in magnitude of a star through two different color filters. In terms of fluxes, color indices become a ratio of fluxes because the magnitude of a star is proportional to the log of the flux. For spherical stars, a given temperature and effective surface gravity correspond to a unique color index for any two appropriately selected spectral energy bands. For a spherical star the surface gravity is constant. For a rotating star the observed spectral energy distribution is composed of the sum of different spectral energy distributions, all with differing effective surface gravities and effective temperatures. Once the spectral energy distribution for a rotating star is computed, T_{eff} and $\log g_{\text{eff}}$ must be determined simultaneously. The following method will uncover values T_{eff} and $\log g_{\text{eff}}$ that an observer would deduce from the star's SED. Since there are two unknowns, T_{eff} and

$\log g_{\rm eff}$, two color indices must be used to determine them uniquely. Colors are measured from SEDs by integrating the flux over a wavelength band.

The above process is described with no mention of the inclination of the star's rotation axis to the line of sight of the observer, and can be performed on an SED at any inclination. SEDs at differing inclinations will determine $T_{\rm eff}(i)$ and $L(i)$ at discrete values of i. Gillich (2007) computed inclination curves for 12 $M_\odot$ uniformly-rotating ZAMS models. More details can be found in his work. The uncertainties in the luminosities and temperatures of the inclination curves computed by Gillich come from three main sources: the uncertainty arising from difficulties converging the non-LTE atmospheres (0-4%), the integration code which integrates over the surface of the model and interpolates in atmospheric models (1-4%), and the uncertainties in deriving luminosity and temperature from the computed spectra (1-6% for luminosity and 0.1-0.6% for temperature).

2.2.2 ANALYTIC INCLINATION CURVES

As discussed in the previous section, the method for determining the effective temperature, $T_{\rm eff}(i)$, and the luminosity, $L(i)$, as functions of inclination (inclination curves) is obtained by integrating the weighted intensity over the observed surface of a star. Such integration is very computer intensive because of the large number of wavelengths, and takes approximately 15 hours to complete for one stellar model using 10 cores from a 92 core Beowolf cluster of 2.6 GHz, dual-core, Opteron processors. Each dual-core has 2GB of RAM. The 15 hours to compute the inclination curve does not include the time to compute the grid of necessary stellar atmospheres covering the $T_{\rm eff}$ and $\log g_{\rm eff}$ space in which the star's local surface properties reside. For the 12 $M_\odot$ rotating models computed by Gillich (2007), the ranges of $T_{\rm eff}$ and $\log g_{\rm eff}$ on the surface of the star are covered by a grid consisting of 60 model atmospheres. Each model atmosphere takes on the order of 40-60 hours to complete, using 6 processors from a 48 processor cluster of 2.4 and 2.8 GHz Xeon processors for the first 20-30 hours of the calculation, and then using only 1 processor for the remaining time, as part of the computation can only be completed in serial. If only the time to compute the inclination curve is considered (i.e. excluding the time to compute the grid of model atmospheres) to make computations for enough stars (300 stars) in enough clusters (300 clusters) to obtain statistically useful results, at least 150 years would be required. Therefore, analytic functions have been developed to translate the ROTORC-computed effective temperature, $T_{\rm eff}(\theta)$, and luminosity, $L(\theta)$, to the inclination curves.

Let $L(\theta)$ be the luminosity of a spherical star, with radius $R(\theta)$ and effective temperature $T_{\rm eff}(\theta)$. The luminosity is defined as:

$$L(\theta) = 4\pi R(\theta)^2 \sigma T_{\rm eff}(\theta)^4, \tag{2.56}$$

where σ is the Stefan-Boltzmann constant and $R(\theta)$ is the local radius as a function of colatitude.

The analytic inclination curves are described by relations for $T_{\rm eff}(i)$ and $L(i)$. The relations are found by fitting functions to the inclination curves calculated by Gillich (2007) for zero age main sequence (ZAMS) 12 $M_\odot$ models at 13 different rotations: 0, 50, 100, 150, 210, 255, 310, 350, 405, 450, 500, 550 and 575 km s^{-1}. As the star ages, its surface equatorial velocity will slow if there is local conservation of angular moment at the surface, as is assumed in the calculations. It is also assumed that the effect on observed $T_{\rm eff}(i)$ and $L(i)$ from evolution will be the same as that for a ZAMS model at a corresponding lower surface equatorial velocity. We shall discuss a test of this assumption shortly.

We define T_{av} and L_{av} as the average effective temperature and luminosity. These averages are used as a reference point from which to measure the deformation of the observed surface properties from rotation. The average effective temperature is defined as:

$$T_{\mathrm{av}} = \frac{1}{N_\theta} \sum_i^{N_\theta} T(\theta_i), \tag{2.57}$$

and likewise:

$$L_{\mathrm{av}} = \frac{1}{N_\theta} \sum_i^{N_\theta} L(\theta_i), \tag{2.58}$$

where the θ_i are the ROTORC colatitudes for each angular zone, and N_θ is the number of ROTORC angular zones.

The transformations from the colatitude dependent variables to the inclination depends on how much the ROTORC surface properties vary. The difference between the pole and equator of $T_{\mathrm{eff}}(\theta)$ and $L(\theta)$ can be used as a measure of this variation. Define the difference between pole and equator values of $T_{\mathrm{eff}}(\theta)$ and $L(\theta)$ as:

$$\Delta T = T_{\mathrm{eff}}(\theta = 4^\circ.5) - T_{\mathrm{eff}}(\theta = 85^\circ.5), \tag{2.59}$$

and likewise

$$\Delta L = L(\theta = 4^\circ.5) - L(\theta = 85^\circ.5), \tag{2.60}$$

respectively. Note that $\theta = 4^\circ.5$ and $\theta = 85^\circ.5$ correspond to the center of the ROTORC zones adjacent to the pole and equator respectively. To aid in making our transformations more independent of the specific models, the Δs are divided by the average quantities. The

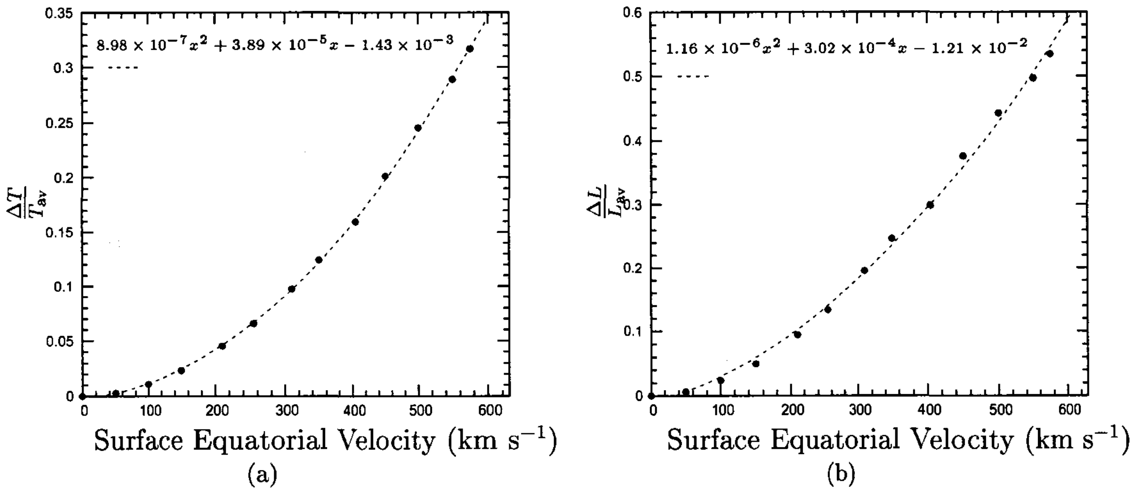

Figure 2.1: Rotation relation for (a) temperature and (b) luminosity for 12 $M_\odot$ models at various rotation rates.

amount of departure from a spherical uniform temperature distribution is clearly dependent on the amount of rotation. Therefore, the quantities $\frac{\Delta T}{T_{\mathrm{av}}}$ and $\frac{\Delta L}{L_{\mathrm{av}}}$ are indicators of how much $T_{\mathrm{eff}}(i)$ and $L(i)$ differ from T_{av}, and L_{av}, because they are related to the amount of rotation in the model. Figure 2.1 (a) shows the relation between $\frac{\Delta T}{T_{\mathrm{av}}}$ and the surface equatorial velocity. Likewise, figure 2.1 (b) shows the relation for $\frac{\Delta L}{L_{\mathrm{av}}}$. The relationship is essentially quadratic, which is expected since the angular velocity Ω turns up in the conservation equations as Ω^2. We also note that $V_{\mathrm{eq}} = \Omega R$, and if the radius, R, is constant, $V_{\mathrm{eq}} \propto \Omega$. R is nearly constant for slow and moderate rotation rates, but this is not true for faster rotation rates.

$\frac{\Delta T}{T_{\mathrm{av}}}$ and $\frac{\Delta L}{L_{\mathrm{av}}}$ are monotonically increasing functions with surface equatorial velocity, at least in the case for solid body rotation considered here. During core hydrogen burning for massive stars, the amount of differential rotation generated from evolution is small, and we assume our approach is adequate.

The range of equatorial surface velocities used in the fit (0-575 km s^{-1}) spans the range of equatorial surface velocities of the most massive stellar evolutionary track, 15 $M_\odot$, used by the synthetic cluster code. Models at lower masses have their equatorial surface velocities chosen such that they have the same surface shape, and thus have lower equatorial surface velocities than a more massive star with similar surface shape. More important than the surface equatorial velocity being within the range considered is whether the indicators for the degree of departure from $T_{\rm av}$ and $L_{\rm av}$ are with in the range used for the fit. The range for $\frac{\Delta T}{T_{\rm av}}$ over the equatorial surface velocities of the 12 $M_\odot$ models is (0.0, 0.317), and for $\frac{\Delta L}{L_{\rm av}}$ the range is (0.0, 0.535). Neither range is exceeded over the entire mass and surface equatorial velocity range of the grid of ROTORC stellar evolution tracks.

As done for the ROTORC surface properties, we non-dimensionalize the inclination dependent luminosity and effective temperature calculated by Gillich (2007). For example, we use $\frac{T_{\rm av}-T_{\rm eff}(i)}{T_{\rm av}}$. We complete the analytic fit by plotting $\frac{T_{\rm av}-T_{\rm eff}(i)}{T_{\rm av}}$ versus $\frac{\Delta T}{T_{\rm av}}$ for each inclination. The results are shown in figure 2.2 for four selected inclinations. Similar plots for the luminosity are shown in figure 2.3. It can easily be seen that $\frac{T_{\rm av}-T_{\rm eff}(i)}{T_{\rm av}}$ follows a cubic reasonably well, while $\frac{L_{\rm av}-L(i)}{L_{\rm av}}$ follows a quadratic. The cubic and quadratic fits in the plots are shown with a dashed line, and have coefficients provided in tables 2.1 and 2.2 for temperature and luminosity, respectively, at the corresponding inclinations. A total of ten fits were done, corresponding to the ten inclinations at which the computed inclination curves are defined. This results in 10 sets of coefficients for both temperature and luminosity at inclinations of 0°, 10°, 20°, ... 90°.

If the trends shown in figure 2.2 and figure 2.3 hold across mass and age, the effective temperature and luminosity as functions of inclination can be found by solving $\frac{T_{\rm av}-T_{\rm eff}(i)}{T_{\rm av}}$ and $\frac{L_{\rm av}-L(i)}{L_{\rm av}}$ for $T_{\rm eff}(i)$ and $L(i)$. That gives $T_{\rm eff}$ and L at discrete inclinations corresponding to

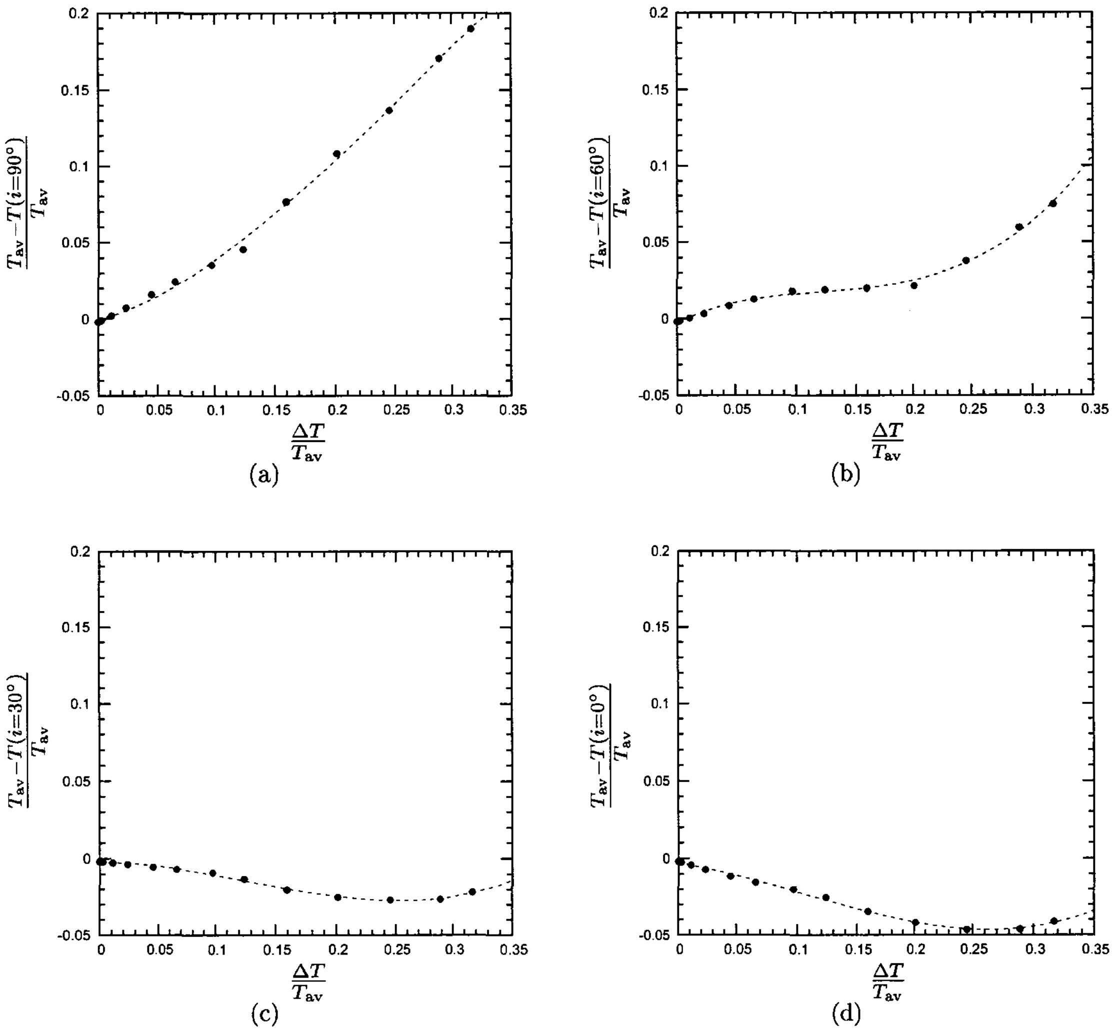

Figure 2.2: The departure of $T(i)$ from $T_{\rm av}$ at differing, $\frac{\Delta T}{T_{\rm av}}$. (a), (b), (c) and (d) are at inclinations of 90°, 60°, 30° and 0° respectively. The intermittent inclinations, 10°, 20°, 40°, etc. are not shown, but show similar trends. The dashed lines are the fits described by the temperature coefficients given in table 2.1.

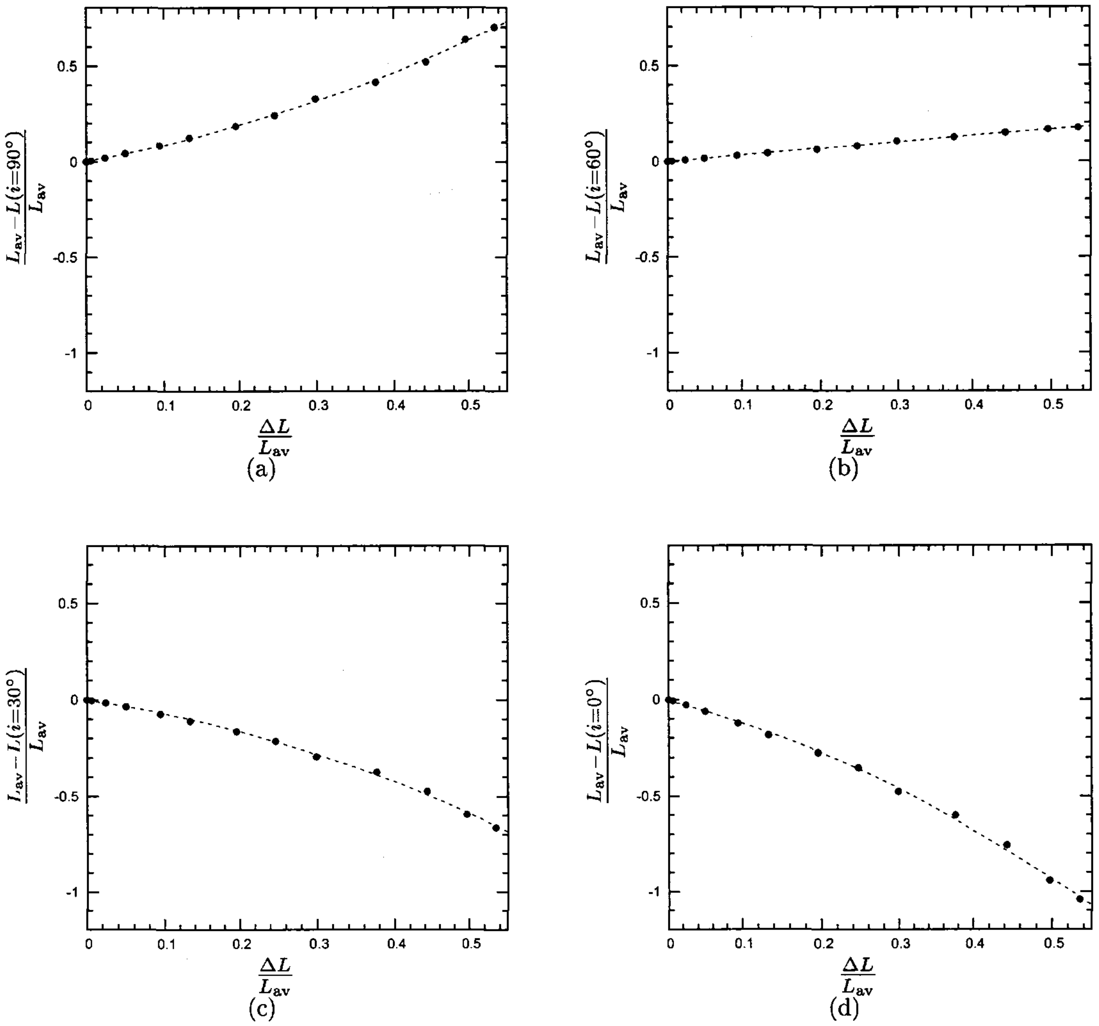

Figure 2.3: The departure of $L(i)$ from $L_{\rm av}$ at differing, $\frac{\Delta L}{L_{\rm av}}$. (a), (b), (c) and (d) are at inclinations of 90°, 60°, 30° and 0° respectively. The intermittent inclinations, 10°, 20°, 40°, etc. are not shown, but show similar trends. The dashed lines are the fits described by the luminosity coefficients given in table 2.2.

i	A_i	B_i	$C_i(\times 10^1)$	$D_i(\times 10^3)$
0	2.94248287	-0.92347285	-1.26452264	-2.80255079
10	3.12245783	-1.00418961	-1.11505019	-2.76241808
20	3.31228923	-1.17267050	-0.56545552	-2.78688538
30	3.10929192	-1.20200219	0.06983017	-2.56526421
40	2.99650915	-1.28245733	0.94656344	-2.37822413
50	4.09471937	-1.83267857	2.38845949	-2.71371317
60	6.64960207	-2.49591152	3.72340463	-2.80450185
70	-0.28525034	0.67783626	1.85131072	-0.15163749
80	-4.08899070	2.42107583	1.38519203	0.35934546
90	-2.96911393	2.21933769	1.94703489	-0.16966418

Table 2.1: Temperature function coefficients

i	E_i	$F_i(\times 10^1)$	$G_i(\times 10^3)$
0	-1.70878235	-9.98920733	-7.46829403
10	-1.66322538	-9.40406315	-7.33754680
20	-1.49486706	-7.89817367	-6.53055571
30	-1.23077435	-5.55427584	-5.37411417
40	-0.89008923	-2.61670215	-4.17380908
50	-0.48802384	0.55424950	-3.09441280
60	-0.02815609	3.46493106	-1.88880111
70	0.46112084	5.65280279	-0.31326165
80	0.88227498	6.87326154	1.44306299
90	1.08186403	7.20450151	2.48222159

Table 2.2: Luminosity function coefficients

the coefficients in table 2.1 and table 2.2. Thus the effective temperatures and luminosities are given by:

$$T_{\mathrm{eff,i}} = T_{\mathrm{av}} \left[1 - \left(A_i \left(\frac{\Delta T}{T_{\mathrm{av}}} \right)^3 + B_i \left(\frac{\Delta T}{T_{\mathrm{av}}} \right)^2 + C_i \left(\frac{\Delta T}{T_{\mathrm{av}}} \right) + D_i \right) \right], \tag{2.61}$$

and

$$L_i = L_{\mathrm{av}} \left[1 - \left(E_i \left(\frac{\Delta L}{L_{\mathrm{av}}} \right)^2 + F_i \left(\frac{\Delta L}{L_{\mathrm{av}}} \right) + G_i \right) \right]. \tag{2.62}$$

The two functions now define inclination curves at inclinations 0°, 10°, 20°, ...90°. To obtain L and T_{eff} at inclinations between the discrete inclinations, linear interpolation is used.

The resulting inclination curves on the H-R diagram are shown in figure 2.4 for various rotational velocities. The analytic inclination curve has a maximum difference from the computed inclination curve over all inclinations and rotations of 0.0036 in $\log(T_{\mathrm{eff}})$ and 0.013 in $\log(L/L_{\odot})$. The overall curve shape is very well reproduced for high rotations. For lower surface equatorial velocities (below 255 km s^{-1}), the inclination curves' shapes are not as well reproduced, but the absolute departures for the curves still remain small. See figure 2.4 for an example of the poor shape reproduction for a surface equatorial velocity of 210 km s^{-1}. The small extent of the low velocity curves causes the poor reproduction of shape to be unimportant in this analysis.

To test the assumptions of portability for the analytic inclination curve, the analytic inclination curve was compared with two computed curves for a 15 $\mathrm{M}_{\odot}$ model with a ZAMS surface equatorial velocity of 570 km s^{-1} at two different stages of core hydrogen burning. The result is shown in figure 2.5. The two models correspond to phases of evolution where

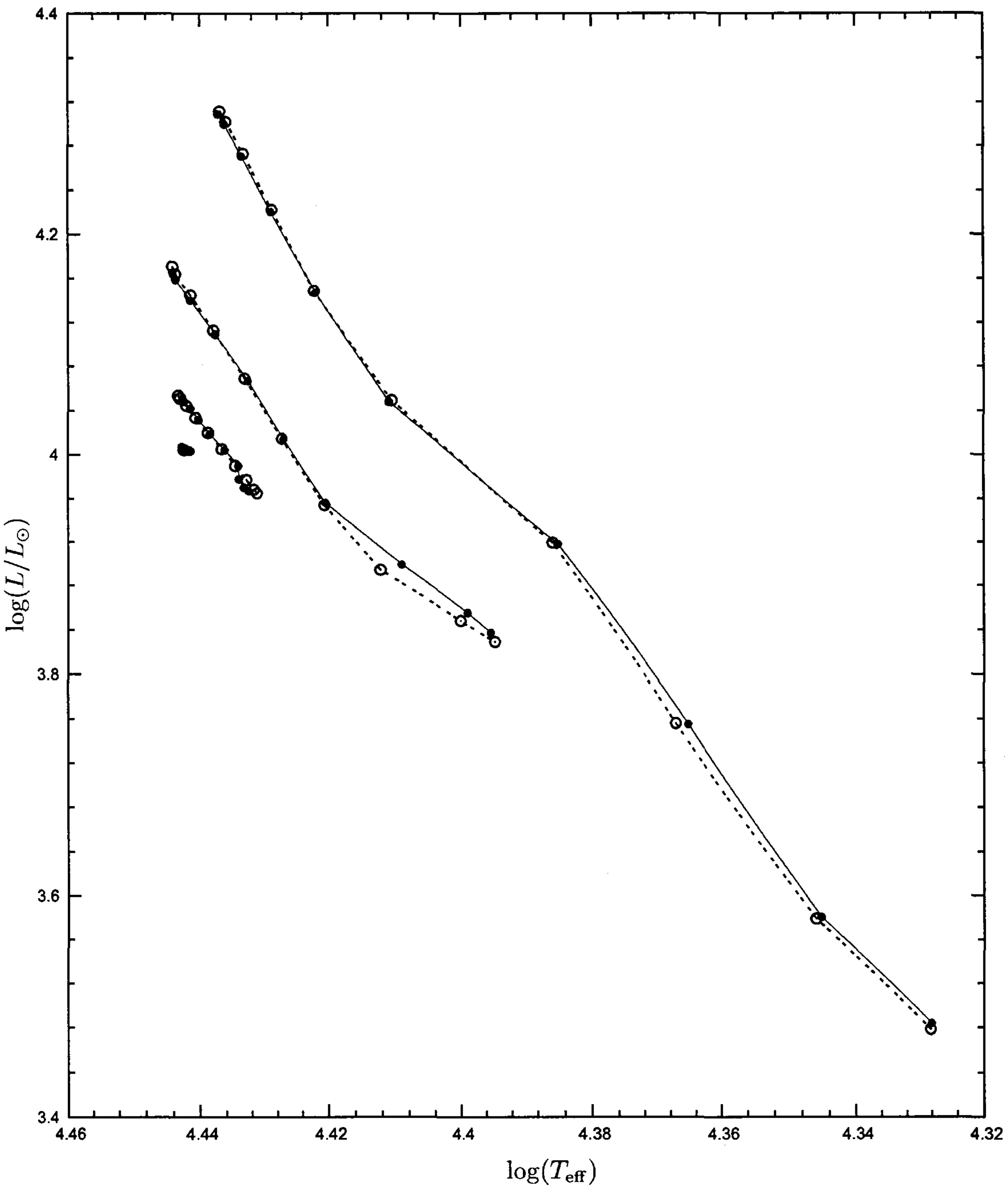

Figure 2.4: Inclination curves computed by Gillich (2007) (dashed curve with open circles) for a 12 $M_{\odot}$ star compared to the analytic fits (solid curve with solid dots). Each point on the curve is a different inclination starting at 0° in the upper left corner to 90° in the lower right corner in increments of 10°. Curves from top to bottom are at differing rotation speeds of 575 km s^{-1}, 405 km s^{-1}, 210 km s^{-1}, and 0 km s^{-1}.

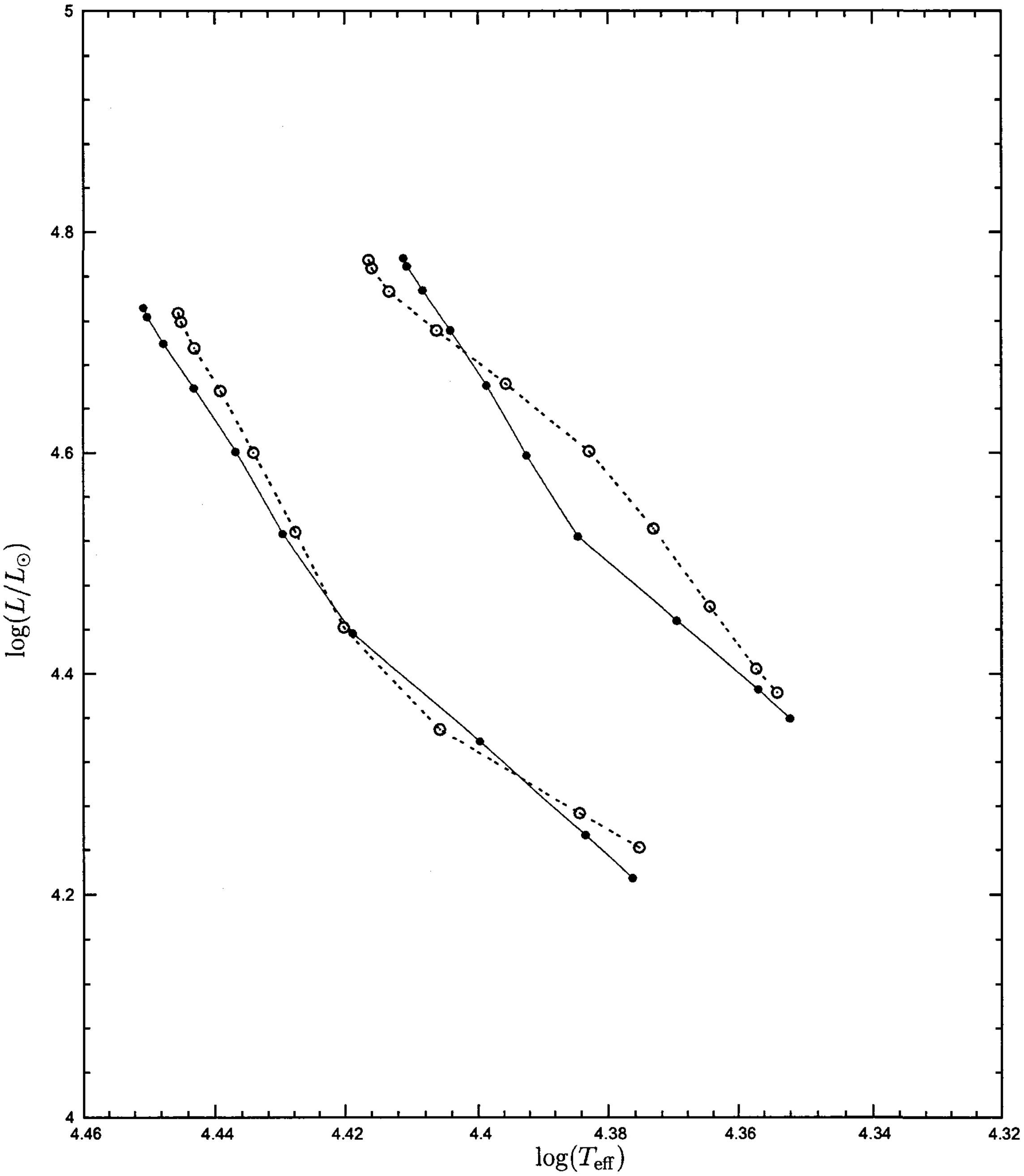

Figure 2.5: Inclination curves computed by Gillich (private communication) are shown as black dashed curves with open circles. Analytic inclination curves are shown as solid curves with filled circles. The inclination curves are computed for two models in the evolutionary sequence of a 15 $M_\odot$ star with a ZAMS surface equatorial velocity of 570 km s^{-1}. The lower left curve is for a model with a central hydrogen mass fraction of 0.305 the upper right curve is for a model with a central hydrogen mass fraction of 0.115.

the central hydrogen mass fraction is 0.305 and 0.115. The position of the two curves relative to each other results primarily from evolution. It can also be seen that the length of the more evolved inclination curve is shorter. That results from a slowing down of the surface equatorial velocity as the star ages. The analytic curve mimics the shortening well. It is also noted that the overall shape of the curve changed somewhat as the star aged, which is not well reproduced by the analytic curve. The maximum difference in effective temperature is found in the older curve and is 600 K, at a temperature of 24,000 K it amounts to about 2.6%. The maximum difference in the luminosity is also found in the older curve, and is 1,000 $L_{\odot}$. At a luminosity of 24,000 $L_{\odot}$ this amounts to about 5.5%. If one compares the errors to the uncertainties in the computed inclination curve found by Gillich, of at least 1-6% in luminosity and 0.1-0.6% for temperature, the lack of agreement for the luminosity does not appear serious. While not within the uncertainty estimates of Gillich (2007), the differences between temperatures are not large when compared to the changes in luminosity and temperature over the length of the inclination curve. The discrepancy in temperature will not greatly affect the results. The luminosity agrees with the computed curves to within the maximum uncertainty. From figure 2.5 it can be noted that the end points and length of the inclination curves are reasonably well represented. The curve shape, which is not as well represented as desired, is less important to the current work. That is because the present work looks at selected cluster stars which are at outer edges of the cluster in the HR diagram, and the end points of the inclination curves dictate the location of the stars in these areas.

2.3 SYNTHETIC CLUSTER GENERATION

We must generate stellar evolutionary tracks to create synthetic clusters. The tracks were made for a grid in mass (3, 5, 8, 12, and 15 $M_\odot$) and rotation. An upper limit of 15 $M_\odot$ was decided on in order to avoid problems arising from mass loss in massive stars. Generally studies considering mass loss focus on stars with masses $\geq$20 $M_\odot$, see Chiosi & Maeder (1986) for examples. At each of the five masses indicated there are six different rotation rates, giving a total of 30 evolutionary tracks. The rotation rates at each of the five masses are chosen to maintain the same approximate surface shape across all masses. The surface shape depends on ω/ω_c, which is believed to be the best variable to measure rotation. The ratio of the polar radius to the equatorial radius, $R_{\rm pole}/R_{\rm eq}$, is monotonically related to ω/ω_c and is used as an indicator of the surface shape. This method for identifying models with similar surface properties was adopted from the original synthetic cluster code provided by Deupree (private communication). It is desirable for the models to have similar surface shapes so that surface properties will vary between tracks only as a function of mass within a given surface shape. To maintain surface shape as the mass increases, the surface equatorial velocity must also increase. Table 2.3 lists the grid of masses and surface equatorial velocities of each of the tracks, and also includes the ratio of the polar to equatorial radius, the fractional polar radius ($R_{\rm pole}/R_{\rm eq}$). The fractional polar radius is unknown before the model is computed. Determining a surface equatorial velocity for a given mass that will reproduce a particular fractional polar radius involves a degree of trial and error. Some of the models have been selected from previously computed ZAMS models that have approximately the same fractional polar radius as those at other masses. Other models have been computed specifically to produce the desired fractional polar radius.

The next section describes what properties must be defined in order to determine a cluster member's position in the HR diagram along with how the properties are determined. The section "Evolutionary Track Interpolation" describes how the properties of a cluster member are used to determine its HR diagram position.

Rot.	15 M$_\odot$		12 M$_\odot$		8 M$_\odot$		5 M$_\odot$		3M$_\odot$	
Index	$V_{\rm eq}$	$R_{\rm pole}/R_{\rm eq}$	$V_{\rm eq}$	$R_{\rm pole}/R_{\rm eq}$	$V_{\rm eq}$	$R_{\rm pole}/R_{\rm eq}$	$V_{\rm eq}$	$R_{\rm pole}/R_{\rm eq}$	$V_{\rm eq}$	$R_{\rm pole}/R_{\rm eq}$
1	0	1.00000	0	1.00000	0	1.00000	0	1.00000	0	1.00000
2	100	0.99125	100	0.99014	90	0.99103	80	0.99103	70	0.99182
3	260	0.94077	240	0.94492	210	0.94905	205	0.94077	185	0.94077
4	405	0.85966	375	0.86640	330	0.87880	300	0.87467	275	0.87055
5	455	0.82319	435	0.82095	405	0.81683	375	0.80858	345	0.79618
6	570	0.72593	540	0.72593	495	0.72593	450	0.72181	410	0.71353

Table 2.3: The grid of evolution tracks used by the synthetic cluster code. $V_{\rm eq}$ is the surface equatorial velocity at the ZAMS in km s^{-1}. $R_{\rm pole}/R_{\rm eq}$ is the fractional radius of the pole with respect to the equator radius. Rot. index is the rotation index assigned to each surface shape. See section 2.3.1 for details about the rotation index.

2.3.1 DETERMINING PROPERTIES OF CLUSTER MEMBERS

The free parameters related to the stellar evolutionary curves are the mass, rotation rate, and age. How those properties are determined for each cluster member is discussed here. The inclination is also important for determining the observed effective temperature and luminosity, as it allows the position along the analytical inclination curve to be determined.

The amount of rotation is described by a floating point index between 1 and 6 and is referred to as the rotation index. It corresponds to the six values of rotation for each mass in table 2.3. A rotation index of 1 corresponds to an surface equatorial velocity of zero and a rotation index of 6 to the maximum surface equatorial velocity, as given in table 2.3. For example, a 12 M$_\odot$ star with a rotation index of 3 has a ZAMS surface equatorial velocity of 240 km s^{-1}. A constant rotation index represents constant surface shape on the ZAMS for any mass because of the manner in which the ZAMS equatorial surface velocities are chosen.

The fractional part of the rotation index corresponds to equatorial surface velocities between the grid velocities. To determine the surface equatorial velocity from the rotation index, we must interpolate among the surface equatorial velocities of the surrounding computed models.

The rotation index is chosen in the range (1-6) by using the random number generation function, `RAND`, in FORTRAN which returns a number between 0 and 1 with equal probability of the number being anywhere in that range. The result from the `RAND` function is then scaled and shifted to cover the range of the rotation index using:

$$\text{rotation index} = 5(\texttt{RAND})^p + 1. \tag{2.63}$$

Raising `RAND` to the power of p allows for different rotation distribution functions for stars within a cluster to be tested. A value of p greater than 1 produces a distribution favoring slower rotators whereas a value of p less than 1 produces a distribution favoring faster rotators. The impact of the rotation distribution on the results of this thesis is discussed in section 3.2.

Environmental effects can play a role on the distribution of rotation among cluster members. However, such a relationship is complex and the details are not well understood. There may also be many subtleties which make the prescription of a generally applicable rotation distribution difficult. However, some trends have been found; for example, a sample of stars from dense clusters typically has more rapid rotating stars when compared to a sample of field stars (Wolff et al., 2007). One theory for this is mergers of binary systems, as mentioned by Turner (1996a), which would spin up the merged star by conservation of angular momentum. Regardless, the above prescription allows us to consider differing smooth distributions of rotation among clusters in a simplistic way and allows us to obtain relevant information while avoiding many of the complexities and unknowns, for example the $v \sin i$ dependence, of a more detailed observed distribution.

The star's mass is chosen in a slightly more complicated way. The Salpeter (1955) initial mass function (IMF) is used. To establich the masses of stars in the cluster, the range that a single star can occupy in mass is determined. That range is determined based on the Salpeter power law, keeping the number of stars in the cluster fixed at N. The Salpeter IMF gives the number of stars, $n(m)$, as a function of mass, m, as:

$$n(m) = Cm^P, \tag{2.64}$$

where m is units of $M_\odot$, C is a constant, and $P = -1.35$. The power, P, was left as a variable in the interpolation code, so that it could be changed later if desired. The number of stars, N, in a given mass range, M_{min} to M_{max}, is given by:

$$N = C \int_{M_{min}}^{M_{max}} m^P dm = \frac{C}{P+1} \left(M_{max}^{P+1} - M_{min}^{P+1} \right). \tag{2.65}$$

Given the number of stars in the cluster and the mass range of the cluster (M_{max}, M_{min}), the normalization constant C can be found as:

$$C = \frac{N(P+1)}{M_{max}^{P+1} - M_{min}^{P+1}}, \tag{2.66}$$

so that the integration over the mass range will produce N stars. If N in equation (2.66) is set to 1, the mass bounds that this single star can be between can be solved for. Let the upper and lower masses of a single star be defined as M_i and M_{i+1}. Solving equation (2.66) for M_{i+1} with $N = 1$ produces:

$$M_{i+1} = \left(\frac{P+1}{C} + M_i^{P+1}\right)^{\frac{1}{P+1}} . \tag{2.67}$$

Given $M_i = M_{min}$, the above recursion relation allows each successive mass range to be determined until $M_{i+1} = M_{max}$. It produces N mass ranges in which the N stars are to be placed. To pick a mass for the i^{th} star, the **RAND** function is used to choose a random mass in the range M_i to M_{i+1}. The same approach was used by Harris & Deupree (1976).

The age of the cluster must still be chosen. This is an input that the user specifies, and is assumed to be the same for all cluster members. The synthetic cluster code does have some functionality built in to allow the age to be randomly chosen within a specific range in a similar manner to the inclination or rotation. The formation time, as well as the age of the cluster, is limited by the largest mass evolutionary track. Though that functionality may be used to explore the effects of a finite cluster formation time, the option is not utilized in this research. Instead, it is primarily used as a means of computing interpolated quantities over a range of ages for comparison, for example an interpolated evolution track that may be compared with a ROTORC evolutionary track.

Finally, the inclination of the star's rotation axis to the line of sight is chosen randomly between 0° and 90°. Again, the **RAND** function is used and scaled up to the desired range. This assumption is valid because a star's rotation axis must be random with respect to an arbitrary observer. However, it is possible that members within a cluster may have some preferred rotation axis orientation since they likely formed out of the same cloud of gas with some net angular momentum. Of course, effects such as a gravitational interaction with other formed or forming stars in the cluster could affect the orientation of the rotation axis in a random way.

2.3.2 EVOLUTIONARY TRACK INTERPOLATION

Evolutionary track interpolation takes the model information from the ROTORC evolution tracks and interpolates it to the required mass, rotation, and age. The following ROTORC quantities must be interpolated: $T_{\mathrm{eff}}(\theta)$, $R(\theta)/R_{\mathrm{eq}}$, and R_{eq}, the equatorial radius. These interpolated quantities, plus the inclination, permit the determination of the model's apparent location in the HR diagram. Other quantities that are also interpolated but not required to determine the observed luminosity and effective temperature are: ROTORC total luminosity, ROTORC average effective temperature, and surface equatorial velocity. These additional quantities are useful for testing and understanding the results of the interpolation.

Before the interpolation can be done, eight models are found that bracket the desired mass, rotation, and age. To describe the interpolation process and how the bracketing models are found, the interpolation of a 6.85 $\mathrm{M}_{\odot}$ model at an age of 0.028 byr at a rotation index of 3.89 is followed step by step.

Four bracketing evolutionary tracks are found, first by identifying masses which bracket the desired mass (in this case 8 and 5 $\mathrm{M}_{\odot}$). Then the rotation indices for each of these masses which bracket the desired rotation index (in this case 3 and 4) are identified. This now defines four evolutionary tracks which bracket the desired model's mass and rotation rate. The next step is to find which two models, on each of these four tracks, bracket the desired age. This is not as straightforward as it might appear.

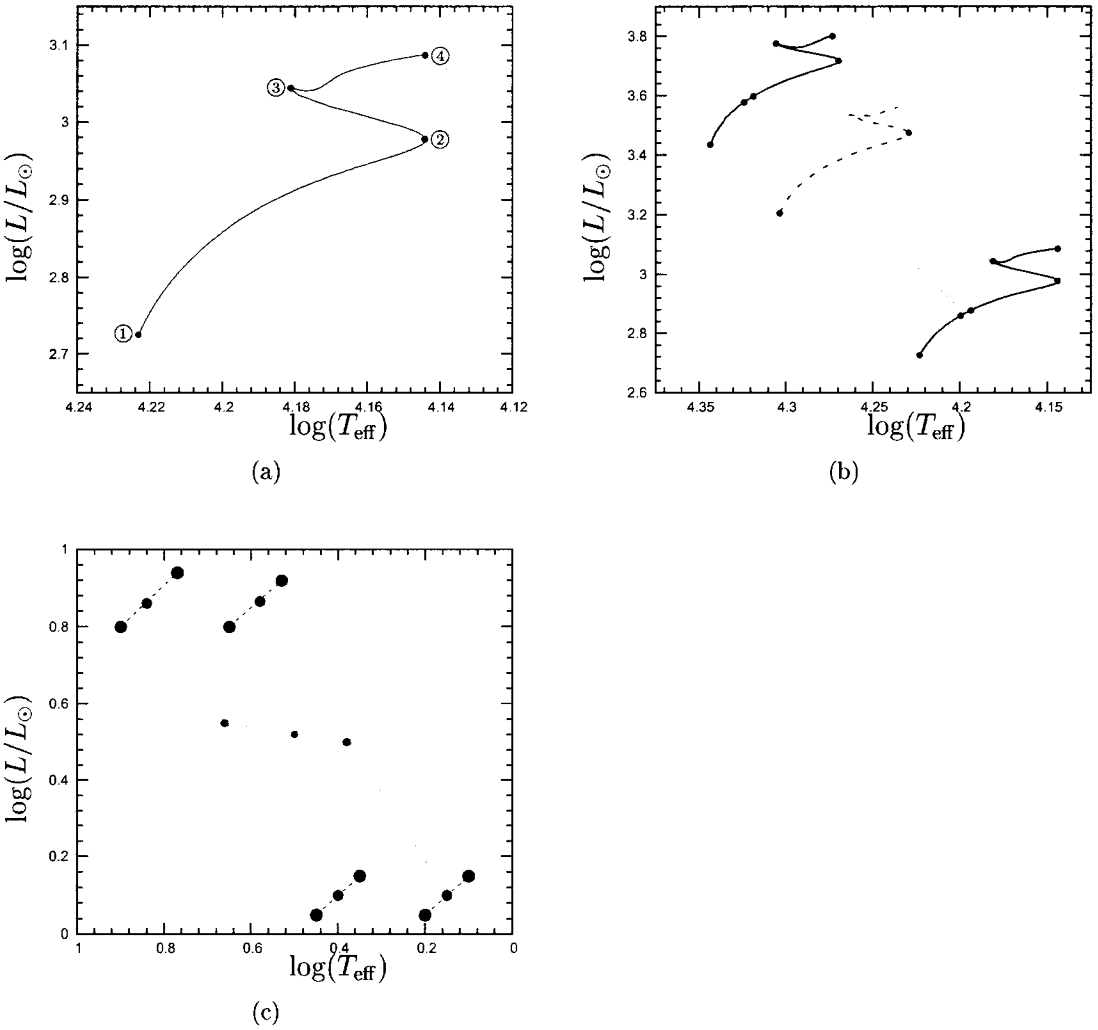

Figure 2.6: (a) Turning points of a 5 M$_\odot$ star with a rotation rate of 205 km s^{-1}. At ① the model is on the ZAMS, at ② the model is at the second turning point, at ③ the model is at the third turning point, and ④ is the last model in the evolution sequence. (b) Solid black lines are evolutionary tracks of 5 M$_\odot$ and 8 M$_\odot$ stars with the larger mass being hotter and more luminous. The dashed black line shows an interpolated evolution track at 6.85 M$_\odot$. The blue dots indicate turning points and the dashed blue lines connect common turning points across mass. The red dots indicate models in the tracks which are in a similar phase of evolution as the desired model (0.028 byr). The red dashed line indicates the same phase of evolution across mass as the desired model. (c) Red dots indicate the 8 bracketing models from the evolution tracks. The blue dots indicate the interpolation in age, the green dots represent the interpolation in mass, and the black dot the interpolation in rotation. The scale of figure (c) is arbitrary as the real scale is difficult to clearly depict the mechanics of the interpolation.

To produce a model at a mass between the calculated masses, models must be interpolated within similar phases of evolution. Finding models in similar phases of evolution at different masses is not simply a matter of searching the evolutionary tracks and selecting the ages that bracket the desired age. Since more massive stars evolve faster than lower mass stars, interpolation must be between similar phases of evolution, not ages (Meyer-Hofmeister, 1969; Schlesinger, 1969). To find similar phases of evolution, turning points in the HR diagram are used. Figure 2.6 (a) shows the turning points with red dots. The numbers identify a particular turning point.

Turning point ① corresponds to the zero age main sequence (ZAMS), where the star has just begun hydrogen burning in the core. From ① to ② the star is burning hydrogen in the core. When hydrogen begins to become depleted in the core (hydrogen mass fraction of ~ 0.01), hydrogen burning slows to the point that the star as a whole begins to contract. The curve between points ② and ③ in figure 2.6 (a) corresponds to the overall contraction phase. At point ③ the star begins hydrogen burning in a shell around the core. Point ④ in figure 2.6 corresponds to the end of the calculated evolutionary sequence.

Because the cluster members all share the same age, only for the most massive evolutionary tracks will the synthetic cluster code interpolate in this last calculated phase of evolution (③-④). The time the star spends on ③-④ branch of evolution is far less than the time spent in core hydrogen burning. Very few observed clusters will have any stars in this region of the cluster's HR diagram, since the stars will rapidly cool as they expand, moving first to cooler effective temperatures at nearly the same L and then moving up the super giant branch to begin helium burning. We note that we cannot include stars in the cluster synthesis much beyond the gravitational contraction phase because of the upper mass limit of the models. In practice, that restricts the ages we can impose on the cluster.

To determine which phase of evolution our desired model is in, the age of the turning points must be determined at the desired model's mass. That is done by linear interpolation in log age from the turning points of each bracketing mass to the desired mass using the log of mass. In figure 2.6 (b) the turning points are shown as blue dots. The evolutionary tracks of the grid are solid black lines. The dashed black line represents the interpolated evolutionary track of the desired mass. Note that evolutionary tracks are not actually computed during the interpolation process. All evolutionary tracks in figure 2.6 (b) are at the same rotation index of 3. The blue dots on the dashed black line are the interpolated turning points. The ages of the turning points are tested to find which two turning points our desired model is between. For the model parameters given above, that corresponds to the turning points labeled ① and ②. The age at the two bracketing masses corresponding to the same phase of evolution as the desired mass can be found by using the age fraction, which is the age fraction of the desired model between the two interpolated turning points. These interpolated turning points are shown as the blue dots on the black dashed curve in figure 2.6 (b). Then two adjacent models are found on each evolutionary track that span an age determined at each track using the age fraction. These models are shown in figure 2.6 (b) as red dots. The separation of these age-bracketing models has been exaggerated so that the two models can be visually differentiated from each other. This process is then repeated at the other rotation index of 4, resulting in a total of eight models. Figure 2.6 (c) shows these eight models as red dots among which the interpolations are performed.

Once all the bracketing models have been found, a desired quantity, q, is interpolated to the desired age, mass, and rotation from the eight bracketing models. The models form

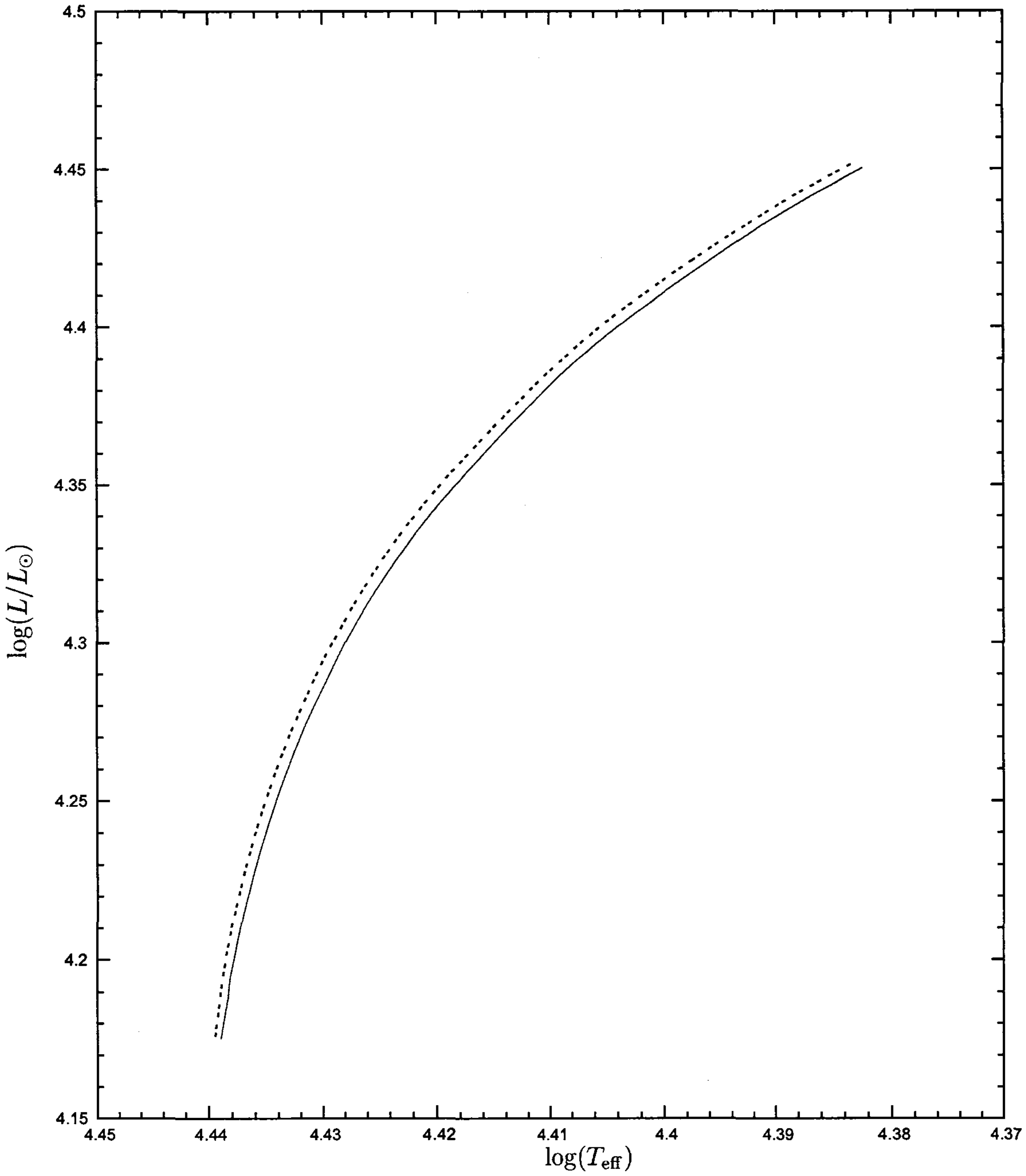

Figure 2.7: Two evolutionary tracks of a 14 $M_\odot$ model with a ZAMS surface equatorial velocity of 498 km s^{-1}. The dashed line is the evolutionary track computed using ROTORC, while the solid line is the track interpolated from the ROTORC grid of models.

a hexahedron in age, mass, and rotation space. First q is interpolated in age between the two models on each evolution track. That is done by linearly interpolating in log age. The result of one interpolation corresponds to one of the blue dots in figure 2.6 (c), and is repeated for the other 4 evolutionary tracks. There are now 4 q's interpolated from the original 8 ROTORC models to the correct age at the differing masses and rotations of the 4 bracketing ROTORC evolutionary tracks. At each of the rotations the two q values are then interpolated linearly in log mass, and results in the two green points in figure 2.6 (c). Finally, q is linearly interpolated in rotation index, producing the value of q at the desired mass, age, and rotation index. To obtain the actual surface equatorial velocity instead of a rotation index the surface equatorial velocity is interpolated from bracketing models just as any other quantity would be. The fractions between bracketing age, mass, and rotation index are calculated once for each interpolated model, and are reused for each quantity, q being interpolated. The quantities that are interpolated are the effective temperature as a function of colatitude, the equatorial radius, fractional radius as a function of colatitude, and the surface equatorial velocity.

The accuracy of the interpolation code has been tested using a 14 $M_\odot$ evolutionary track calculated with ROTORC having a ZAMS rotation speed of 498.46 km s^{-1} with solid body rotation, no overshooting, and the same metal abundance as the grid of ROTORC models used for interpolation. The rotation index (5.4863) of the interpolated model was chosen so that the surface equatorial velocities at the ZAMS of the interpolated model matched that of the ROTORC model calculated at the ZAMS. The accuracy of interpolating the effective temperature and fractional radius as a function of colatitude and equatorial radius was determined by interpolating models at ages of 0 0.009 and 0.0110282 byr at a mass of

14 $M_\odot$ and a rotation index of 5.4863. The maximum relative errors of the interpolated quantities are as follows: 0.6% for the ROTORC effective temperature as a function of colatitude (corresponding to 190 K at a temperature of 30,000 K), 1.2% for the fractional radius as a function of colatitude (corresponding to 0.011 at a fractional radius of 0.935), and 0.7% for the equatorial radius (corresponding to 0.06 $R_\odot$ at a equatorial radius of 8.4 $R_\odot$).The relative error in interpolating the surface equatorial velocity was also found to be 0.2% (corresponding to 0.67 km s^{-1} at a velocity of 292.39 km s^{-1}). However, because the surface equatorial velocity was used as a means of determining the rotation index for the interpolation, the test would only determine the accuracy of the interpolator with age, because the rotation index was fit on the ZAMS. In addition, an interpolated evolutionary track for the 14 $M_\odot$ ROTORC track was compared with that computed by ROTORC. The result is shown in figure 2.7. The two curves are quite close in $\log T_{\text{eff}}$ and $\log L$, and have differences characteristic of the uncertainties mentioned above. The plotted $\log T_{\text{eff}}$ and $\log L$ in figure 2.7 are the ROTORC luminosity and effective temperature.

3 RESULTS

3.1 SELECTED MEMBERS

The problem of understanding the properties of selected cluster members needs to be handled in a statistical manner, and, as such, a large number of test cases need to be computed. The test cases are used to quantify the fraction of cluster members at selected locations in the HR diagram having various inclinations and rotation rates. The fractions, C_f depends on the number of stars in a cluster. When there are more stars in a cluster, there is a wider range of rotational characteristics represented by cluster members producing different C_fs. Of course, one must recognize when comparing with observations that the number of stars in the cluster is fixed and may be too small to provide valid statistics. The calculated fractions also depend on the number of clusters that are used in the calculation. For such reasons, the first step in the analysis is to compute synthetic clusters ranging from 20 to 500 member stars in increments of 20 members, resulting in 25 sets, each composed of 500 clusters. All clusters have a mass range of 3 $M_\odot$ to 15 $M_\odot$, an inclination range of 0° to 90°, a rotation index range of 1 to 6 (essentially, zero to critical rotation), and an age of 11 Myr. Figure 3.1 and figure 3.2 show two characteristic clusters with 160 and 340 member stars respectively. Open circles show rapidly rotating stars, with rotation indices between 3.5 and 6 (surface equatorial velocities of 308 km s^{-1} to 570 km s^{-1} for a 15 $M_\odot$ ZAMS star), and viewed nearly equator-on, with inclinations between 60° and 90°. Open diamonds show rapidly rotating stars, with rotation indices between 3.5 and 6, and viewed nearly pole-on, with inclinations between 0° and 30°. Closed circles represent all other stars in the synthetic cluster, whether they are slowly rotating stars at any inclination, or rapidly rotating stars with inclinations between 30° and 60°. Since cluster members are displayed with different symbols, it can be seen that the rapidly rotating stars seen pole-on are generally the brightest and hottest cluster members. It can also be noted that the rapidly rotating equator-on stars are nearly always to the redder side of the main sequence turnoff. Finally, one can see that it is difficult to distinguish between a rapidly rotating massive star viewed equator-on and a less massive rapidly rotating star viewed pole-on along the main sequence below the turnoff.

The selected members that were studied in this analysis are as follows: the brightest core hydrogen burning star in the cluster, the bluest star in the cluster, and the reddest star above a predefined luminosity cutoff in the cluster. These qualifiers for selected members were chosen based on our knowledge of the inclination curves discussed in section 2.2. The ability of the inclination curve to produce the selected members in the cluster is greatly hindered along the main sequence because the effects of moving along the inclination curve are nearly identical to those of changing mass, which is referred to here as mass effects. However, the main sequence is widened by rotation independent of the inclination. As a star rotates more rapidly, the overall inclination curve moves to lower temperatures and higher luminosities, as can be seen in figure 2.4. At higher masses, cluster members are beginning to move noticeably off the ZAMS which is referred to as the main sequence turnoff. Their luminosity and temperature begin to change with mass in a direction that is no longer parallel to that of the inclination curve and the inclination curve is no long parallel to the to main sequence. Hence, selected members are now produced. The region above the main sequence turnoff is therefore the target of this analysis.

The brightest core hydrogen burning star in the cluster is likely to be viewed pole-on and to be rapidly rotating, as that corresponds to the most luminous part of the inclination curve. The fraction, C_f, of clusters with the brightest star in the rotation index range from 3.5 to 6 and inclination range of 0° to 30°, as a function of the number of stars in the cluster, is shown in figure 3.3 (a) using 500 synthetic clusters. As can be seen from the example cluster in figure 3.1, the most luminous star in this particular cluster is not rapidly rotating and not viewed pole-on, but is more massive than the second most luminous star which is rapidly rotating and viewed pole-on. As the number of stars in the cluster increases there are more massive stars and the fraction of clusters having both a massive and rapidly rotating star viewed pole-on increases. Clusters having a membership of 130 stars produce a value of C_f of 0.5 for the brightest star being rapidly rotating and seen pole-on. C_f increases as the number of stars increases, though the rate of increase shows signs of slowing at larger cluster memberships.

To determine if a sufficiently large sample of clusters was used in obtaining the results, the fraction of clusters with the brightest star in a rotation index range of 3.5 to 6 and inclination range from 0° to 30° was plotted as a function of the number of clusters up to 500 clusters, each cluster with 340 stars. The results are shown in figure 3.3 (b). As can be seen from the figure, approximately 150-200 clusters and greater will give reasonably consistent fractions.

To examine how the fraction of clusters with brightest stars within the specified range changes as the inclination range changes, the fraction of clusters with the brightest star in the rotation index range of 3.5 to 6 and an inclination range from 0° to a varying maximum inclination is shown in figure 3.3 (c). One can see that as the inclination range increases, so does the fraction of clusters with the brightest star in the defined range. More interesting is that an inclination range from 0° to 50° includes all the brightest stars which are within the given rotation index range. It indicates that any of the other brightest stars are more slowly rotating stars below the lower bound of the rotation index range of 3.5. These stars are likely either more massive stars which are more evolved than the other stars or moderately rotating stars viewed nearly pole-on, or a combination of both. It also means that no stars that are rapidly rotating with inclinations greater than 50° are ever selected as the brightest cluster members in this sample of clusters. Again, that is expected as higher inclinations will move the star to lower luminosities (see figure 2.4).

To investigate how the fraction of clusters with the brightest star within the specified ranges changes as the rotation range varies, the fraction of clusters with the brightest star having a rotation index in the range of a varying minimum to 6 and inclination in the range from 0° to 30° is plotted in figure 3.3 (d). As can be seen, the fraction of clusters with the brightest star within the specified ranges increases rather rapidly up to a minimum rotation index of about 3.3, slightly over half the rotation index range. After that, the curve flattens out considerably and only increases slightly. The curve continues to increase, though slowly, indicating that some of the brightest stars are from slowly rotating stars, seen nearly pole-on.

The same four plots created for the brightest star in the cluster were produced for the other two types of selected members considered: the bluest star, and the reddest star above a predefined luminosity cutoff. Unlike the other two types of selected members considered, the luminosity cutoff involves more work than merely picking the maximum or minimum of luminosity or temperature. A luminosity is used, below which stars are not included in the search for the reddest cluster member, because the main sequence becomes progressively cooler at lower luminosities. Thus, the luminosity limit was chosen to exclude stars that would be redder merely because of a lower mass. This luminosity corresponds to the luminosity at which the cluster begins to turn off the ZAMS noticeably. This luminosity changes with the age of the cluster because lower mass stars are turning off the ZAMS. A plot of the chosen cutoff luminosity, as a function of age, is shown in figure 3.4. Plotted as solid curves are isochrones generated from non-rotating ROTORC evolutionary tracks at ages from 0 to 24 Myr in steps of 2 Myr with a mass range of 3 to 15 $M_{\odot}$. The dashed line shows the luminosity that is used as a luminosity cutoff. Once an age is selected, the luminosity cutoff can be taken from the curve. The dashed line is parallel to the ZAMS but shifted upwards by 0.38 in $\log(L/L_{\odot})$.

Figure 3.5 (a), (b), (c) and (d) are the corresponding four plots for the reddest star above a $\log(L/L_{\odot})$ cutoff of 4.11 corresponding to the age of 11 Myr. The range in rotation index is again 3.5 to 6, the range for the inclination is now 60° to 90°, viewed equator-on to place the star in the lower temperature regime of the inclination curve. The general trends seen here are similar to the results shown in figure 3.3, only with a much higher fraction of clusters with the reddest star within the specified rotation and inclination ranges. The higher fraction of clusters results from using the luminosity cutoff to eliminate most stars of lower mass and slower rotation, and from the fact that higher mass stars will be so cool only if they are rapidly rotating. The fraction of clusters with the reddest star above a luminosity cutoff that is rapidly rotating and seen pole-on is 0.5, when the membership of the clusters is 50 stars. At a membership of 150 stars the fraction of clusters with the reddest star above a luminosity cutoff that is rapidly rotating and seen pole-on is 0.84.

When membership of the clusters is increased from 150 to 500 stars, there is only a modest increase in the fraction of clusters with the reddest star above a luminosity cutoff being rapidly rotating and seen pole-on.

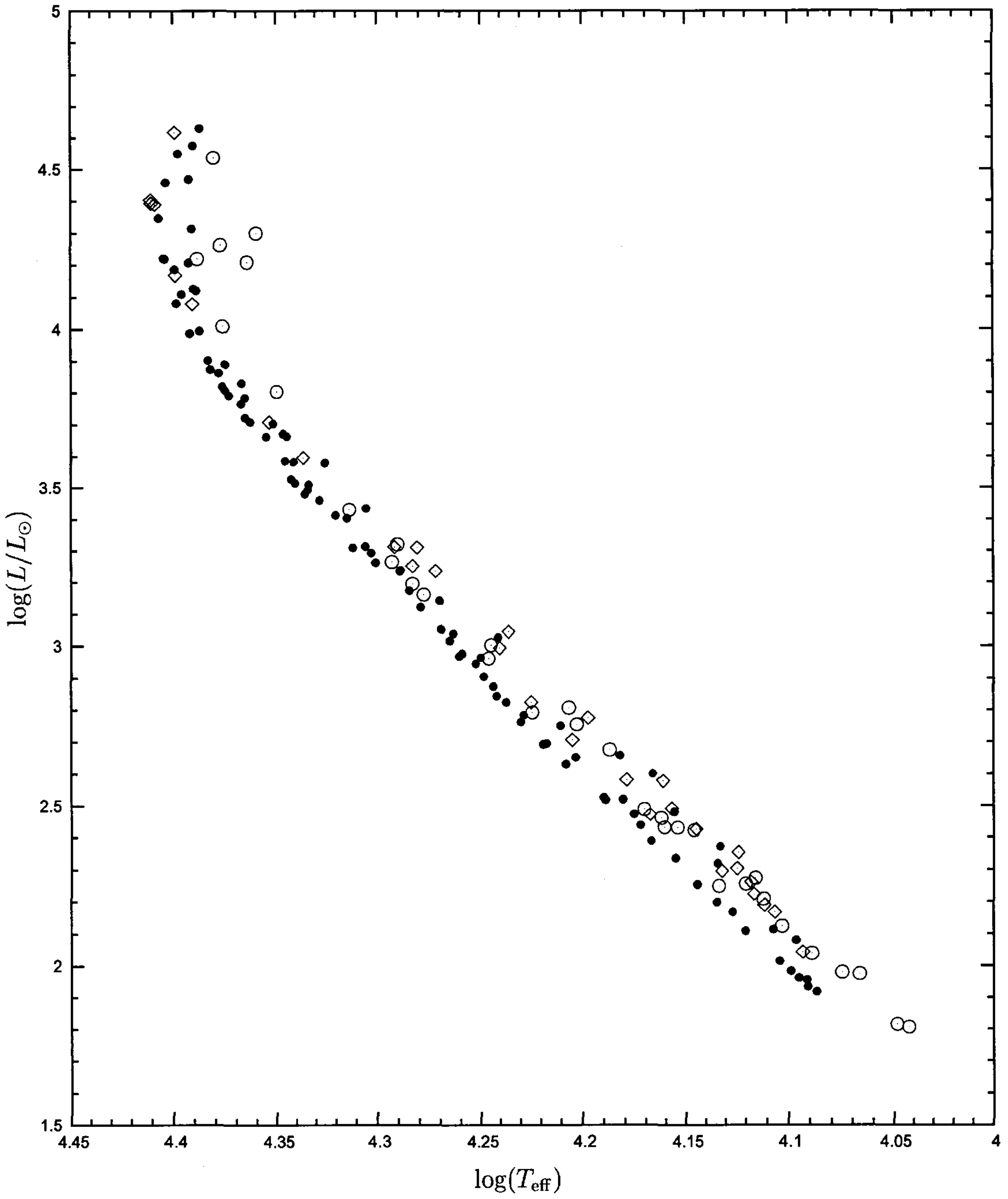

Figure 3.1: Characteristic clusters from the sample of 12,500 clusters with a 160 member stars. Open circles denote rapidly rotating (rotation index between 3.5 and 6) equator-on (inclination between 60° and 90°) stars. Open diamonds denote rapidly rotating (rotation index between 3.5 and 6) pole-on (inclination between 0° and 30°) stars. Filled circles are slowly rotating stars or stars which are rapidly rotating and in the inclination range 30° to 60°.

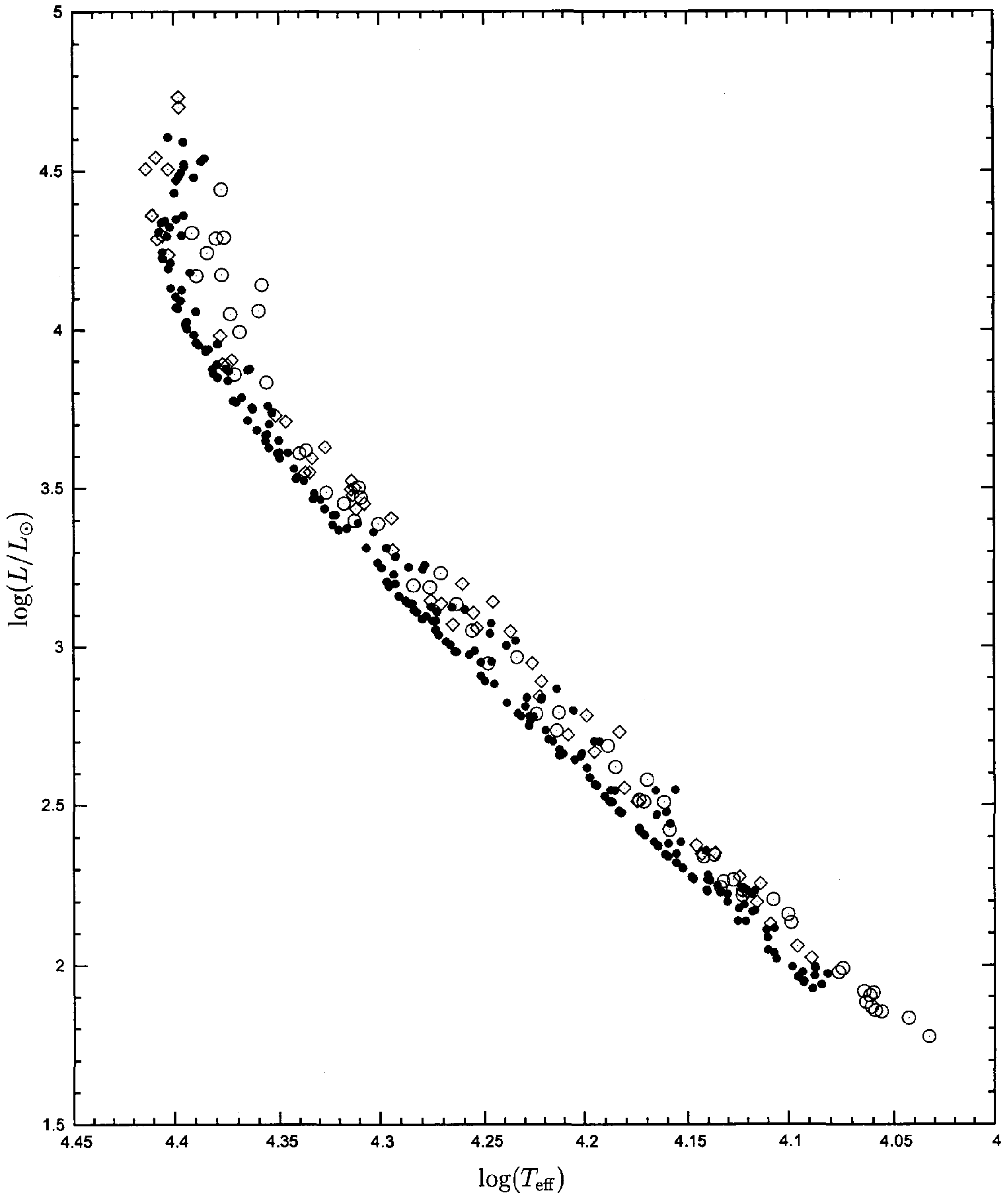

Figure 3.2: Characteristic cluster from the sample of 12,500 clusters with 340 member stars. Open circles denote rapidly rotating (rotation index between 3.5 and 6) equator-on (inclination between 60° and 90°) stars. Open diamonds denote rapidly rotating (rotation index between 3.5 and 6) pole-on (inclination between 0° and 30°) stars. Filled circles are slowly rotating stars or stars which are rapidly rotating and in the inclination range 30° to 60°.

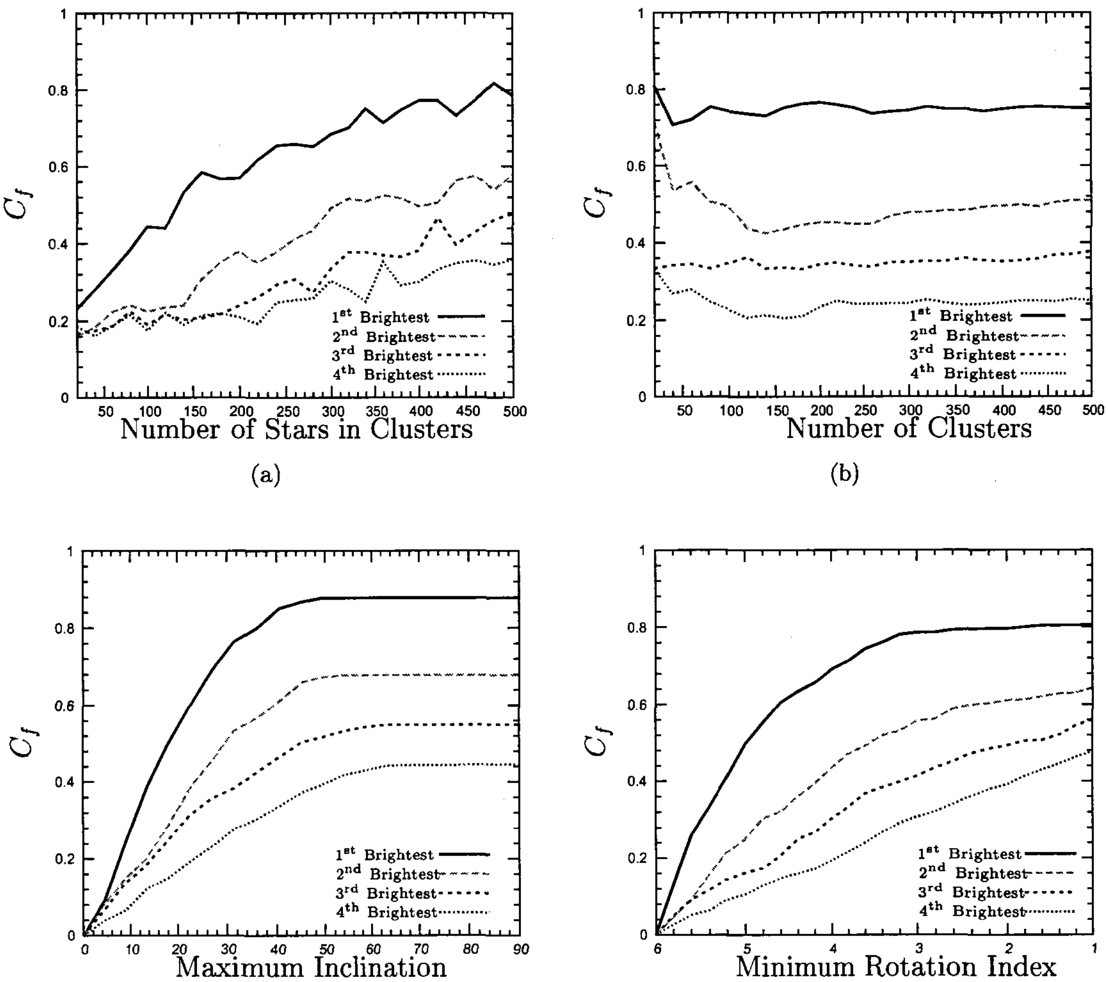

(a) (b)

(c) (d)

Figure 3.3: (a) is a plot of the fractions of clusters with the first, second, third, and fourth brightest stars within the rotation index and inclination ranges of 3.5 to 6 and 0° to 30° respectively, plotted as a function of the number of stars in the cluster. (b) is a plot of the four brightest stars within the same rotation index and inclination range as (a) but as a function of the number of clusters. (c) is a plot of the fraction of clusters with a first, second, third, and fourth brightest star within the rotation index and inclination ranges of 3.5 to 6 and 0° to a varying maximum inclination respectively. (d) is a plot of the fraction of clusters with a first, second, third, and fourth brightest stars within the rotation index and inclination ranges of a varying minimum to 6 and 0° to 30° respectively. Plots (c) and (d) were both computed from 500 clusters, each with 340 stars.

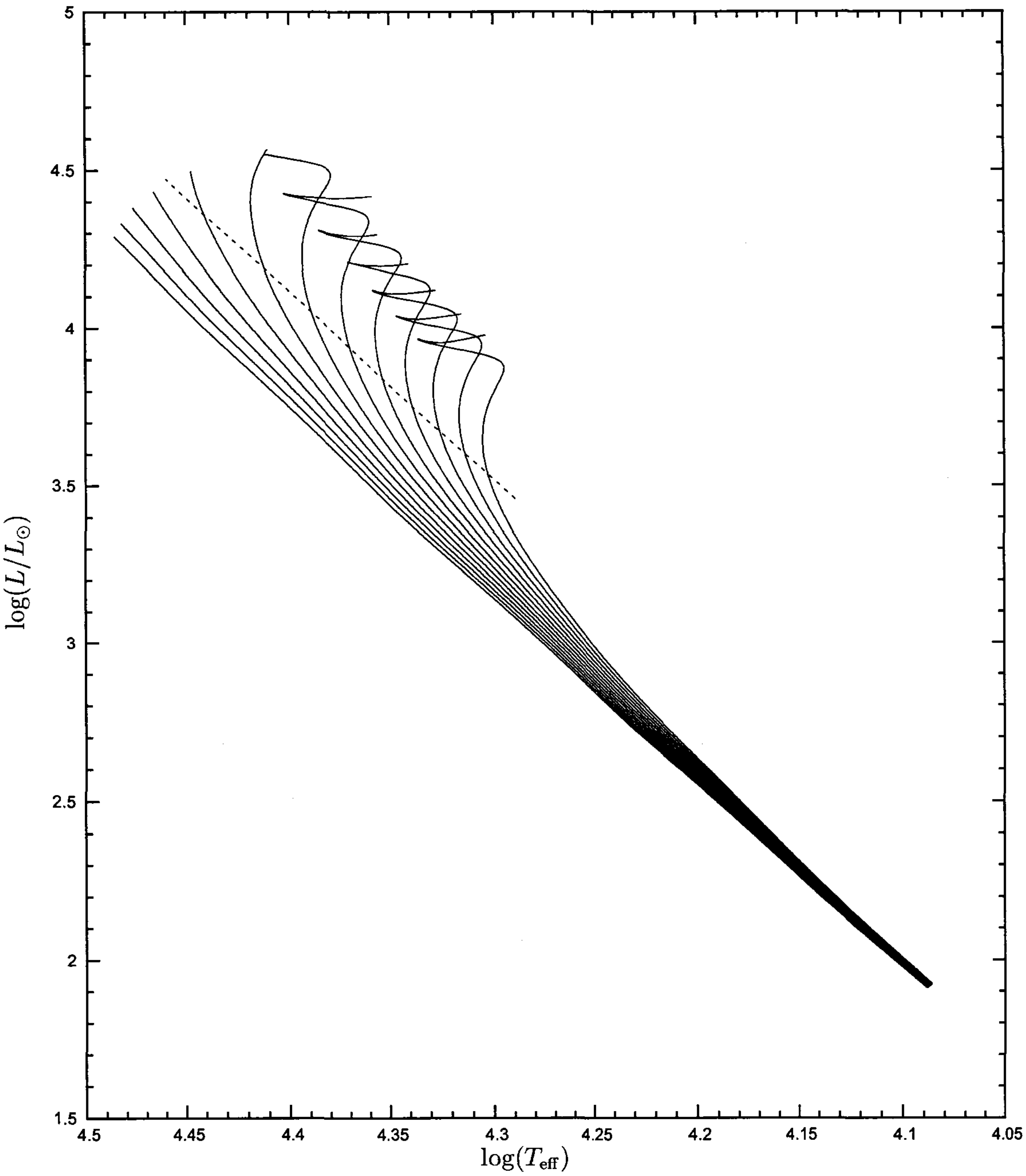

Figure 3.4: This plot illustrates how the luminosity cutoff for the reddest cluster member is determined. Plotted are isochrones generated from non-rotating ROTORC evolution tracks at ages from 0 to 24 Myr in steps of 2 Myr. The dashed line is parallel to the ZAMS and indicates the luminosity cutoff as a function of the age of the isochrone the line is crossing.

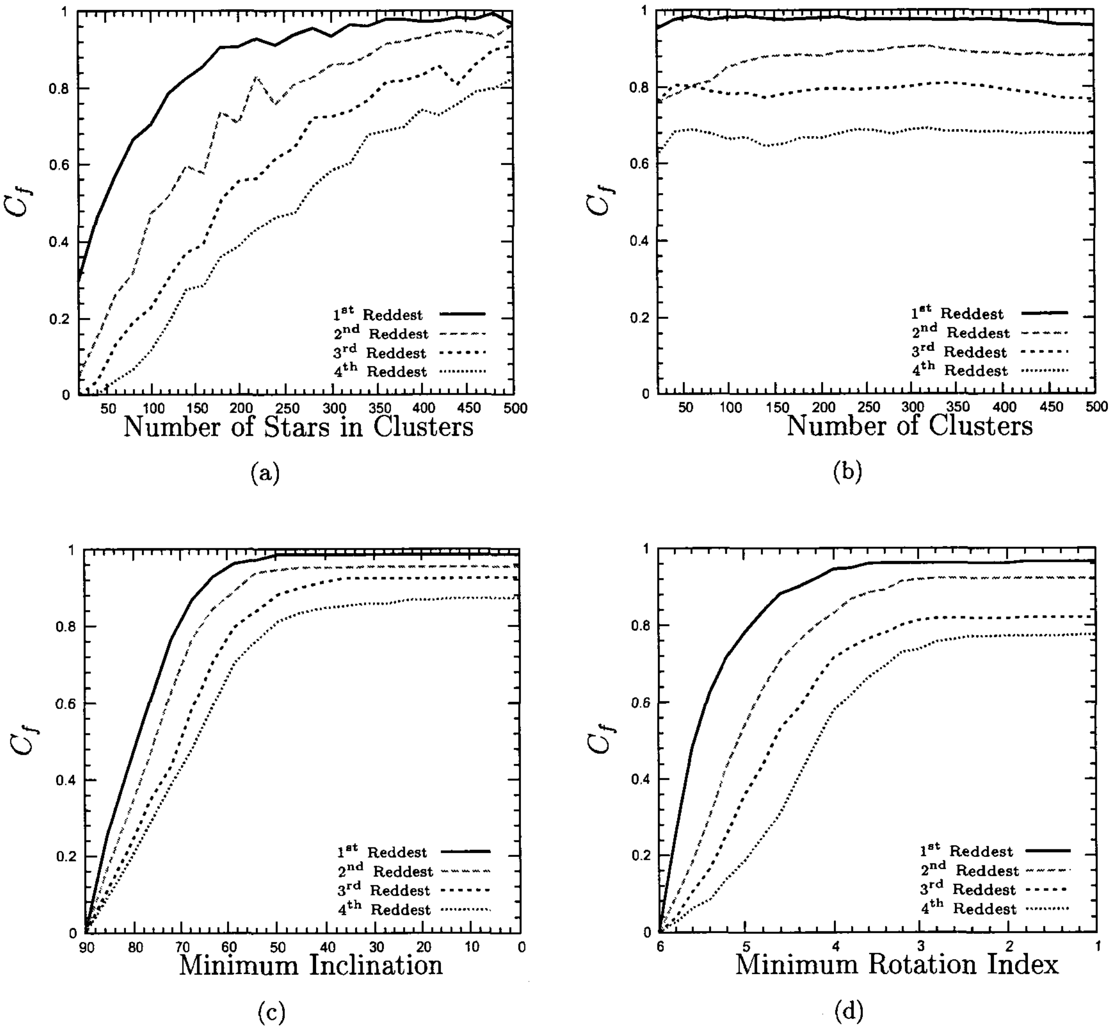

Figure 3.5: (a) is a plot of C_f for the four reddest stars above a luminosity cutoff having rotation rates and inclinations within the rotation index and inclination ranges of 3.5 to 6 and 60° to 90° respectively, plotted as a function of the number of stars in the cluster. (b) is a plot of the four reddest stars above a luminosity cutoff within the same rotation index and inclination range as (a) but as a function of the number of clusters. (c) is a plot of C_f having the reddest star above a luminosity cutoff within the rotation index and inclination ranges of 3.5 to 6 and a varying minimum to 90° respectively. (d) is a plot of C_f having the reddest star above a luminosity cutoff within the rotation index and inclination ranges of a varying minimum to 6 and 60° to 90° respectively. Plots (c) and (d) were both computed from 500 clusters, each with 340 stars.

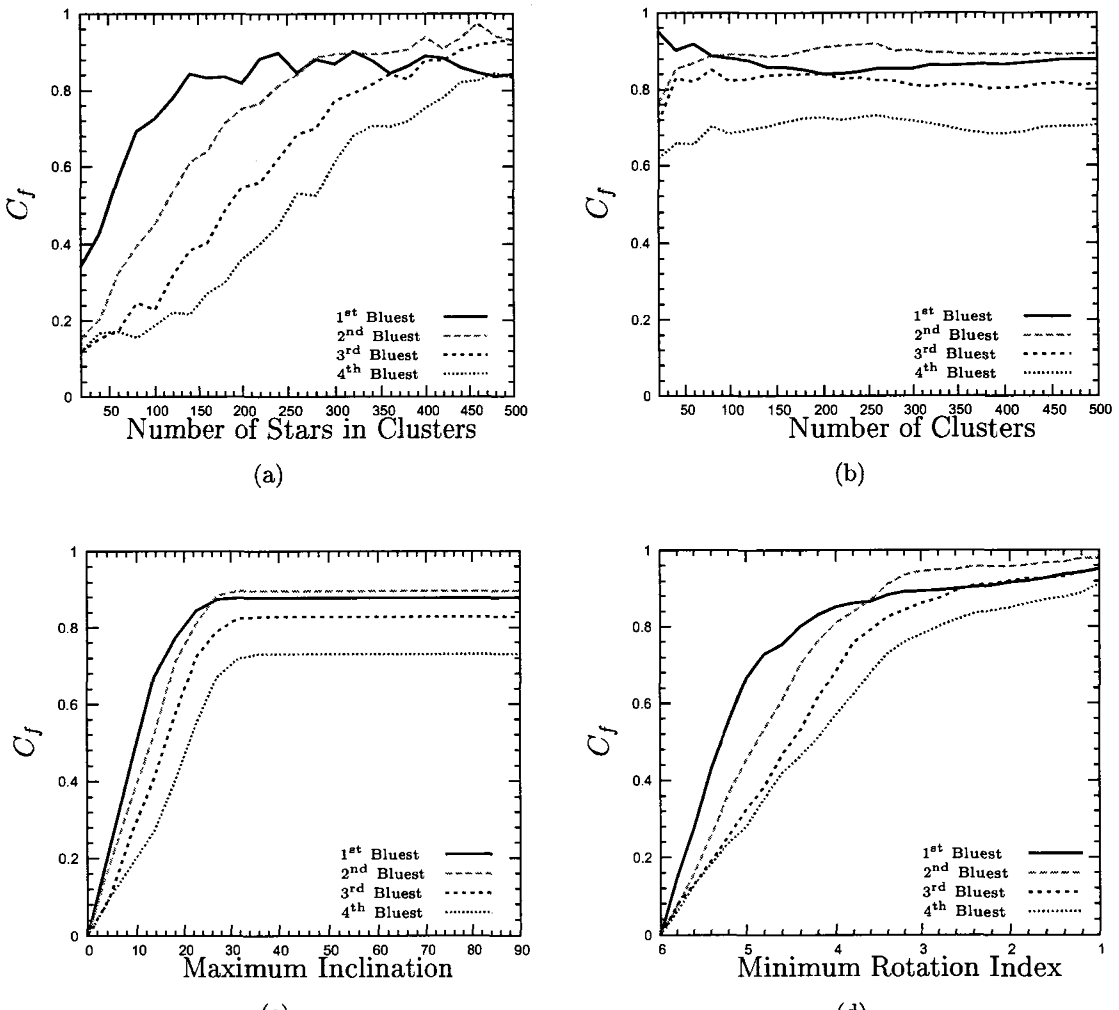

Figure 3.6: (a) is a plot of C_f for the four bluest stars of being within the rotation index and inclination ranges of 3.5 to 6 and 0° to 30° respectively, plotted as a function of the number of stars in the cluster. (b) is a plot of the four reddest stars above a luminosity cutoff within the same rotation index and inclination range as (a) but as a function of the number of clusters. (c) is a plot of C_f having the bluest member within the rotation index and inclination ranges of 3.5 to 6 and 0° to a varying maximum respectively. (d) is a plot of C_f having the bluest member within the rotation index and inclination ranges of a varying minimum to 6 and 0 to 30° respectively. Plots (c) and (d) were both computed from 500 clusters, each with 340 stars.

The final type of selected member that was examined was the bluest star in the cluster (i.e., hottest). Figure 3.6 shows the corresponding four plots for this case. A rapidly rotating star seen pole-on appears hotter than a slower rotating star or a star seen at a higher inclination (see figure 2.4). Thus, it is expected that the bluest star will likely be rapidly rotating and seen pole-on. The range in rotation index is again 3.5 to 6, the range for the inclination is again 0° to 30°. When the membership of the synthetic cluster reaches 50 stars, half of the clusters ($C_f = 0.5$) have the bluest star being rapidly rotation (a rotation index between 3.5 and 6) and viewed pole-on (an inclination between 0° and 30°). At a membership of 140 stars, $C_f = 0.84$ for the bluest star being viewed pole-on and rapidly rotating. C_f increases very little for increased memberships from 140 to 500 stars.

Interestingly, as seen in figure 3.6 (a), the first bluest star's C_f drops below that of the second bluest star's C_f as the number of stars increases. This can be understood by looking at figure 3.7, a plot of the HR diagram of a cluster of 380 stars with the bluest star represented by an open circle and the second bluest star by an open diamond. The dashed curve shows the isochrone for non-rotating stars corresponding to the cluster's age. The bluest star is one of the most massive stars and is nearly non-rotating, while the second bluest star is a rapidly rotating star seen pole-on. The reason for the decrease in C_f for the bluest star below that of the second bluest star, as the number of stars in the cluster increases, is that the mass bins (see equation 2.66 and equation 2.67) for the cluster members become small enough for stars to start populating the gravitational contraction phase of evolution (between ② and ③ in figure 2.6 (a)). As long as there is a star in the upper mass range that is hotter than the bluest star near the main sequence turnoff, the bluest star may have any rotation or inclination properties so long as it is massive. If there were a sufficient number of stars in the gravitational contraction phase, then rotational properties could again start to play a role. The time a star spends in the gravitational contraction phase, however, is short compared to the main sequence lifetime, and the number of stars in a cluster would need to be greater than the largest number of stars (500) considered here to populate the gravitational contraction phase to this extent.

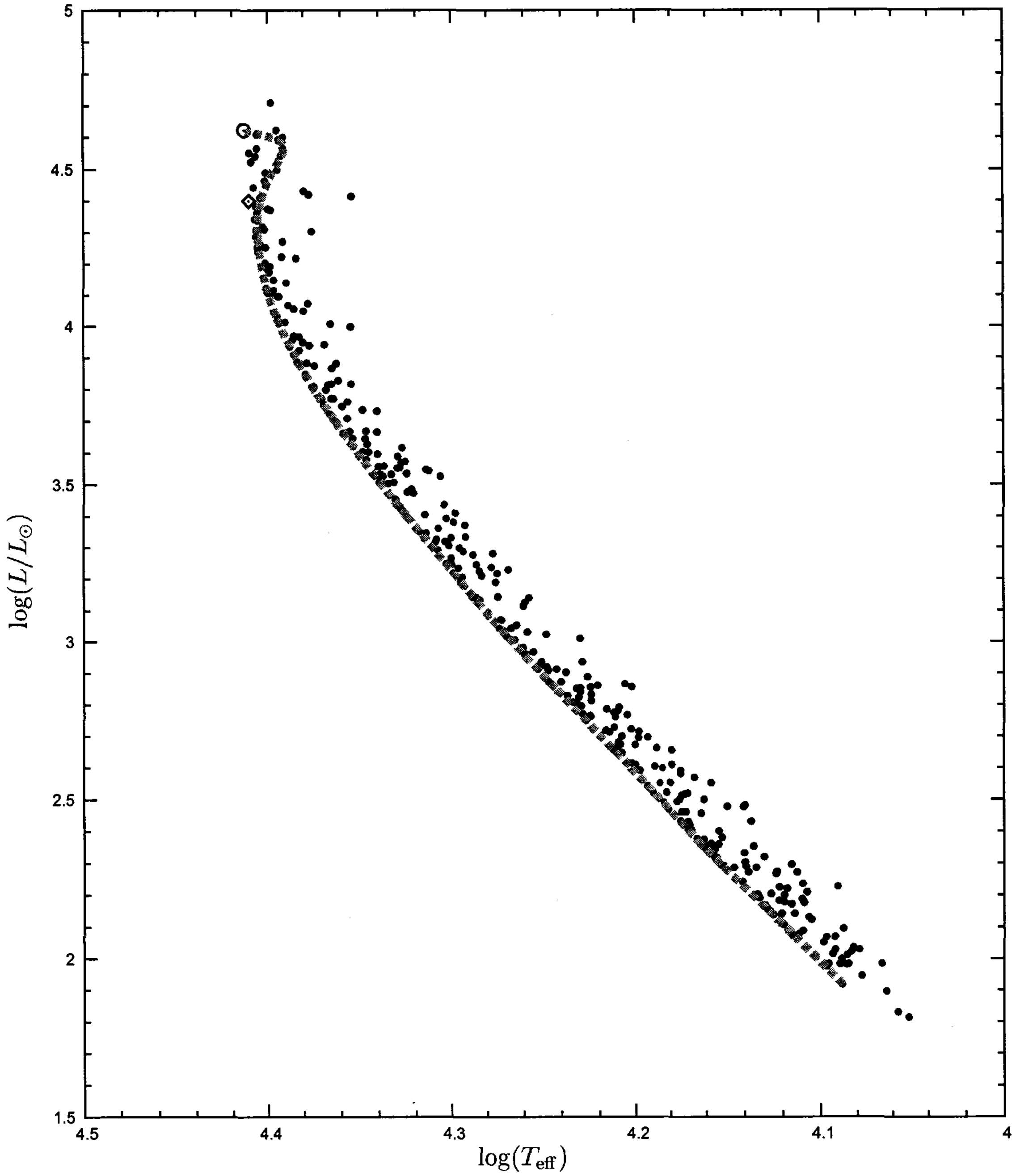

Figure 3.7: Plotted is a cluster illustrating the cause of the trend seen in figure 3.6. The open circle is the bluest cluster member and the open diamond is the second bluest cluster member. The open circle is a massive nearly non-rotation model where as the diamond is a pole-on rapidly rotating star. The dashed line is a non-rotating isochrone of the same age as the cluster. The filled circles are the rest of the cluster members.

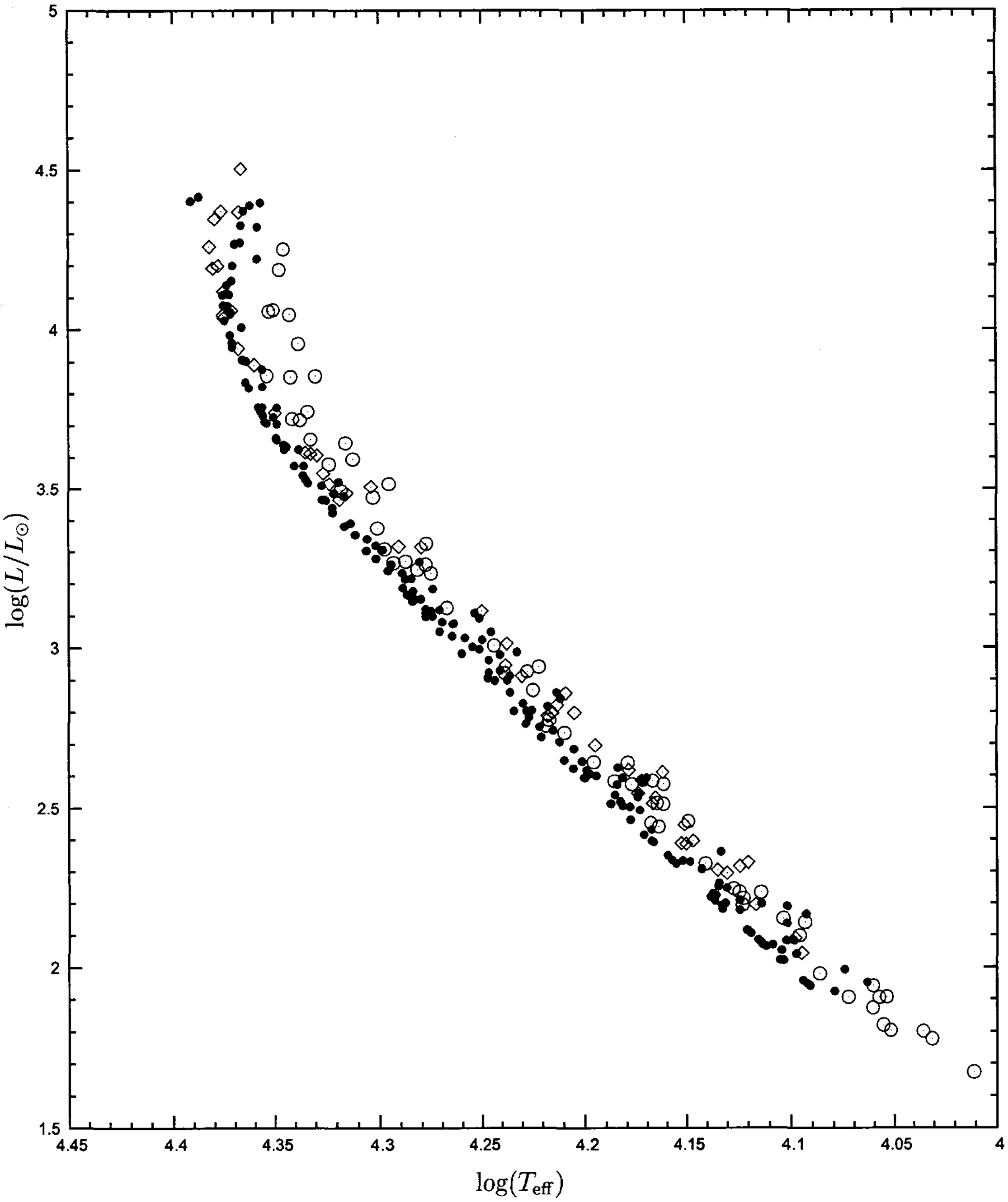

Figure 3.8: Plotted is a 14 Myr cluster with 340 members. The open circles are rapidly rotating equator on stars (rotation index and inclination ranges of 3.5 to 6 and 60° to 90°). The open diamonds are rapidly rotating pole-on stars (rotation index and inclination ranges of 3.5 to 6 and 0° to 30° respectively). The filled circles are the remaining members.

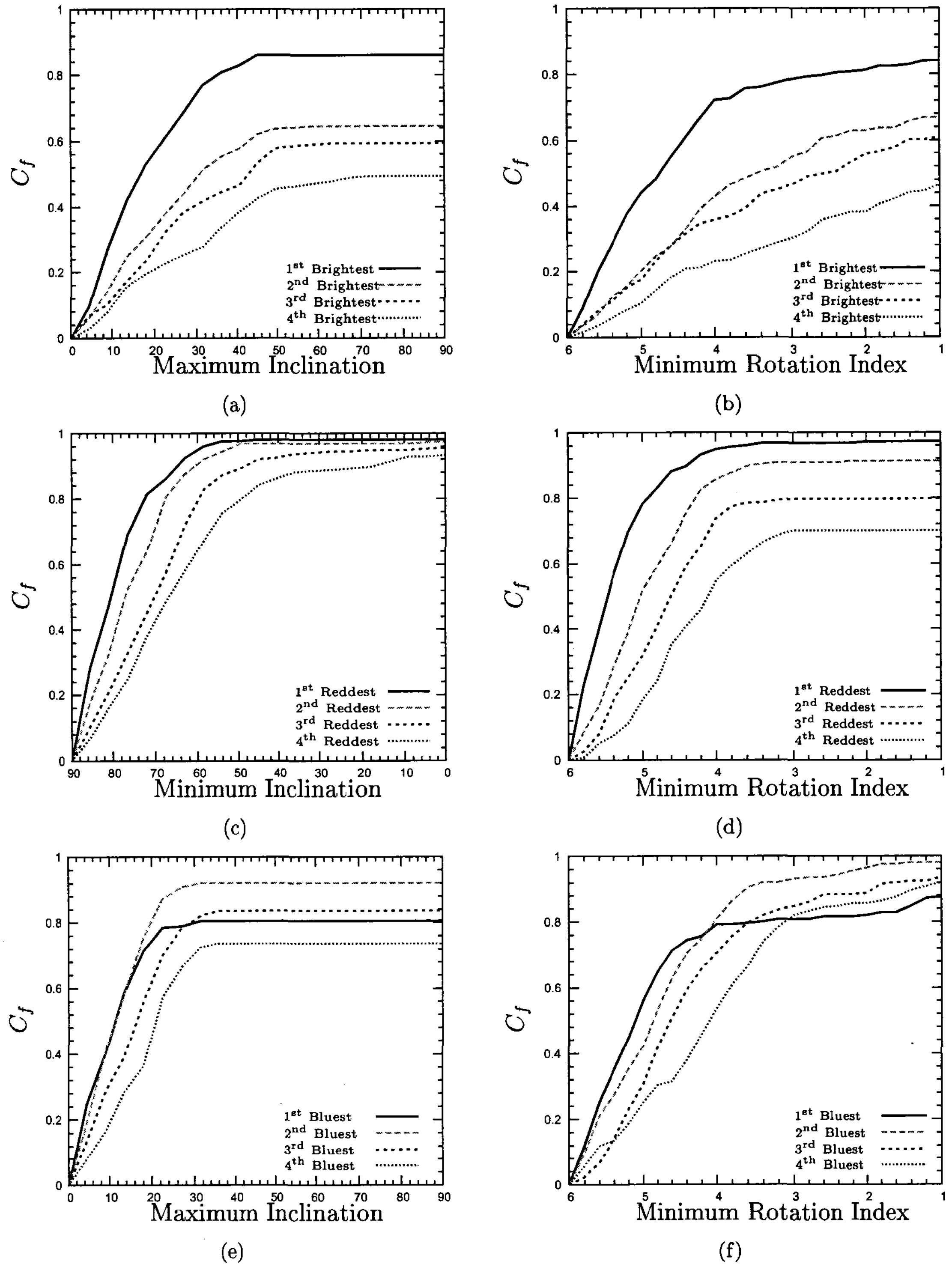

(a) (b)

(c) (d)

(e) (f)

Figure 3.9: These plots have been produced from a set of 250 clusters each with 340 stars at an age of 14 Myr. The above plots have the same ranges, from top to bottom, as figures 3.3 (c) and (d), figures 3.5 (c) and (d) and figures 3.6 (c) and (d) respectively.

From the isochrone for figure 3.7, it is noted that the age of 11 Myr for the most massive stars is no longer on the evolutionary tracks for all rotations. In the upper portions of the evolutionary tracks, the model's luminosity and temperature are changing rapidly and a small difference in age can correspond to a large difference in the evolutionary phase of the models. This results in a premature ending of the track, because two tracks at the same mass and at different rotations can end at the same phase of evolution at different ages. This is an issue only when the cluster's age is near the terminal age for main sequence. Older or younger ages will not correspond to these rapidly changing evolutionary phases and will not have this issue. To explore the effects of the premature ending in our cluster's mass distribution, a set of 250 clusters at an age of 14 Myr, each cluster consisting of 340 stars, was computed. At this age the most massive stars are completely off the end of the evolutionary track, after rapidly moving to cooler temperatures on the HR diagram. The results of this set of computations are shown in figure 3.9 for the three types of selected members: the brightest, reddest above a luminosity cutoff, and the bluest. The results are nearly the same for the brightest and reddest cluster members, with C_f only changing by a few hundredths. Such a small change can be explained by a different and smaller sample of clusters. The bluest cluster member's C_f has dropped below even the third bluest member at a maximum of 30° (figure 3.9 (e)), and below even the fourth brightest when the minimum rotation index is below 3 (figure 3.9 (f)).

3.2 DIFFERING ROTATION DISTRIBUTIONS

To examine if the width of the main sequence can be used as an indicator of the distribution of rotation among cluster members, sets of 250 clusters consisting of 340 stars with differing rotation distribution powers, p, in equation 2.63 were created. This sample of synthetic clusters can also be used to examine how C_f for the selected members having specific rotational characteristics is affected by different rotation distributions among cluster members. 20 sets were created with $p = 1$ to 10.0, in steps of 0.5. Recall that increasing p produces more stars which are slowly rotating. A typical cluster from the set with $p = 10.0$ is shown in figure 3.10 in order to illustrate the effects of the increased rotation distribution power on the synthetic clusters. The three selected member types have been re-examined with $p = 5.0$ and $p = 10.0$ and are shown in figures 3.11 and 3.12 respectively.

A value of p decreasing from 1 to 0 increases the number of rapidly rotating stars in the cluster. More rapid rotators improve C_f for the three considered types of selected members being within the rotation index and inclination ranges considered (see figure 3.13). The examination of the effects on C_f is aimed at determining for which rotation distribution power C_f is no longer meaningful. When fewer than half the clusters have selected members which meet the specified rotational characteristics (C_f=0.5) it becomes equally likely that the selected members meet or do not meet the specified criteria.

In figure 3.11 for $p = 5.0$ the brightest star's C_f, with an inclination range from 0° to 50° and a rotation index range of 3.5 to 6, has decreased to 0.34. The reddest star above the luminosity cutoff with an inclination range of 40° to 90° and a rotation index range of 3.5 to 6 has a C_f of nearly 0.8. The bluest star has a higher C_f, at 0.56, than the brightest star in the same inclination and rotation index range, but still not nearly as large a C_f as the reddest star above a luminosity cutoff.

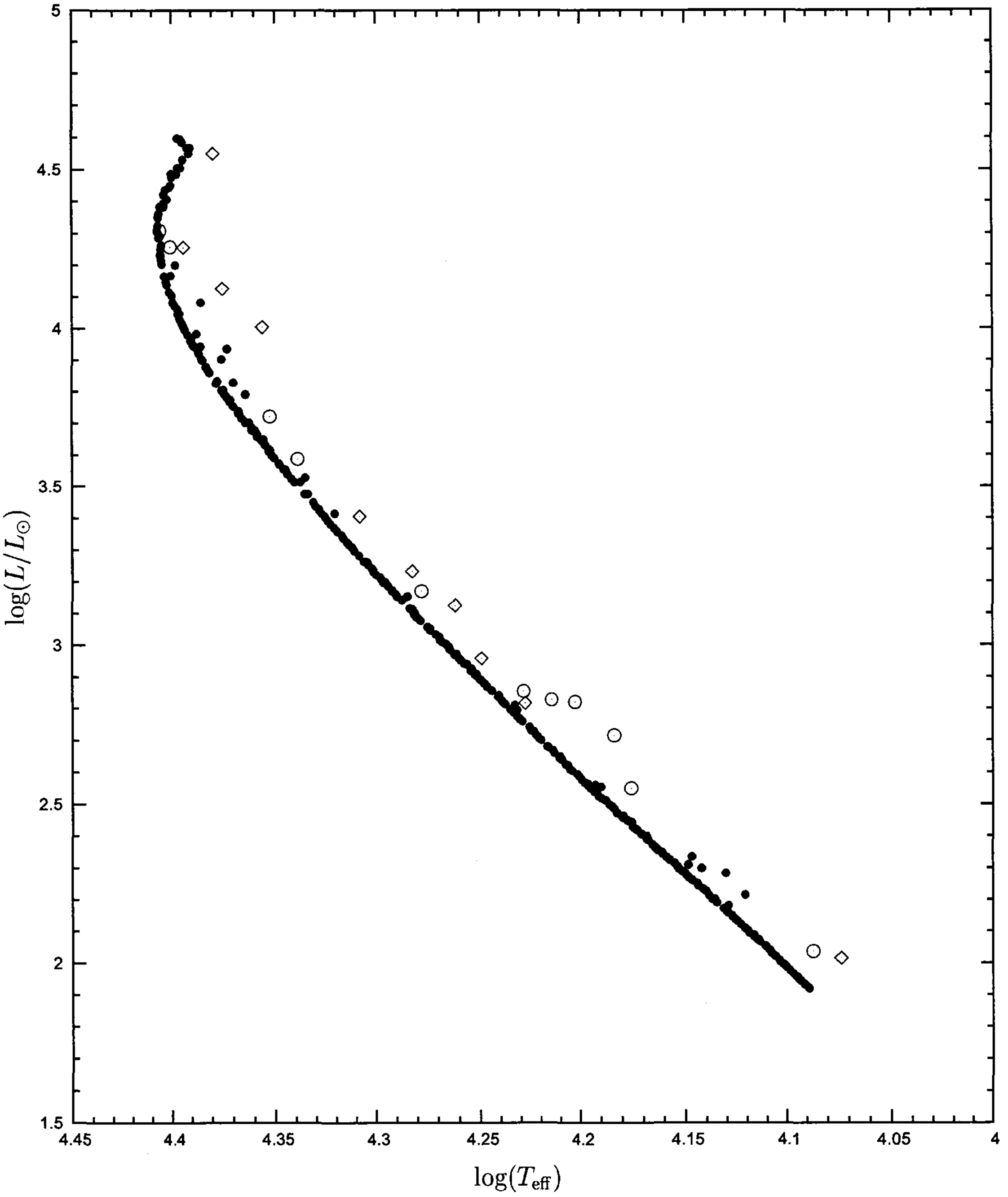

Figure 3.10: Plotted is a cluster with 340 members and a rotation distribution power, p, of 10. The open circles are rapidly rotating equator-on stars (rotation index and inclination ranges of 3.5 to 6 and 60° to 90°) The open diamonds are rapidly rotating pole-on stars (rotation index and inclination ranges of 3.5 to 6 and 0° to 30° respectively). The filled circles are the remaining members.

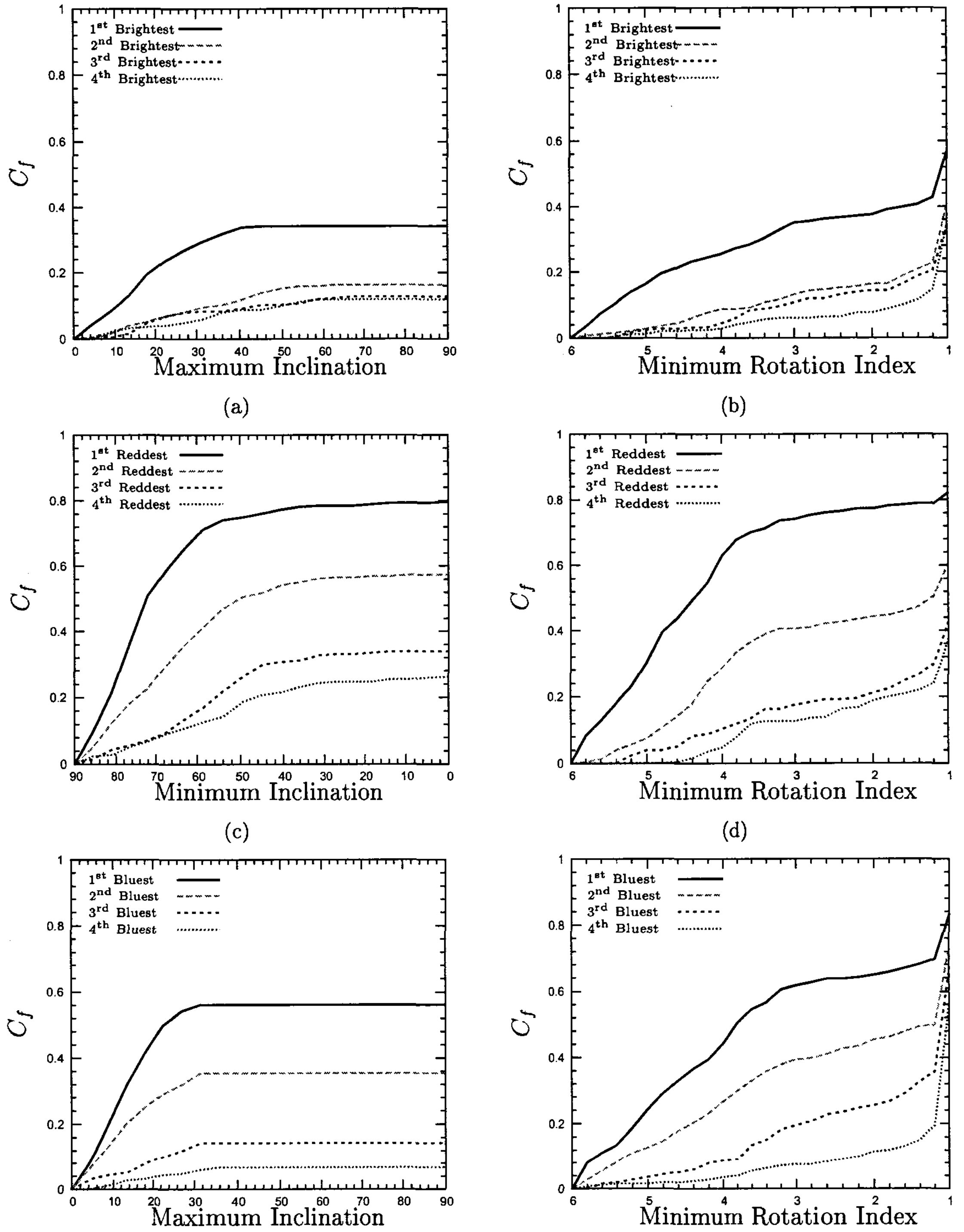

(a) (b)

(c) (d)

(e) (f)

Figure 3.11: These plots have been produced from a set of 250 clusters with a rotation distribution power of $p = 5$. The above plots have the same ranges, from top to bottom, as figures 3.3 (c) and (d), figures 3.5 (c) and (d) and figures 3.6 (c) and (d) respectively.

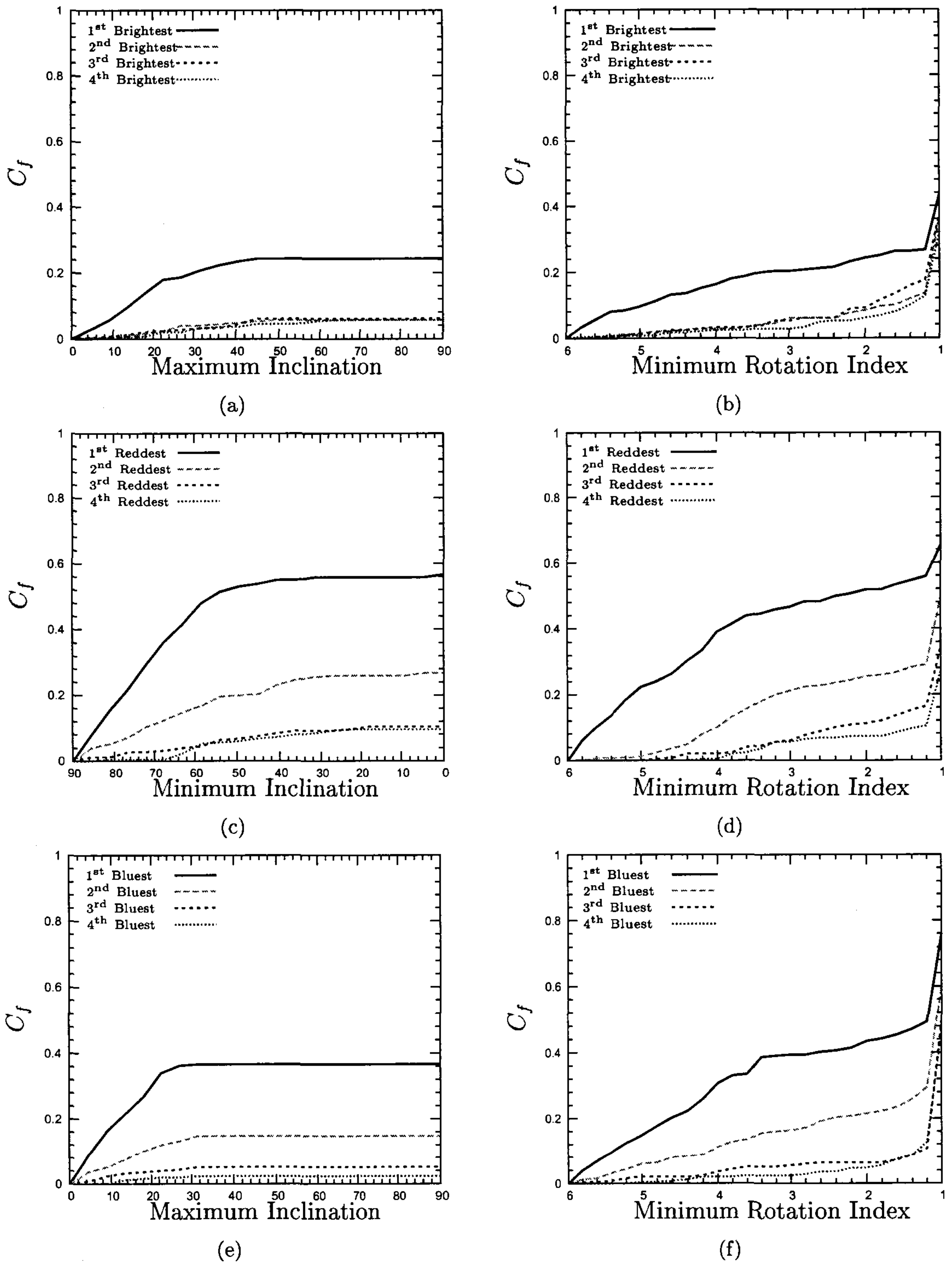

(a) (b)

(c) (d)

(e) (f)

Figure 3.12: These plots have been produced from a set of 250 clusters each with 340 stars at a rotation distribution power of $p = 10$. The above plots have the same ranges, from top to bottom, as figures 3.3 (c) and (d), figures 3.5 (c) and (d) and figures 3.6 (c) and (d) respectively.

In figure 3.12 at $p = 10.0$ the brightest star has decreased to a C_f of 0.24 in the inclination range from 0° to 40° and rotation index range of 3.5 to 6. The reddest star at a $p = 10.0$ has decreased to a C_f of 0.46 in the inclination range from 60° to 90° and rotation index range of 3.5 to 6. Finally at a $p = 10.0$ the bluest star has decreased to a C_f of 0.36 in the same inclination and rotation range as the brightest star.

It is expected that C_f spikes when the very slow rotators are included, as can be seen in figures 3.11 (b), (d), and (f), and figures 3.12 (b), (d), and (f). That is because the rotation distribution powers have created so many more slowly rotating members that their inclusion in the criteria drastically increases the C_f. To aid in understanding how these C_fs change as a function of p, figure 3.13 shows the C_f for the brightest, reddest above a luminosity cutoff, and bluest cluster members being within the rotation index and inclination ranges of 3.5 to 6 and 0° to 30°, 3.5 to 6 and 60° to 90°, and 3.5 to 6 and 0° to 30° respectively. The brightest, reddest above a luminosity cutoff, and bluest stars are shown with the double dashed, dashed, and solid curves respectively. The reddest and bluest stars decrease with increasing p in a nearly linear fashion; whereas the brightest star C_f drops off more rapidly initially, but the drop in C_f slows as p increases above 4. The brightest star reaches a C_f of 0.5 at a $p \simeq 2.5$. The bluest star reaches a C_f of 0.5 at a $p \simeq 5.5$ or 6.5. The reddest star reaches a C_f of 0.5 at $p \simeq 9$ or 10.

To examine if the width of the main sequence could be used as an indicator of the rotation distribution of the cluster, the bluest and reddest cluster members where found in a luminosity band from $\log(L/L_\odot) = 3$ to 3.2, and the width in $\log(T_{\rm eff})$, w, produced by the reddest and bluest members was calculated for each of the 250 clusters at each of the rotation distribution powers. This range in luminosity was chosen so that the size of the band would be small enough to reduce the measured large from differing masses of the stars within the luminosity band, but at the same time wide enough to have multiple stars within it. It was chosen to be well below from the ZAMS turnoff so that the width of the main sequence would depend only on amount of rotation and not on the length of the inclination curve. The average was calculated as:

$$\bar{w} = \frac{1}{N}\sum_{i=1}^{N} w_i, \tag{3.1}$$

where N is the number of clusters and the standard deviation, σ was calculated as:

$$\sigma = \sqrt{\frac{1}{N}\sum_{i=1}^{N}(w_i - \bar{w})^2}. \tag{3.2}$$

The results of the calculation are shown in figure 3.14. The points correspond to the average temperature width and the error bars to the standard deviation. The change in temperature width from a rotation distribution power, p, of 1 to a p of 10 is 0.013, while the minimum standard deviation is 0.008. Also, as the rotation distribution power changes from 1 to 0, the temperature width changes by 0.018 which is not very significant compared with the minimum standard deviation. While one could likely determine a difference between the two extremes of all cluster members rotating near critical rotation rate and a completely flat and even distribution of rotation rates, the intermediate rotation distributions would be difficult to discern. Thus, the main sequence width is not a very sensitive indicator of rotation distribution.

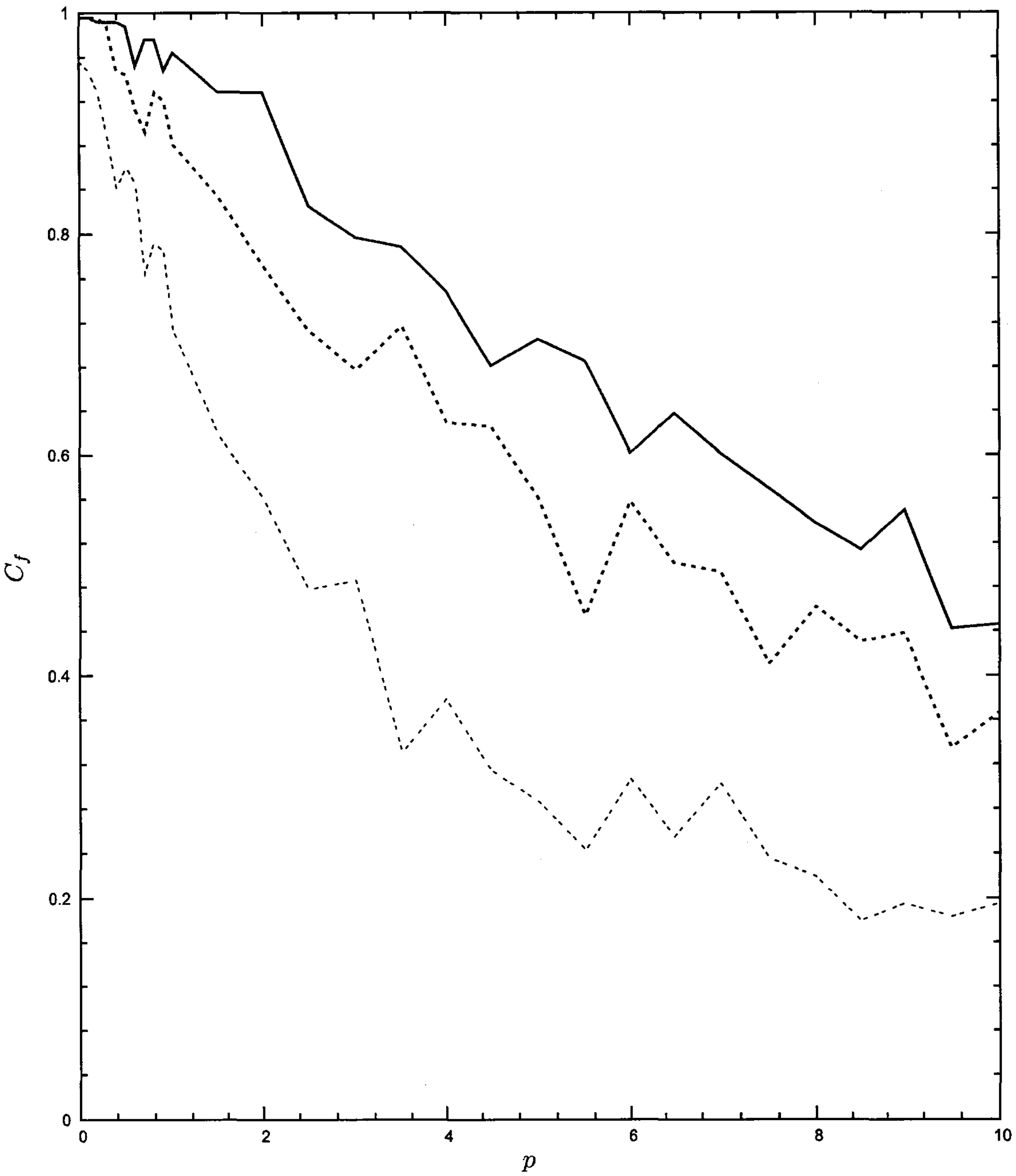

Figure 3.13: Plotted are the C_fs of the brightest star, bluest star and reddest star above a luminosity cutoff as double dashed, dashed and solid curves respectively. The rotation index and inclination ranges for the brightest star, reddest star above a luminosity cutoff, and bluest star are 3.5 to 6 and 0° to 30°, 3.5 to 6 and 60° to 90° and 3.5 to 6 and 0° to 30° respectively.

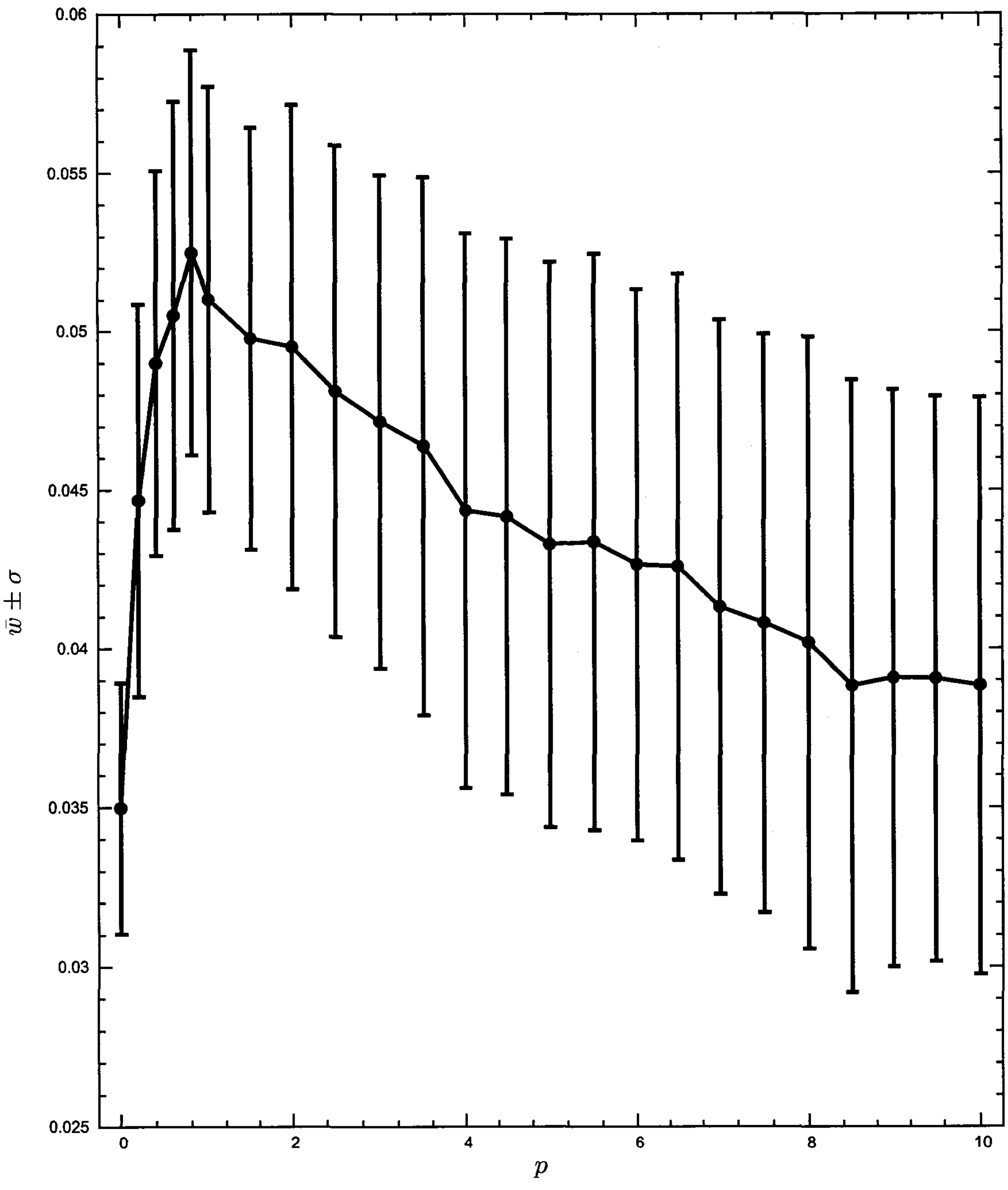

Figure 3.14: Plotted is the measured average temperature width of the main sequence on a luminosity band from 3 to 3.2 in $\log(L/L_{\odot})$. The error bars show the standard deviation of the averages.

4 COMPARISON WITH OBSERVED CLUSTERS

The results presented in the previous section provide a method for constraining a cluster member's rotation rate and inclination based on its position in the HR diagram. To make use of C_fs one must compare with observed clusters. Such a comparison is not an easy task since observed clusters have other effects besides rotation affecting the observed luminosity and effective temperature. For example stars with an unresolved binary companion can help to broaden the main sequence by allowing the combined SED to produce temperatures both to the blue and red side of the non rotating main sequence depending on the types of stars combined. Here we compare synthetic cluster HR diagrams with observed cluster HR diagrams for NGC 3293, h and χ Persei (a composite HR diagram), NGC 3766, and NGC 4755. These clusters were chosen because their ages are within the range covered by our evolutionary tracks and they have *uvby* photometry or effective temperatures and luminosities for a sizeable sample of stars within our mass range. The results of this comparison are shown in figure 4.1, figure 4.2, figure 4.3, and figure 4.4, respectively. The HR diagram data, masses, and age for h and χ Persei members are taken from Slesnick, Hillenbrand, & Massey (2002). For NGC 3293 the *uvby* photometry, distance, and age are taken from Balona (1994b). For NGC 3766 and NGC 4755 the *uvby* photometry has been taken from WEBDA[1], and ages of 20 Myr (Patenaude, 1978) and 10 Myr (Sanner et al., 2001) are adopted for these clusters, respectively.

The photometry for NGC 3293, NGC, 3766, and NGC 4755 has been dereddened fol-

---

[1] WEBDA is an online database for open star clusters. The URL for the site is http://www.univie.ac.at/webda/.

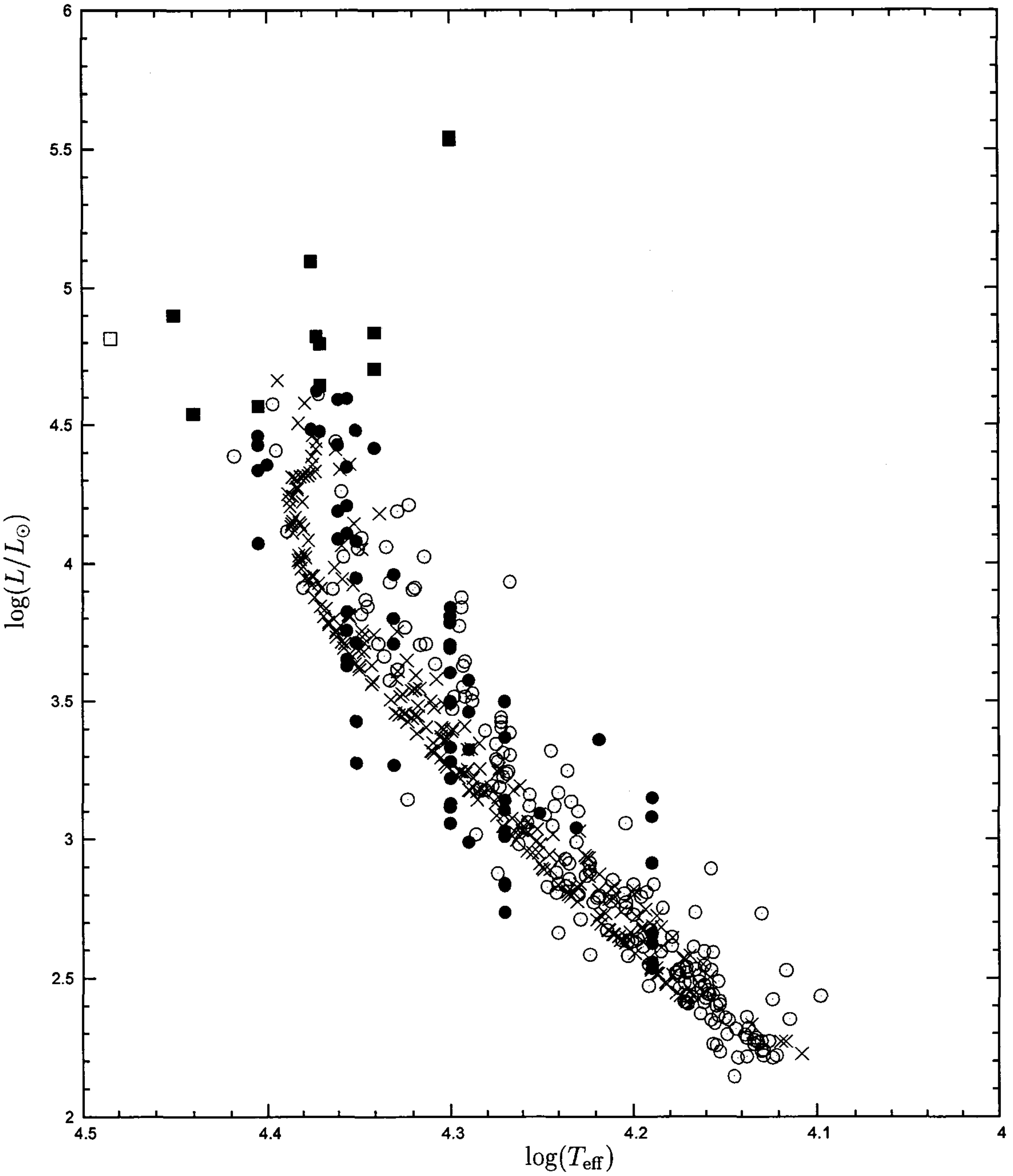

Figure 4.1: A comparison of h and χ Persei with a synthetic cluster. The synthetic cluster has been created with an age of 12.8 Myr over the mass range 4 to 15 $M_\odot$ and are denoted by "X" 's. The filled symbols are members whose temperature has been determined using spectroscopy, and the open symbols are members who's temperature has been determined only photometrically. Circles correspond to stars with masses within the 4 to 15 $M_\odot$ range. The squares correspond to stars outside this range. The data for h and χ Persei are from Slesnick, Hillenbrand, & Massey (2002).

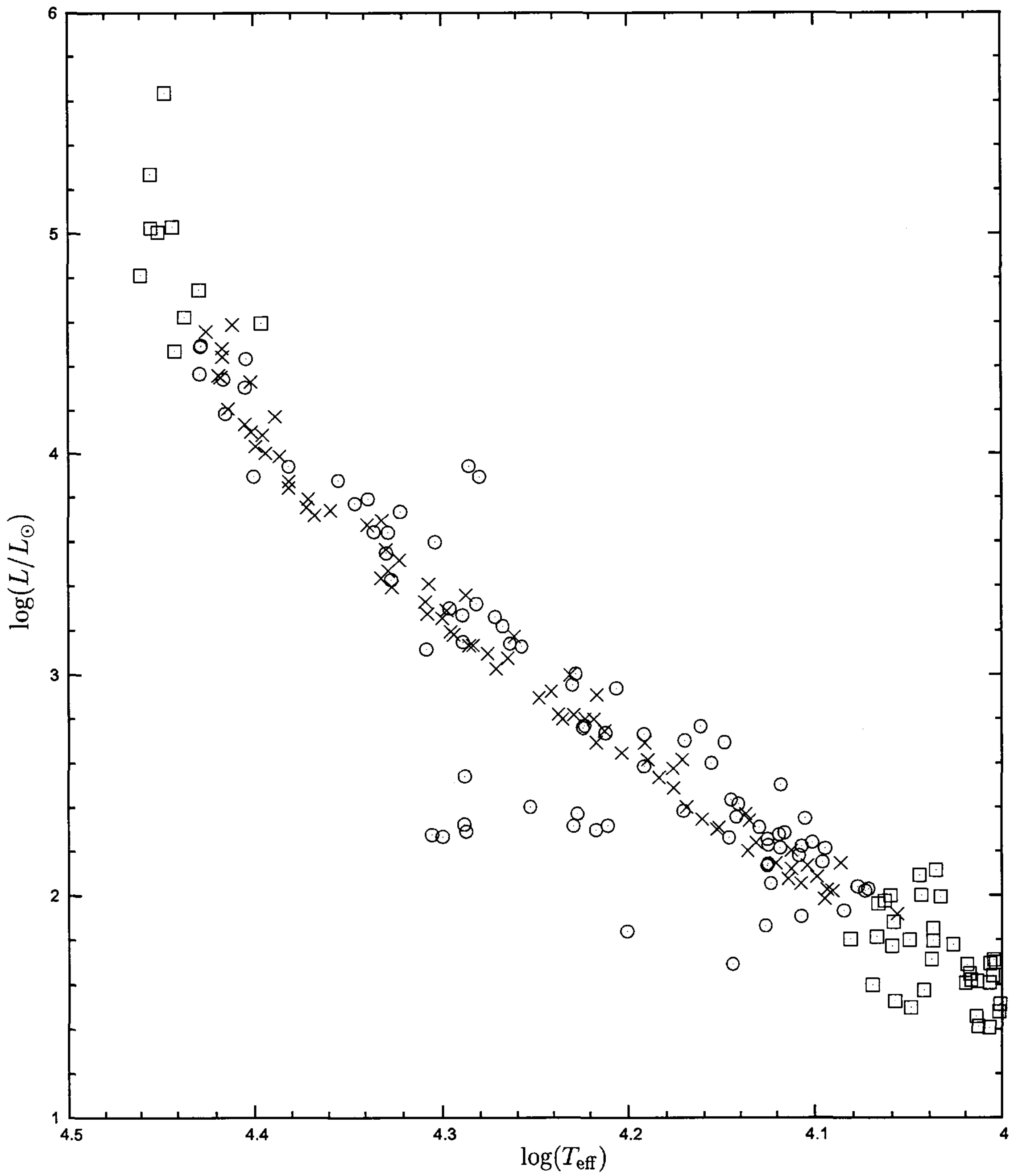

Figure 4.2: A comparison of NGC 3293 with a synthetic cluster of age 10 Myr. The open circles are members within the 3 to 15 $M_\odot$ range. The open squares denote members outside the mass range. The X's represent the synthetic cluster. Photometry for the observed cluster is from Balona (1994b).

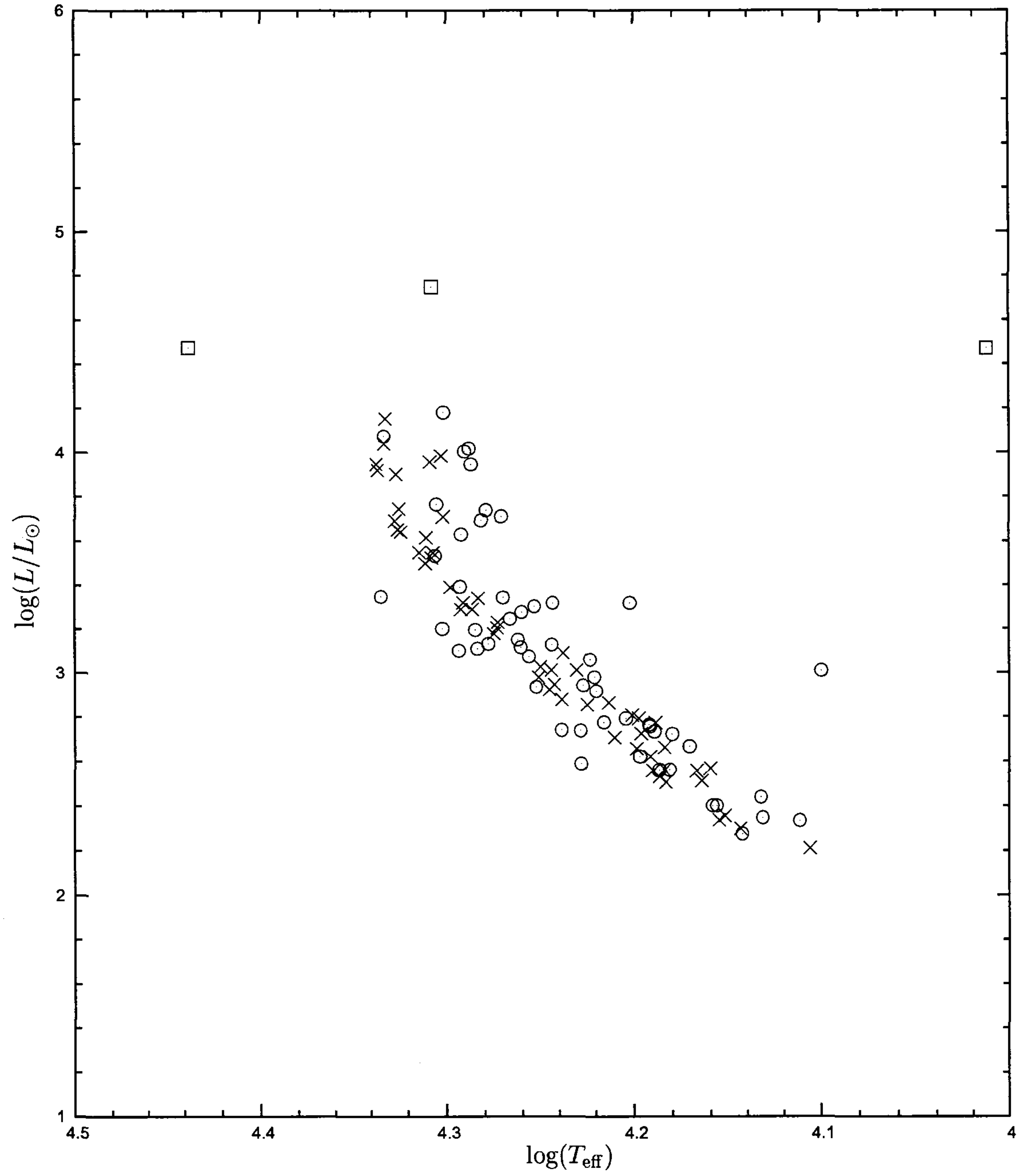

Figure 4.3: A comparison of NGC 3766 with a synthetic cluster of age 20 Myr. The open circles are members within the 3 to 15 $M_\odot$ range. The open squares denote members outside the mass range. The X's represent the synthetic cluster. Photometry for the observed cluster is from WEBDA.

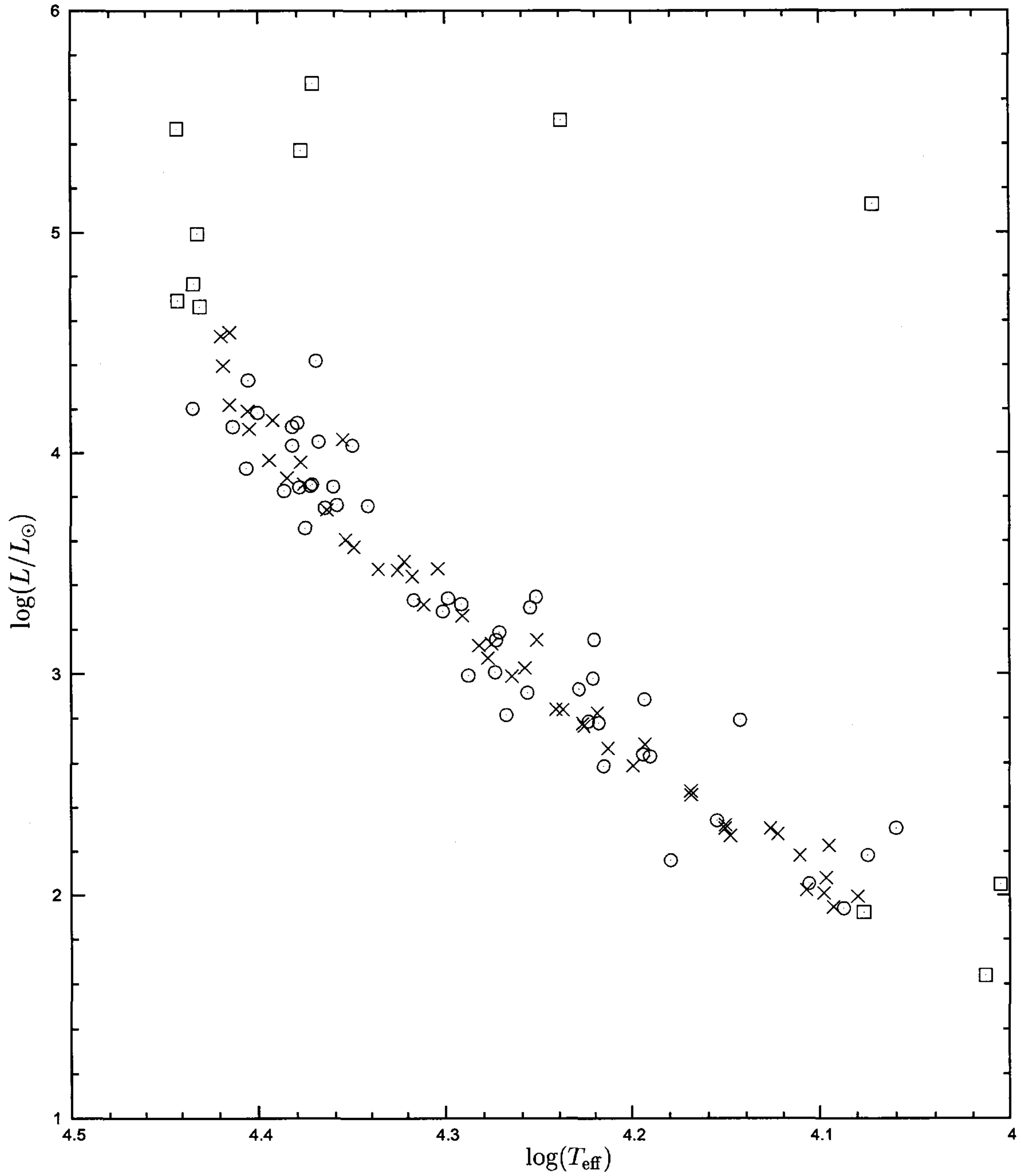

Figure 4.4: A comparison of NGC 4755 to a synthetic cluster of age 10 Myr. The open circles are members within the 3 to 15 $M_\odot$ range. The open squares denote members outside the mass range. The X's represent the synthetic cluster. Photometry for the observed cluster is from WEBDA.

lowing the procedure of Shobbrook (1983), and converted into effective temperatures, luminosities and masses using the procedure outlined by Balona (1994a). By dereddening the individual stars following the procedure by Shobbrook (1983), and not using simply a mean reddening for the cluster, the circumstellar reddening suggested by Turner (1993), who states that the effects of circumstellar reddening are almost indistinguishable from those of interstellar reddening, should be adequately treated.

In figure 4.1 for h and χ Persei, the X's denote the synthetic cluster stars, and the filled symbols denote members whose temperature was determined using spectral types, and the open symbols denote members whose temperature was determined only photometrically. Squares correspond to stars with masses outside the mass range of the synthetic cluster (4 to 15 $M_\odot$). In figures 4.2, 4.3, and 4.4 the open circles are members within the 3 to 15 $M_\odot$ range. The open squares denote members outside the mass range. The X's again represent the synthetic cluster stars. The numbers of stars for all synthetic clusters have been chosen to match that of the observed sample within our mass range, and a Salpeter (1955) mass function has been used for all synthetic clusters. For h and χ Persei, NGC 3293, NGC 3766, and NGC 4755 there were 266, 80, 54, and 50 members, respectively, within our grid's mass range. While a membership of 266 will certainly allow application of the computed C_f, a membership of 80 allows one to draw only marginal conclusions about selected members while memberships of 54 and 50 allow no conclusions for selected members. All clusters, however, allow a comparison of the width of the observed main sequence to the width of the synthetic main sequence.

The spread of the main sequence of h and χ Persei is much larger, 1.8 times wider in temperature, than that of the synthetic clusters. Collins (1966) states that many other effects may play a role, such as metal abundance and age spread. Because h and χ Persei are considered together, there may be differences between the clusters which could help to spread out the observed main sequence. Inaccuracies in the relative distance estimates for the h and χ clusters would also increase the width of observed main sequence. Another effect to consider is differential rotation, which will likely help to broaden the main sequence (Collins & Smith, 1985). Differential rotation can have a great effect on the length and orientation of the inclination curve (see Gillich, 2007), and thus could be a factor. From figure 4.1 and 4.3 it can be seen that there are significantly more slowly rotating stars near the ZAMS turnoff for the synthetic cluster than in the observed cluster. This suggests that there may be more rapidly rotating stars than in the synthetic cluster, which assumes a uniform distribution of rotation ($p = 1$), supporting the suggestion by Strom, Wolff, & Dror (2005) and Wolff, Strom, Dror, & Venn (2007) that dense clusters have more rapidly rotating stars.

In view of the comparison of NGC 3293, NGC 3766, and NGC 4755 to synthetic clusters, the width of the observed main sequence is reasonably well matched by the rotationally widened main sequence of the synthetic cluster. This could be a result of using a single cluster that is more confined and more homogenous. The width of the observed cluster being reasonably well matched by a synthetic cluster that includes rotational effects is not inconsistent with the idea that the observed width, at least in part, results from rotation, and the assumptions made in generating the synthetic clusters are possibly valid.

In the case of NGC 3293 and NGC 4755, however, the age of 10 Myr is such that there are still stars present with masses above the upper mass limit of our grid. Thus, C_fs determined here cannot be strictly applied to this cluster. It can likely be said that the stars on the redder side are rapidly rotating. The number of stars in NGC 3293 causes the brightest star not to be a very reliable indicator. However, the reddest star and the bluest star both have a C_f of 0.68 in which they are rapidly rotating and seen equator-on or pole-on, respectively, for a membership of 80 stars. In NGC 4755 there are too few stars to make any conclusions about the selected members' rotational characteristics.

h and χ Persei and NGC 3766, at ages of 12.8 Myr and 20 Myr respectively, are old enough that the most massive stars in our grid will have moved to the right in the HR diagram. However, there are still massive stars present near the ZAMS. This could be from field star contamination or from stars in the cluster that have formed relatively recently. In either case the stars would have to be removed from consideration to apply directly the rotational constraints on members based on their location.

The difficulties highlighted here indicate that it is very important to consider the properties of the observed cluster used for comparison. Namely the age of the cluster must be old enough to remove stars more massive than those of our grid, and the cluster must be homogenous and well confined. Composite HR diagrams are likely not as useful because they can introduce heterogeneity into the sample. Also the observed cluster should have a large number of members in order to be reasonably confident of the rotational characteristics of the selected cluster members. Cluster memberships of more than 150 in this mass range are ideal.

5 CONCLUSIONS

In this thesis the effects of stellar rotation were examined in the context of synthetic clusters. The width of the main sequence was examined for different rotation distributions among cluster members to see if there was a trend in the main sequence width with rotation distribution. It was found that, while there is generally a trend in the main sequence width to be largest when there is a wide range of rotations and to be smallest when there is either many slow or fast rotators but not both, the trend is small compared to the standard deviation of the sample. That makes it impossible to say with any certainty what the distribution of rotation is among cluster members based on the width of the main sequence.

The comparison of synthetic cluster to observed clusters is complicated by multiple factors affecting the observed main sequence width, such as age spread among cluster members, unresolved binary companions, field star contamination, and photometric errors. Out of the four observed clusters examined, three have main sequence widths consistent with that of a synthetic rotationally broadened cluster. In h and χ Persei the observed main sequence width significantly exceeds that of the synthetic cluster main sequence on both the blue and red sides.

The results of the statistics on synthetic clusters suggests that by selecting specific locations on the HR diagram will allow one to put constraints on the rotation rate and inclination of a cluster member with some modest but not overwhelming certainty. The locations which appear to be the best indicators of rotation are ones in which the select cluster member can only obtain the location from rotational effects, and changing mass cannot achieve the same location. The selected member which is the most robust is the reddest star above a predefined luminosity cutoff. The reason is that the effects of changing mass on the star's HR location play a minor role in placing a star at the selected location, while rotational effects are needed for a cluster member to reach the selected location. The applicability of the C_fs depend on the properties of the observed cluster. The cluster would need to have an age near 11 Myr and have photometry available for about 150 members in our mass range to be able to draw meaningful conclusions about selected members.

Another interesting result is that using the bluest star as an indicator of rotational characteristics when a cluster has members in the gravitational contraction phase of evolution produces lower C_f values. The members that are in the gravitational contraction phase can be bluer than the bluest stars at the ZAMS turn-off even for those on the ZAMS turn-off seen exactly pole-on and very rapidly rotating. Because there will be very few stars in the gravitational contraction phase, because of the short lifetime of the phase, it is unlikely that the bluest of these stars will have specific rotational characteristics, and it can only be said that they are massive. This problem may be fixed with application of a luminosity cutoff as was done with the reddest cluster member.

REFERENCES

Balona, L. A. 1994a, MNRAS, 268, 119

—. 1994b, MNRAS, 267, 1060

Becker, S. A., & Mathews, G. J. 1983, ApJ, 270, 155

Bodenheimer, P. 1971, ApJ, 167, 153

Carroll, J. A. 1928, MNRAS, 88, 548

—. 1933, MNRAS, 93, 478

Chiosi, C., & Maeder, A. 1986, ARA&A, 24, 329

Clement, M. J. 1974, ApJ, 194, 709

—. 1978, ApJ, 222, 967

—. 1979, ApJ, 230, 230

Collins, G. W. 1966, ApJ, 146, 914

Collins, II, G. W. 1963, ApJ, 138, 1134

—. 1965, ApJ, 142, 265

Collins, II, G. W., & Smith, R. C. 1985, MNRAS, 213, 519

Collins, II, G. W., & Truax, R. J. 1995, ApJ, 439, 860

Collins, II, G. W., Truax, R. J., & Cranmer, S. R. 1991, ApJS, 77, 541

Cowling, T. G. 1935, MNRAS, 96, 42

Demarque, P. 1967, ApJ, 149, 117

Deupree, R. G. 1974, ApJ, 194, 393

—. 1990, ApJ, 357, 175

—. 1995, ApJ, 439, 357

—. 1998, ApJ, 499, 340

—. 2000, ApJ, 543, 395

—. 2001, ApJ, 552, 268

Elvey, C. T. 1930, ApJ, 71, 221

Faulkner, J., Roxburgh, I. W., & Strittmatter, P. A. 1968, ApJ, 151, 203

Fowler, W. A., Caughlan, G. R., & Zimmerman, B. A. 1967, ARA&A, 5, 525

Frémat, Y., Zorec, J., Hubert, A.-M., & Floquet, M. 2005, A&A, 440, 305

Gardiner, J. G. 1951, MNRAS, 111, 94

Gillich, A. 2007, Master's thesis, Saint Mary's University, Halifax, Nova Scotia

Hardorp, J., & Strittmatter, P. A. 1968a, ApJ, 153, 465

—. 1968b, ApJ, 151, 1057

Harris, G. L. H., & Deupree, R. G. 1976, ApJ, 209, 402

Hauschildt, P. H., & Baron, E. 1999, J. Comput. Appl. Math, 109, 41

Henyey, L. G., Forbes, J. E., & Gould, N. L. 1964, ApJ, 139, 306

Iben, I. J. 1965a, ApJ, 141, 993

—. 1965b, ApJ, 142, 1447

—. 1966a, ApJ, 143, 483

—. 1966b, ApJ, 143, 516

—. 1966c, ApJ, 143, 505

—. 1967a, ApJ, 147, 650

—. 1967b, ApJ, 147, 624

Iglesias, C. A., & Rogers, F. J. 1996, ApJ, 464, 943

Jackson, S. 1970, ApJ, 161, 579

Jackson, S., MacGregor, K. B., & Skumanich, A. 2005, ApJS, 156, 245

Lovekin, C. C. 2005, Master's thesis, Saint Mary's University, Halifax, Nova Scotia

Lovekin, C. C., Deupree, R. G., & Short, C. I. 2006, ApJ, 643, 460

Maeder, A., & Meynet, G. 1989, A&A, 210, 155

Maeder, A., & Peytremann, E. 1970, A&A, 7, 120

Mark, J. W.-K. 1968, ApJ, 154, 627

Meyer-Hofmeister, E. 1969, A&A, 2, 143

Ostriker, J. P., & Mark, J. W.-K. 1968, ApJ, 151, 1075

Patenaude, M. 1978, A&A, 66, 225

Richtmyer, R. F., & Morton, K. W. 1957, Difference Mehods for Initial Value Problems (New Your, Interscience)

Rogers, F. J., Swenson, F. J., & Iglesias, C. A. 1996, ApJ, 456, 902

Roxburgh, I. W., Griffith, J. S., & Sweet, P. A. 1965, Zeitschrift fur Astrophysik, 61, 203

Roxburgh, I. W., & Strittmatter, P. A. 1965, Zeitschrift fur Astrophysik, 63, 15

Sackmann, I. J., & Anand, S. P. S. 1969, ApJ, 155, 257

—. 1970, ApJ, 162, 105

Salpeter, E. E. 1955, ApJ, 121, 161

Sandage, A. 1962, ApJ, 135, 349

Sandage, A., & Eggen, O. J. 1969, ApJ, 158, 685

Sanner, J., Brunzendorf, J., Will, J.-M., & Geffert, M. 2001, A&A, 369, 511

Schlesinger, B. M. 1969, ApJ, 157, 533

Schou, J., Antia, H. M., Basu, S., Bogart, R. S., Bush, R. I., Chitre, S. M., Christensen-Dalsgaard, J., di Mauro, M. P., Dziembowski, W. A., Eff-Darwich, A., Gough, D. O., Haber, D. A., Hoeksema, J. T., Howe, R., Korzennik, S. G., Kosovichev, A. G., Larsen, R. M., Pijpers, F. P., Scherrer, P. H., Sekii, T., Tarbell, T. D., Title, A. M., Thompson, M. J., & Toomre, J. 1998, ApJ, 505, 390

Shajn, G., & Struve, O. 1929, MNRAS, 89, 222

Shobbrook, R. R. 1983, MNRAS, 205, 1215

Simpson, E., Hills, R. E., Hoffman, W., Kellman, S. A., Morton, E. J., Paresce, F., & Peterson, C. 1970, ApJ, 159, 895

Slesnick, C. L., Hillenbrand, L. A., & Massey, P. 2002, ApJ, 576, 880

Slettebak, A., Kuzma, T. J., & Collins, II, G. W. 1980, ApJ, 242, 171

Smith, R. C. 1971, MNRAS, 151, 463

Stoeckley, T. R. 1968, MNRAS, 140, 141

Strom, S. E., Wolff, S. C., & Dror, D. H. A. 2005, AJ, 129, 809

Sweet, I. P. A., & Roy, A. E. 1953, MNRAS, 113, 701

Tassoul, J.-L. 1978, Theory of Rotating Stars (Princeton University Press)

Townsend, R. H. D., Owocki, S. P., & Howarth, I. D. 2004, MNRAS, 350, 189

Turner, D. G. 1993, A&AS, 97, 755

Turner, D. G. 1996a, in Astronomical Society of the Pacific Conference Series, Vol. 90, The Origins, Evolution, and Destinies of Binary Stars in Clusters, ed. E. F. Milone & J.-C. Mermilliod, 443–+

Turner, D. G. 1996b, in Astronomical Society of the Pacific Conference Series, Vol. 90, The Origins, Evolution, and Destinies of Binary Stars in Clusters, ed. E. F. Milone & J.-C. Mermilliod, 382–+

von Zeipel, H. 1924, MNRAS, 84, 665

Wolff, S. C., Strom, S. E., Dror, D., & Venn, K. 2007, AJ, 133, 1092